Electroweakly Interacting Spin-1 Dark Matter and Its Phenomenology

February 21, 2022

Department of Physics, Graduate School of Science,
Division of Particle and Astrophysical Science,
Nagoya University

Motoko Fujiwara

Preface

Dark Matter (DM) is a mysterious massive source that occupies about 85 % of the matter components in our universe. One of the most promising DM candidates is Weakly Interacting Massive Particle (WIMP), which interacts with the ordinary matter and is thermalized in the early hot universe. Electroweakly-charged DM candidates, in particular, are well-studied because these candidates often appear in scenarios motivated to solve hierarchy problems such as theories with supersymmetry and extra-dimension. These candidates are directly related to physics beyond the Standard Model (SM). Therefore, identifying DM quantum numbers should be crucial hints not only to narrow down the theoretical possibility for DM interactions but also to probe the physics behind DM. One interesting scenario for DM identification is the discrimination of spin-1/2 and spin-1 signatures predicted from the $\mathrm{SU}(2)_L$ triplet DM with $Y = 0$, which corresponds to the Wino DM (spin-1/2) in the Minimal Supersymmeric SM and the Kaluza-Klein electroweak boson (spin-1) in the extra-dimensional scenario.

In this thesis, electroweakly interacting spin-1 DM and its experimental signatures are studied to investigate the possibility to discriminate DM spin in the above scenarios. We use the simplified model that realizes the essential features of DM candidates in extra-dimensional setups. We focus on DM annihilation processes to determine the viable range to obtain correct DM thermal relic abundance and the achievable region in the next-generation DM indirect detection. It is well-known that the electroweak potential relevantly affects the non-relativistic (NR) DM annihilation cross section, which is called the Sommerfeld effect. To include this effect, we derive the NR effective theory to describe DM pair annihilation. Solving the Schrödinger equations for two-body states composed of DM multiplets, we numerically obtained the predictions on DM annihilation cross sections including the Sommerfeld effect. We studied the DM annihilation in the early universe to evaluate predictions on DM thermal relic abundance. Due to the difference in spin-statistics, signs of the $Q = 1$ two-body state potentials are different between spin-1/2 and spin-1 DM system: A spin-1/2 DM pair have the attractive potential, while a spin-1 DM pair feels repulsive potential. Since spin-1 DM may have $J = 2$ partial wave cross section, where J is the total spin of two-body states, the larger annihilation cross section is predicted compared to the spin-1/2 DM candidate. In our leading order calculation, the correct thermal relic abundance is predicted by $m_{\mathrm{DM}} \simeq 3.1$ TeV ($m_{\mathrm{DM}} \gtrsim 3.4$ TeV) for the spin-1/2 (spin-1) DM candidate. We studied the monochromatic gamma-ray signatures and reveal the current constraint and the achievable region in the future gamma-ray observation. We also found that the heavier neutral spin-1 particle (Z'), which is often associated with spin-1 DM theory, may play an important role in DM identification. If spin-1 DM pair may annihilate into Z' and a photon, the separable two monochromatic peaks are predicted in the photon energy spectrum. The peak locations are determined by masses of spin-1 DM and Z', and thus we can reconstruct the mass spectrum in this theory. Considering the energy resolution, we specified the region where separable two peaks may be probed in the Cherenkov Telescope Array. Our analysis of the simplified model is straightforwardly applicable for extra-dimensional theories that predict electroweakly interacting spin-1 DM candidates, which will be completed in our future work.

Acknowledgment

I would like to thank my Ph.D. advisor, Prof. Junji Hisano, for his continued support in this doctoral project. The discussion about the Sommerfeld effects in electroweakly interacting spin-1/2 DM systems helps me to calculate annihilation processes in the spin-1 DM system. I would also like to thank Dr. Tomohiro Abe for the useful discussions and Dr. Kohei Matsushita for the discussion on the early stage of this project. I thank Prof. Seong Chan Park for the useful discussions and comments.

Besides, I would like to thank the referees of the Ph.D. defense, Dr. Kiyotomo Ichiki, Prof. Yoshitaka Ito, Dr. Nobuhiro Maekawa, and Prof. Shinichi Nojiri. I appreciate their fruitful comments during the defense presentation, which helps me to enhance the quality of this thesis.

This doctoral project was supported by JSPS Grant-in-Aid for Scientific Research KAKENHI Grant Number JP20J12392. This work is also supported by JSPS Core-to-Core Program Grant Number JPJSCCA20200002.

Contents

1 Introduction

Since the lack of gravitational source in the clusters of galaxies is pointed out in the 1930s [1, 2], we have found overwhelming evidence of dark matter (DM). The various astrophysical observations such as the rotational curves of the galaxies [3, 4] imply existence of DM indirectly. These experiments suggest the following qualitative features of DM:

- DM should be electrically neutral because we can not directly detect it in astrophysical observations.
- DM should behave as a matter component in the structure formation of galaxies, which is called *cold DM*, to be consistent with the numerical n-body simulation.
- DM is stable or sufficiently long-lived to survive in the current universe.

Besides, we know one more quantitative fact on DM. Assuming a specific cosmological model, we can determine the ratio of the DM energy density in our universe by observing the Cosmic Microwave Background (CMB). According to the latest analysis assuming the ΛCDM model by the Planck collaboration [5], DM is a dominant matter content and occupies a quarter of the energy density in the universe. There is no suitable candidate that satisfies all the above conditions in the Standard Model (SM) of particle physics, and thus we need to extend the framework to explain the mysterious matter component.

One interesting possibility is that DM is embedded in a theoretical framework of physics beyond the SM (BSM), which is motivated to solve problems in the SM framework. Various DM candidates, indeed, are proposed and studied in various contexts. If we obtain signals of DM in upcoming experiments, the next step should be an identification of DM from these various candidates. To archive this goal, it is essential to reveal the distinctive signatures from each DM candidate. Understanding the nature of DM could provide significant information on an underlying physics. In particular, it could give implications for other mysteries in our universe such as the matter-antimatter asymmetry and the origin of neutrino masses.

One of the most promising DM candidates is Weakly Interacting Massive Particle (WIMP), and its thermal history is called WIMP scenario. In this scenario, DM is assumed to have interactions with ordinary matter and to be thermalized in the SM plasma in the early universe. Once we put this assumption, DM physics is independent of the initial conditions of the universe, such as mechanisms of inflation and reheating, and thus this scenario is highly predictable. The theoretical predictions can be tested through the various interaction channels such as scattering, annihilation, and production processes. These experimental searches would also be powerful tools for DM identification.

Electroweakly interacting DM is one attractive class of WIMPs where DM mainly interacts with the SM particles through electroweak couplings. The minimal framework to study this hypothesis is to introduce one multiplet charged under the $\mathrm{SU}(2)_L$ symmetry, which is called *Minimal DM* scenario. We may systematically assign the electroweak charges such that electrically neutral component presents in the new multiplet. DM masses that achieve the correct DM energy density is determined for each DM multiplet, which is about $\mathcal{O}(1)$ TeV range. In this scenario, therefore, all we have to specify is DM spin to write down the

interaction theory between DM and the SM particles. The phenomenology has been studied in many contexts [6, 7, 8], mainly focused on the spin-0 and spin-1/2 DM scenarios. The most nontrivial question in this electroweakly interacting DM hypothesis is how to realize electroweak charge and DM stability at the same time. It is because $\mathcal{O}(1)$ TeV DM with electroweak decaying channels are not thermally abundant in the current universe due to the short lifetime. This question is addressed in some BSM scenarios that naturally provide discrete symmetry that stabilizes electroweakly interacting DM candidates. One example is a theory with supersymmetry (SUSY). In this scenario, all the particles associate partners with different spin-statistics. The simplest model is the Minimal Supersymmetric extension of the Standard Model (MSSM) where all the SM matter fields are promoted to the chiral superfields, and the gauge fields are promoted to the vector superfields, respectively. We can define the discrete symmetry called *R-parity* that is depending on the baryon number, the lepton number, and the spin of the particles [9]. The most remarkable feature of this discrete symmetry is that all the SM fields turn out to be even while the superpartner is odd. If this symmetry is exact, therefore, the Lightest Superpartner of the SM fields (LSP) can be a stable DM candidate. The spectrum depends on the parameters in the model but one popular benchmark candidate is *the Wino DM*. The Wino DM is the $\mathrm{SU}(2)_L$ triplet Majorana fermion (spin-1/2) and a superpartner of the $\mathrm{SU}(2)_L$ gauge bosons. Through the electroweak interactions, we may achieve the correct DM abundance with about 3 TeV DM mass. Another example is a theory with extra-dimensions. The simplest extra-dimensional model is called the Universal Extra-Dimension (UED) where the SM fields propagate in the five dimensional spacetime with the flat metric. To realize the chiral theory with extra-dimensions, the five dimensional coordinate y is compactified as the circle with the identification of the point $y = -y$, which is called the orbifold compactification. After this compactification, the discrete symmetry called *Kaluza Klein parity* (KK-parity) remains. Under this parity symmetry, all the SM particles are even and associate the infinite number of particles with the same quantum numbers such as spin and the charge of the SM symmetry. These particles are called the *Kaluza Klein partner* (KK partner). If the Lightest KK-parity odd particle (LKP) is electrically neutral, then it may be a stable DM candidate. Which spectrum turns out to be the LKP is depending on the parameters in the theory but one interesting possibility is that the LKP is the KK partner of the electroweak bosons. In this case, DM is $\mathrm{SU}(2)_L$ triplet vector (spin-1). This minimal model and its phenomenologies are studied in Ref. [10, 11, 12, 13]

In the coming decades, the next-generation DM experiments such as the XENONnT, LZ, DARWIN, and Cherenkov Telescope Array (CTA) plan to upgrade their experimental sensitivities. The electroweakly interacting DM predicts the signals that can be explored by these experiments. Therefore, we expect to obtain further information about electroweakly interacting DM. As mentioned above, some electroweakly interacting DM candidates directly relate to the BSM scenarios. We may obtain remarkable implications on a theory behind DM if we may specify the quantum numbers of DM, such as the electroweak charge and spin, through the experimental tests.

One of the most important scenarios is the spin separation of the $\mathrm{SU}(2)_L$ triplet DM with spin-1/2 and spin-1, which corresponds to the separation of the Wino DM (spin-1/2)

and the KK electroweak boson DM (spin-1). One powerful tool for spin discrimination is a collider experiment where we can produce the BSM particles directly. However, if these DM candidates have exact odd-parity and thus, DM only appears in pair production processes. Consequently, TeV scale DM is difficult to produce even in the current Large Hadron Collider (LHC) experiment. Besides, the viable searching channel is an event with large missing energy, and thus we may not extract relevant information on DM spin from final states. Other than the collider experiments, we may infer the DM features from direct and indirect detection experiments where we try to observe the DM signals in the Milky-way galaxies. However, the spin-discrimination is again a challenging issue. The averaged velocity of DM in the current universe is totally non-relativistic (NR), and thus spin-dependent features tend to decouple from low energy signatures.

In this thesis, we study the pair annihilation processes of DM and reveal the differences caused by DM spin. In particular, we will consider the following two annihilation processes:

(1) Annihilation of DM multiplets in the early universe to determine the prediction of DM energy density.

(2) DM pair annihilation processes in the current universe that may be probed by astrophysical observation such as a gamma-ray search.

There are three reasons why we consider the annihilation channels to discriminate spin-1/2 and spin-1 DM candidates: First, DM is distributed with the NR velocity, and thus the interaction processes are dominated by the s-wave contributions. This means that, in the NR limit, the spin-statics directly determine the symmetricity of a wave function for a pair of DM multiplets. Spin-1/2 and spin-1 DM candidates follow different spin-statistics and have different numbers of spin degrees of freedom, which causes viable differences in the predicted annihilation cross section between DM multiplets. Second, as shown in (1), the current DM energy density is one of the most important predictions because we may specify the feasible DM mass range to explain the correct DM energy density following the WIMP scenario. If spin dependence is relevant in the annihilation cross section, we may have a finite gap of DM mass that can achieve the correct abundance. Third, as shown in (2), signals from DM pair annihilation are promising searching channels of electroweakly interacting DM. We focus on the line gamma-ray channels in this thesis because this channel provides striking DM signals due to the following reasons: If a TeV scale DM has annihilation channels into more than one photon, it predicts the line-like peak in the photon energy spectrum. The peak location is determined by masses of DM and final state particles. Since there is no astrophysical background source that predicts the line gamma-ray monochromatic peak in the expected energy range, it is easy to search TeV scale DM signatures. Moreover, we may reconstruct the mass spectrum of DM from the energy value of a monochromatic peak. We may have a great chance to probe gamma-ray from DM annihilation in next-generation gamma-ray observation such as Cherenkov Telescope Array (CTA), which is sensitive for a photon with $\mathcal{O}(1)$ TeV or higher energy. Specifying the DM mass and DM annihilation cross section in light of gamma-ray search, we may discriminate spin-1/2 and spin-1 DM candidates and may narrow down possibilities of DM theories.

Since a DM pair annihilates with NR relative velocity in its center mass frame, perturbative calculations may break down due to the effects of electroweak potential. The electroweak potential force gets effectively larger in the NR limit of DM multiplets and distorts the wave function of DM two-body states from the plane wave profile. This effect is called *the Sommerfeld effect*, which is originally proposed for the Coulomb potential by Sommerfeld and is applied to the Wino DM system with the electroweak potential [14]. The potential induced by the W boson exchanging processes realizes mixing between electrically neutral DM states, and thus DM can annihilate into photons without loop suppression. We have to construct NR effective theory to systematically include electroweak potential effects in the evaluation of annihilation cross sections. The NR effective theories for spin-0 and spin-1/2 DM are already completed in contexts of the supersymmetric DM and the Minimal DM. We may apply the same procedures for spin-1 DM to construct an effective theory. Precise evaluation of DM annihilation cross section in each theory is crucial to conclude the possibility of DM spin discrimination in the next-generation gamma-ray observation. This is our motivation to study the Sommerfeld effects in spin-1 DM systems with electroweak interactions.

This thesis is organized as follows: In Sec. 2, We briefly show fundamental physics on DM such as observational evidence. Then, focusing on WIMP DM candidate, we review the standard thermal history called WIMP scenario and how to solve the time evolution of WIMP in the expanding universe. In Sec. 3, we review electroweakly interacting DM candidates, in which we discuss the possibility of discrimination between spin-1/2 and spin-1 DM with $\mathrm{SU}(2)_L$ triplet and $Y = 0$ interactions. These DM candidates correspond to simplified models of the Wino DM and the KK electroweak boson DM. Section 4 is devoted to showing a formalism to describe NR DM pair annihilation including electroweak potential forces. We briefly review matching procedures to construct a NR effective field theory and show results for the spin-1 DM system, which is one of the main results of this thesis. In Sec. 5 and Sec. 6, we apply this formalism to evaluate the current DM energy density and the annihilation cross section into photons, respectively. We show the parameter regions where we may explain the correct DM energy density. We also specify regions where we expect signatures in the CTA experiments considering the uncertainty of the local DM density. We devote Sec. 7 to give our conclusions. Throughout this thesis, we use the natural unit where $\hbar = c = 1$.

2 WIMP Dark matter and its thermal history

We accumulated overwhelming evidence that suggest the existence of DM in our universe. The various possibilities of DM are proposed in various contexts. One interesting possibility is that DM is an unknown elementary particle. Besides, if DM couples to the SM particles and is thermalized in the early universe, we may obtain predictions that are less dependent on the initial conditions of the universe. Solving the Boltzmann equation for the DM number density, we may derive a prediction on the current DM energy density. Requiring the predicted value to realize the observed DM energy density, we may constrain the parameters in DM theory. In Sec. 2.1, we briefly review DM evidence, which is pointed out in a wide range of the cosmological scale. One of the most popular DM candidates is WIMP. We review the thermal history of WIMP and summarize how to solve the time evolution of DM energy density. In Sec. 2.2, we show a more dedicated treatment of solving DM density evolution assuming the degenerated parity-odd particles in the system. The derived formulas are necessary to discuss the electroweakly interacting DM system where we have a nearly degenerated parity-odd spectrum.

2.1 Dark Matter evidence and WIMP hypothesis

DM evidence is discovered in various independent astrophysical observables of various cosmological scales. First, the total mass of the cluster can be estimated from the visible source in the astrophysical observation where the missing mass in our universe is discovered [1]. The DM existence in our universe was first claimed by Zwicky [2] through the analysis of the dynamical mass of the Coma galaxy cluster.

Second, the rotation curves of spiral galaxies also imply a missing gravitational source [3, 4]. The spiral velocities are measured through the Doppler shift of Hydrogen 21 cm line observations. Applying the Newton's gravitational law for the spiral galaxy, the circular speed v_c is estimated to be

$$v_c = \sqrt{\frac{GM_<}{r}}, \tag{2.1}$$

where G is the gravitational constant and $M_<$ is the mass in the range of radius r. The observed velocity is flat in large r that is outside of the visible disc. This fact implies an invisible massive source also exists around the visible disc to keep v_c to be constant.

Third, DM existence is also essential to explain structure formation. The most successful mechanism for structure formation is gravitational instability. In this mechanism, small initial density fluctuations evolve by gravitational forces, which is crucial to realize structures such as galaxies and galaxy clusters. Since the baryon component, which corresponds to the SM particles, tightly couples to photons, perturbation of baryons can not grow fast enough to form observed structures in our galaxy. On the other hand, the DM component does not couple to photons due to the neutrality, and thus a power-low growth of perturbations is possible. Therefore, DM provides a density fluctuation that the baryon component can follow after the photon decoupling. This is one of the greatest reasons why DM is an essential component

in our universe. Assuming this mechanism of the gravitational structure formation, we may determine the energy density of DM in the current universe. In the Planck observation, the CMB angular power spectrum is observed precisely. Since the baryon and DM density affects the oscillation of the photon, the energy density of each component in the universe is determined to realize the observed CMB data. In particular, they assume the ΛCDM model where three major components of the universe, cosmological constant (Λ), cold DM (CDM), and baryon, is assumed. According to the latest result [5], we obtain

$$\Omega_{\rm DM}h^2 = 0.120 \pm 0.001, \tag{2.2}$$

where $\Omega_{\rm DM}$ is the density parameter of the universe and h is the Hubble parameter. This observational fact put an important constraint when we study DM physics since this is only the quantitative information that we know about DM.

As long as we can reach the correct value of DM energy density shown in Eq. (2.2), the properties of DM are unknown. Therefore, we have vast possibilities in DM mass and DM interactions with the SM particles. One of the most promising DM candidates is WIMPs. This DM candidate has GeV to TeV DM mass range and $\sim \mathcal{O}(1)$ pb cross section with the SM particles. The standard thermal history of WIMP is called WIMP scenario, which is frequently applied in many contexts of WIMP DM studies.

In this scenario, we assume that DM interacts with the SM particles and is thermalized in the early universe. The time evolution of DM number density is described by the Boltzmann equation.

$$\frac{dn}{dt} + 3Hn = 2\int d\Pi\ \mathcal{C}[E], \tag{2.3}$$

where n denotes the DM number density and H denotes the Hubble parameters. The factor of three in the second term on the left hand side (LHS) is originated from the number of spatial dimensions. The right hand side (RHS) is called a collision term. If there is no collision effect, the number density is conserved in the time evolution of n. Let us consider the situation where we have the number changing processes, $X + Y + \cdots \to A + B + \cdots$. The collision term has the following form.

$$\begin{aligned} 2\int d\Pi \mathcal{C}[E] = \int d\Pi_X d\Pi_Y d\Pi_A d\Pi_B \cdots (2\pi)^4 \delta^4(p_X + p_Y + \cdots - p_A - p_B - \cdots) \\ \times \Big[f_A f_B \cdots (1 \pm f_X)(1 \pm f_Y) \cdots |\mathcal{M}_{A+B+\cdots \to X+Y+\cdots}|^2 \\ - f_X f_Y \cdots (1 \pm f_A)(1 \pm f_B) \cdots |\mathcal{M}_{X+Y+\cdots \to A+B+\cdots}|^2 \Big], \end{aligned} \tag{2.4}$$

where f_i ($i = X, Y, \cdots, A, B, \cdots$) denotes distribution functions for each particle species. The factors of f_i are for initial particles. The factors of $(1 \pm f_i)$ are for final particles where the positive and negative signs are for the Boson and Fermion, respectively. To discuss the more specific situation for DM systems, we focus on the two-to-two process, $X + \bar{X} \to A + B$, where X and $\bar{X}$ denote a DM and an anti-DM. To simplify the Boltzmann equation, We assume the following assumptions, which can be widely applied to WIMP system.

- All the particles are in the kinetic equilibrium. We take the classical limit for the distribution function.

$$f_i = \left\{ \begin{array}{ll} \left[\exp\left(\frac{E_i-\mu_i}{k_BT}\right)-1\right]^{-1} & \text{(for Boson)} \\ \\ \left[\exp\left(\frac{E_i-\mu_i}{k_BT}\right)+1\right]^{-1} & \text{(for Fermion)} \end{array} \right\} \xrightarrow{\text{classical limit}} \exp\left(-\frac{E_i-\mu_i}{k_BT}\right) (\ll 1), \tag{2.5}$$

  where E_i and μ_i are the energy and chemical potential for i-th particle, respectively.

- The process is invariant under the time-reversal.

$$|\mathcal{M}_{X\bar{X}\to AB}|^2 = |\mathcal{M}_{AB\to X\bar{X}}|^2 \equiv |\mathcal{M}|^2. \tag{2.6}$$

- DM number is equal to the anti-DM number, $n_\chi = n_{\bar{\chi}}$.

- The final particles are in the thermal equilibrium, and thus number density is expressed as $n_{A(B)} \simeq n^{\rm eq}_{A(B)}$.

Under these assumptions, we may obtain a simpler expression of the Boltzmann equation.

$$\frac{dn_X}{dt} + 3Hn_X = -\langle\sigma v\rangle \left(n_X^2 - (n_X^{\rm eq})^2\right). \tag{2.7}$$

We define

$$n_i^{\rm eq} \equiv \int \frac{d^3p}{(2\pi)^3} g_i e^{-\frac{E_i}{k_BT}} = \frac{g_i m^3}{2\pi^2}\left(\frac{m}{T}\right)^{-1} K_2(x) \simeq \left\{ \begin{array}{ll} g_i \left(\frac{mT}{2\pi}\right)^{\frac{3}{2}} e^{-\frac{m}{T}} & (m \gg T), \\ \\ \frac{g_i T^3}{\pi^2} & (m \ll T), \end{array} \right. \tag{2.8}$$

where g_i denotes the internal degree of freedom for i-th particle and $K_n(x)$ denotes the modified Bessel function. We also introduce a thermalized velocity weighted cross section as defined below.

$$\langle\sigma v\rangle \equiv \frac{1}{(n_X^{\rm eq})^2} \int \frac{d^3p_X}{(2\pi)^3} \int \frac{d^3p_{\bar{X}}}{(2\pi)^3} \int \frac{d^3p_A}{(2\pi)^3} \int \frac{d^3p_B}{(2\pi)^3} \times (2\pi)^4 \delta^4(p_X + p_{\bar{X}} - p_A - p_B) |\mathcal{M}|^2 \exp\left(-\frac{E_X + E_{\bar{X}}}{k_BT}\right), \tag{2.9}$$

The time evolution of n_X is obtained by solving Eq. (2.7). For the numerical evaluation, it is more convenient to change the variables into $x = m/T$ where m denotes DM mass and T denotes the temperature of the thermal bath. We define *yield* for DM as a function of x.

$$Y_X(x) \equiv \frac{n_X}{s}, \tag{2.10}$$

where s denotes the total entropy density

$$s = \sum_i s_i, \tag{2.11}$$

and s_i as the entropy density for the i-th particle as defined below.

$$s_i \equiv \frac{\rho_i + p_i}{T}, \tag{2.12}$$

where ρ_i and p_i denote internal energy and pressure for the i-th component, respectively. For the relativistic particles, we can further simplify this expression by using the equation of state, $p_i = \rho_i/3$, and obtain the following expressions.

$$s_i = \frac{4\rho_i}{3T} \simeq \frac{2\pi^2}{45} g_i T_i^3 \begin{cases} 1 & \text{(Boson)} \\ \\ \frac{7}{8} & \text{(Fermion)} \end{cases}, \tag{2.13}$$

where T_i denotes the temperature of the i-th particle. It is convenient to introduce the effective degrees of freedom for the total entropy density g_{*s} and the total energy density g_*.

$$g_{*s}(T) \simeq \sum_{i:\text{Boson}} g_i \left(\frac{T_i}{T}\right)^3 + \frac{7}{8} \sum_{i:\text{Fermion}} g_i \left(\frac{T_i}{T}\right)^3, \tag{2.14}$$

$$g_*(T) \simeq \sum_{i:\text{Boson}} g_i \left(\frac{T_i}{T}\right)^4 + \frac{7}{8} \sum_{i:\text{Fermion}} g_i \left(\frac{T_i}{T}\right)^4. \tag{2.15}$$

Using these expressions, the total entropy density s can be expressed as the function of the temperature of photons, T.

$$s = \frac{2\pi^2}{45} g_{*s}(T) T^3. \tag{2.16}$$

Finally, Eq. (2.7) can be expressed as the differential equation of the yield, $Y_X(x)$.

$$\frac{dY_X}{dx} = -\frac{s}{xH}\left(1 - \frac{x}{3g_{*s}(x)}\frac{dg_{*s}(x)}{dx}\right)\langle\sigma v\rangle\left(Y_X^2 - (Y_X^{\text{eq}})^2\right), \tag{2.17}$$

where we introduce the yield at the thermal equilibrium, $Y_X^{\text{eq}}(x)$ as defined below.

$$Y_X^{\text{eq}}(x) \equiv \frac{n_X^{\text{eq}}}{s} \simeq \frac{45}{2\pi^4}\sqrt{\frac{\pi}{8}}\frac{g_X}{g_{*s}(x)} x^{\frac{3}{2}} e^{-x}, \tag{2.18}$$

where we assume $m \gg T$ to approximate DM number density. If we assume the radiation dominant universe, the Hubble constant, H, is expressed as follows.

$$H \equiv \sqrt{\frac{g_*(T)}{10}}\frac{\pi}{3M_{\text{pl}}}\frac{m^2}{x^2}. \quad (m \gg T) \tag{2.19}$$

We can solve Eq. (2.17) by giving g_{*s} as a function of T.

To read out the rough picture for the time evolution of DM number density, let us approximate g_{*s} to be constant and neglect the derivative of g_{*s} in Eq. (2.17).

$$\frac{x}{Y_X^{\rm eq}}\frac{dY_X}{dx} \simeq -\frac{\Gamma_X}{H}\left[\left(\frac{Y_X^2}{Y_X^{\rm eq}}\right)^2 - 1\right], \tag{2.20}$$

where we define the annihilation rate of DM as $\Gamma_X \equiv \langle\sigma v\rangle\, n_X$. From this approximated equation, we find the following behaviors of n_X in each epoch of the thermal history. First, in the early universe, we have plenty rate of all the interaction channels, production, annihilation, and scattering processes for DM. Therefore, the yield of DM is expressed in the form of a thermal equilibrium state, $Y_X \simeq Y_X^{\rm eq}$, and the RHS of Eq. (2.20) is negligible. Consequently, if the effect of the cosmic expansion is also negligible, the DM number density is approximately fixed to be a constant value. Second, as the temperature of the thermal bath gets decreased, it becomes more difficult to produce a pair of DM from the SM particles due to the lack of thermal energy. After DM production processes are forbidden kinematically, pair annihilation processes of DM only occur and decrease the number density of DM. As long as we have rapid scattering processes between DM and particles in the thermal bath, DM number density is expressed in the thermal equilibrium state. Therefore, the yield of DM decreases exponentially as the temperature decreases. Third, DM annihilation processes are forbidden if the cosmic expansion gets relevant and DM can not find an annihilation partner. After closing both production and annihilation processes, DM number density per comoving volume turns out to be constant. This succeeding thermal history of DM is called *freeze-out*, and the thermally abundant DM is called *thermal relic abundance*. We may estimate when the freeze-out occurs by comparing the typical time scale for DM pair annihilation $\sim 1/\Gamma_X$ and the cosmic age, $\sim 1/H$. Therefore, the condition for DM annihilation processes to be negligible is expressed below.

$$\Gamma_X/H \ll 1. \tag{2.21}$$

This condition implies that the RHS of Eq. (2.20) gets negligible and yield is again fixed to the constant value. The temperature where the freeze-out occurs, $T_{\rm fo}$, can be roughly estimated by reading out where $\Gamma_X/H \simeq 1$ is realized. We need to solve Eq. (2.17) numerically to precisely determine the DM number density in the current universe, which is one of the most important predictions of WIMP hypothesis.

2.2 Coannihilation

In the previous section, we gave general formalism to evaluate thermal relic abundance following the freeze-out mechanism. If we have a nearly degenerated mass spectrum in the DM system, the evaluation of the thermal relic abundance is affected by not only DM but also the heavier components. This effect is called *coannihilation* [15]. In particular, if the mass difference between DM and a heavier component is smaller than the freeze-out temperature of DM, the heavier component is still abundant in the thermal bath. Consequently, the

heavier component may also affect the number density of parity-odd particles, and the DM annihilation rate gets effectively increased. In this section, we review the general formalism to evaluate the thermal relic abundance in the system with viable coannihilation effects.

Let us consider the system with Z_2-odd charge, $\{\chi^i\}$ $(i = 1, 2, \cdots, n)$. This discrete symmetry stabilizes the lightest Z_2-odd particle and realizes a stable DM candidate. We assign the label i so that $m_1 < m_2 < \cdots < m_n$, and thus DM is χ^1. To simplify the notation, we use $m \equiv m_1$ to express DM mass. We also assume that χ^i has interaction channels with the SM particles. The relevant interactions conserving the Z_2 symmetry are listed below.

$$\chi^i\chi^j \to XX', \tag{2.22}$$
$$\chi^i X \to \chi^j X', \tag{2.23}$$
$$\chi^j \to \chi^i XX', \tag{2.24}$$

where X and X' denote the appropriate combination of the SM particles. Once we determine X, the other X' is automatically fixed depending on each interaction theory of DM. Thanks to the decay processes in Eq. (2.24), all the heavier components $\chi^j (j > 1)$ finally decay to the lightest component χ^1. Therefore, all we have to follow is the total number density n to evaluate the thermal relic abundance of DM.

$$n \equiv \sum_i n_i, \tag{2.25}$$

where n_i denotes the number density of χ^i.

We obtain the following Boltzmann equation for the i-th component by including the processes shown in Eqs. (2.22)-(2.24) on the RHS.

$$\begin{aligned}\frac{dn_i}{dt} + 3Hn_i = -\sum_{j,X}\Big[&\langle\sigma_{ij}v\rangle\,(n_in_j - n_i^{\rm eq}n_j^{\rm eq}) \\ &+ \left(\langle\sigma'_{ij}v\rangle\,n_in_X - \langle\sigma'_{ji}v\rangle\,n_jn_{X'}\right) \\ &+ \Gamma_{ij}(n_i - n_i^{\rm eq})\Big],\end{aligned} \tag{2.26}$$

where we introduce the following notation.

$$\sigma_{ij} \equiv \sigma(\chi^i\chi^j \to XX'), \tag{2.27}$$
$$\sigma'_{ij} \equiv \sigma(\chi^iX \to \chi^jX'), \tag{2.28}$$
$$\Gamma_{ij} \equiv \Gamma(\chi^i \to \chi^jXX'). \tag{2.29}$$

We assume that the SM particles are in the thermal equilibrium and relativistic at the freeze-out temperature. To obtain the Boltzmann equation for total number density, n, we take summation over i for Eq. (2.26) on both sides and obtain the following equation.

$$\frac{dn}{dt} + 3Hn = -\sum_{i=1}^{n}\sum_{j=1}^{n}\langle\sigma_{ij}v\rangle\,(n_in_j - n_i^{\rm eq}n_j^{\rm eq}), \tag{2.30}$$

where we define

$$\langle \sigma_{ij} v \rangle \equiv \left(\frac{m}{4\pi T}\right)^{3/2} \int dv 4\pi v^2 (\sigma_{ij} v) \exp\left(-\frac{m v^2}{4T}\right). \tag{2.31}$$

Note that the second and third terms on the RHS of Eq. (2.26) do not change the total number density, and thus these terms do not contribute to Eq. (2.30). Besides, the symmetric part of σ_{ij} only contributes to the equation. Since we assume the SM particle is relativistic near the freeze-out point, the number density of χ^i is exponentially suppressed compared to that of the SM particles. Therefore, the processes in Eq. (2.23), which thermalizes χ^i, are more relevant than the processes in Eq. (2.22). Consequently, we can approximately express the number density of χ_i as $n_i \simeq n_i^{\rm eq}$. For later convenience, we define the ratio of the number density.

$$r_i \equiv \frac{n_i^{\rm eq}}{n^{\rm eq}} = \frac{g_i (1+\Delta_i)^{\frac{3}{2}} e^{-x\Delta_i}}{g_{\rm eff}}, \tag{2.32}$$

where g_i denotes the internal degrees of freedom for χ^i. We also introduce the following variables.

$$\Delta_i \equiv \frac{m_i - m}{m}, \tag{2.33}$$

$$g_{\rm eff} \equiv \sum_{i=1}^{n} g_i (1+\Delta_i)^{\frac{3}{2}} e^{-x\Delta_i}. \tag{2.34}$$

Using the above expressions, we express Eq. (2.30) as shown below.

$$\frac{dn}{dt} + 3Hn = -\langle \sigma_{\rm eff} v \rangle \left(n^2 - n_{\rm eq}^2\right), \tag{2.35}$$

where effects of the coannihilation are imprinted in the effective annihilation cross section $\sigma_{\rm eff}$.

$$\langle \sigma_{\rm eff} v \rangle \equiv \sum_{i=1}^{n} \sum_{j=1}^{n} \langle \sigma_{ij} v \rangle \, r_i r_j \tag{2.36}$$

$$= \sum_{i=1}^{n} \sum_{j=1}^{n} \langle \sigma_{ij} v \rangle \, \frac{g_i g_j}{g_{\rm eff}^2} (1+\Delta_i)^{\frac{3}{2}} (1+\Delta_j)^{\frac{3}{2}} \exp\left[-x(\Delta_i + \Delta_j)\right]. \tag{2.37}$$

The physical meaning of r_i is stated below: If we have $T \lesssim m_i - m$, the ratio r_i for $i > 1$ is exponentially suppressed. This suppression represents the thermal decoupling of the heavier components. In the limit of high temperature, all the heavier components decouple from the thermal bath, and we obtain the following converged values.

$$g_{\rm eff} \to g_1, \quad \text{(internal degrees of freedom for DM)} \tag{2.38}$$

$$r_i \to \begin{cases} 1 & \text{for } i = 1, \\ 0 & \text{for } i > 1. \end{cases} \tag{2.39}$$

Therefore, we recover the results for DM annihilation cross section without degenerated spectrum and obtain the same Boltzmann equation derived in the previous section.

Before we move to the next section, we mention concrete situations where the coannihilation effects get viable. In this thesis, we consider spin-1/2 and spin-1 DM systems with the $\mathrm{SU}(2)_L$ triplet and $Y = 0$ electroweak interactions and study the possibility to discriminate these signatures. DM candidate corresponds to the neutral component of the $\mathrm{SU}(2)_L$ multiplet. We have typically $\mathcal{O}(100)$ MeV for the mass splitting between the neutral and the charged components originated from the electroweak radiative corrections. Another source of mass splitting is the higher dimensional operators that are suppressed by the cutoff scale. In particular, nonzero contributions to the mass splitting only appear from the operator that breaks $\mathrm{SU}(2)_L$ symmetry after the SM Higgs develop the Vacuum Expectation Values (VEV). The lowest operators are dimension seven for spin-1/2 DM and dimension eight for spin-1 DM, respectively. If we assume the cutoff scale is higher than $\mathcal{O}(10)$ TeV, the contribution from the higher dimensional operators get irrelevant and the electroweak radiative corrections dominate the mass splitting. Since the value of mass splitting is much smaller than the TeV scale DM mass, which is expected to reach the correct value of thermal relic abundance, the coannihilation effects are efficiently switched on. In Sec. 5, we will evaluate σ_{eff} in the system of electroweakly interacting DM.

3 Electroweakly interacting spin-1 DM

As reviewed in the previous section, the crucial constraint for the WIMP DM model is the thermal relic abundance. There are various possibilities on DM mass and interactions with the ordinary matter as long as the observationally fixed value $\Omega h^2 = 0.120 \pm 0.001$ is realized. We note that the velocity-weighted annihilation cross section for DM, $\langle \sigma v \rangle$, is the crucial parameter to characterize the prediction of DM abundance. To realize the observed DM energy density through the freeze-out scenario, we need the following value for the cross section.

$$\langle \sigma v \rangle \simeq 3 \times 10^{-26} \text{ cm}^3/\text{s}, \tag{3.1}$$

which is called *the canonical cross section*.

Electroweakly interacting DM is one of the promising and most studied WIMP theories. These DM candidates interact with the SM particles mainly through electroweak interactions. Under this assumption, we may estimate the DM annihilation cross section through a simple dimensional analysis.

$$\sigma v \simeq \frac{\alpha_2}{m_{\text{DM}}^2}, \tag{3.2}$$

where α_2 is the fine structure constant of the $\text{SU}(2)_L$ gauge group, and we assume that DM mass, m_{DM}, is the typical energy scale for DM annihilation processes. Requiring this cross section to be equal to the canonical cross section, we obtain the typical value for DM mass,

$$m_{\text{DM}} \simeq \mathcal{O}(100) \text{ GeV}, \quad \text{for } \alpha_2 \simeq 0.03, \tag{3.3}$$

and obtain the accidental coincidence of the scale and mass which are both typical for electroweak theory in the SM. This fact is called *WIMP miracle*, which is one of the greatest motivations to consider electroweakly interacting DM.

Although this electroweakly interacting DM hypothesis is simple and works well following the standard WIMP framework, we have one more nontrivial question: how to stabilize DM candidates with electroweak interactions. If we have no stabilization mechanism for TeV scale DM with electroweak interactions, DM may not survive in the current universe due to the short lifetime. One may simply assume the discrete symmetry for the dark sector. Some theoretical frameworks, motivated to solve the hierarchy problem, provide both DM stability and electroweak interactions for DM at the same time.

One possibility to stabilize electroweakly interacting DM is the R-parity in the supersymmetric scenario. The MSSM is the minimal supersymmetric model that realizes the SM spectrum at low energy. In this model, all the SM matter fields are extended to the chiral superfield while gauge bosons are promoted to the vector superfields. The Wino is the spin-1/2 superpartner of the $\text{SU}(2)_L$ gauge bosons in the vector superfield. Therefore, its electroweak charge is identical to that of gauge bosons, $\text{SU}(2)_L$ triplet with $Y = 0$. If the neutral component of the spin-1/2 triplet is the LSP, it may be a stable DM candidate and is called the Wino DM. Since the Wino DM has no Higgs coupling at the tree-level, electroweak

channels dominate interactions between the Wino DM and the SM particles. The tree-level mass m for electrically neutral and charged components are degenerated at the tree-level due to the triplet features. This degeneracy is broken by the radiative corrections between electroweak multiplets, and nonzero mass splitting is induced. This mass splitting, δm, is calculated at the two-loop level [16, 17, 18], and obtained as $\delta m \simeq 170$ MeV in the limit of $m \gg m_W$. This Wino DM scenario is one of the most studied WIMP DM candidates.

Another framework to stabilize electroweakly interacting DM is the KK-parity in extra-dimensional theories. Concrete models that predict electroweakly interacting spin-1 DM, which has the non-abelian vector couplings with electroweak bosons, are proposed. We will review this latter stabilization mechanism in the rest of this section. In Sec. 3.1, we review extra-dimensional theory and spin-1 DM candidates that are stabilized by the KK-parity. We also summarize properties of spin-1 DM such as couplings for spin-1 DM and mass spectrum in each model. In Sec. 3.2, we introduce a simplified spin-1 DM model that realizes essential features of KK electroweak boson DM of the extra-dimensional theory.

The goal of this work is to compare the predictions from the spin-1/2 and spin-1 DM candidates that have the $\mathrm{SU}(2)_L$ triplet and $Y = 0$ electroweak interaction. This comparison corresponds to the discrimination between the Wino DM and the KK electroweak boson DM. Let us add comments on the significance to discuss the discrimination of these scenarios: The Wino DM is indeed embedded in the *neutralino* DM, which is the mixing of the electrically neutral spin-1/2 fields, in a more general framework in the MSSM. The lightest spectrum can be the LSP DM candidate. In this sense, the Wino DM is a special limit of the general neutralino DM scenario where the LSP has purely $\mathrm{SU}(2)_L$ triplet features. Therefore, phenomenological studies focusing on the Wino DM are not enough. We have to study more general neutralino DM to conclude the possibility of discrimination between spin-1/2 DM candidate predicted in supersymmetric scenarios and spin-1 DM in extra-dimensional theories. Still, it is worth focusing on the Wino DM and the KK electroweak boson DM as benchmark scenarios to discuss separations. This is because discrimination between these DM candidates are highly non-trivial due to the same electroweak interactions with $\mathrm{SU}(2)_L$ triplet and $Y = 0$. It is essential to extract the spin-dependent features and signatures of these theories. In Sec. 6, we will discuss further how to detect spin-dependence in experimental observables.

3.1 Spin-1 DM candidate in extra-dimensional theory

If we have extra-dimensions, they should be compactified with the appropriate procedures so that we can not observe the higher dimensions. The procedures to construct a concrete model with extra-dimension(s) are summarized below.

1. Fix the number of extra-dimension(s)
2. Determine the metric for extra-coordinate(s)
3. Choose how to compactify extra-dimension(s)
4. Assign boundary conditions for each field to desire appropriate spectrum

Throughout this thesis, we focus on five dimensional theories: four ordinary dimensions ($\{x^\mu\}$ ($\mu = 0, 1, 2, 3$) to express these coordinates) and one extra dimension (y to express this coordinate). This is a minimal choice to realize a discrete symmetry originated from a geometric reflection of an extra-dimension. We also discuss some possibilities for metric of an extra-dimension. The simplest choice is a flat metric for the fifth coordinate, which is often mentioned as *universal*.

$$d^2s = d^2x + d^2y. \tag{3.4}$$

We may also consider a curved extra-dimension. The most well-studied setup is a `warped` metric. The warped metric is parameterized by the warp factor, k, which has mass dimension 1.

$$d^2s = d^2x + e^{-2ky}d^2y. \tag{3.5}$$

Using this warped metric, some models are constructed to address the hierarchy problems [19]. The geometric symmetry is different between the flat and curved metric, and thus the discrete symmetries are realized by the different mechanisms. The difference also appears in the mass spectrum through the possibly large boundary terms as discussed in Sec. 3.1.2 and Sec. 3.1.3.

The way of compactification is also important to realize the desired spectrum in low energy. The most nontrivial part is to realize chiral fermions. Besides, compactifications crucially determine the residual symmetry for the four dimensional theory. We may find a discrete symmetry that stabilizes a DM candidate. We review the above possibilities of model construction using simple toy models with an extra-dimension and summarize distinctive properties in each setup.

3.1.1 Universal Extra-Dimension

Let us start from the simplest example, which is called the *universal extra dimension*. In this setup, we consider a five dimensional theory with a flat metric shown in Eq. (3.4). The geometry of the fifth coordinate is *orbifold*, S^1/Z_2, where Z_2 means the identification of the point with y and $-y$. In other words, we require the theory to respect the parity symmetry under the $y \mapsto -y$. This discrete symmetry is called *y-parity*, In Fig. 1, we show the fifth coordinate with the orbifold compactification. After this identification, the fifth coordinate is mapped on the line segment of length $L = \pi R$. We have two boundaries on this line, $y = 0$ and $y = \pi R$, which are called *fixed points*. Each point is transformed into itself under the symmetry transformation of $y \mapsto -y$. These boundaries violate the translation invariance on the fifth coordinate, which is originally guaranteed by the flatness of extra-dimension.

The discrete symmetry is found in this setup with orbifold compactification in the following way. Since the fifth dimension is S^1, we have the following periodicity around the extra-dimensional coordinate.

$$y \simeq y + 2\pi R. \tag{3.6}$$

This is nothing but a U(1) symmetry, and this symmetry is exact before orbifolding. The fifth momentum is discretized due to this periodic boundary condition, and five dimensional

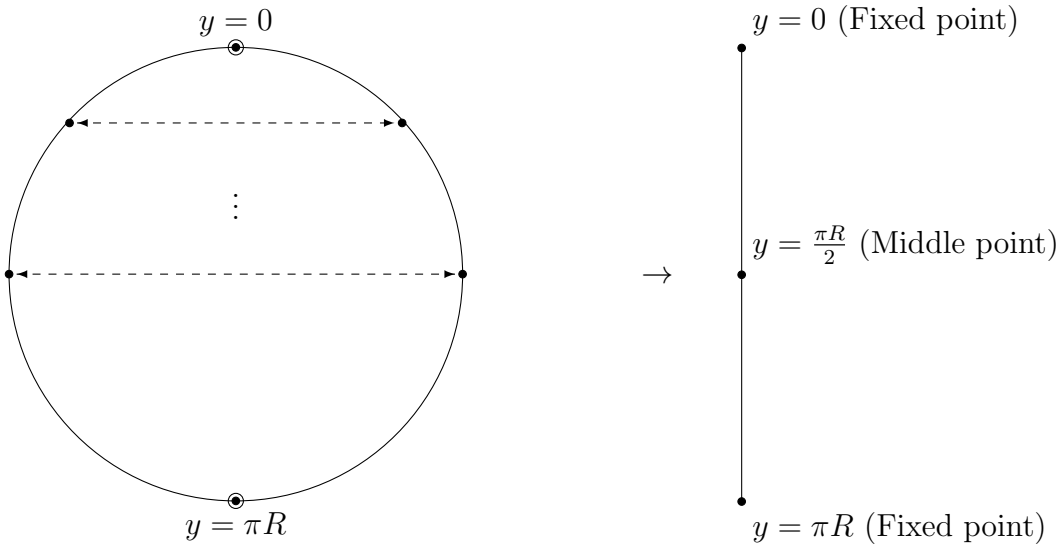

Figure 1: The fifth coordinate with the orbifold compactification.

fields are expanded into each mode, which is called *KK mode*, with momentum n/R ($n = 0, 1, 2, \cdots$). The conserved quantum number exists associated with the U(1) symmetry if the translation invariance is exact. This conserved number is called *KK number*. We have the discrete symmetry even after orbifolding, which corresponds to the invariance under the translation of πR in the y-direction. Expressing this translation within the domain of the fifth coordinate, $y \in [0, \pi R]$, this translation is equivalence to the flip of the line segment about its center at $y = \pi R/2$.

$$y \mapsto \pi R - y, \tag{3.7}$$

where we use the invariance under the $y \mapsto -y$ and $y \mapsto y + 2\pi R$. Note that we should assume the equivalent boundary localized interactions on two branes to maintain this KK parity exactly since $y = 0$ and $y = \pi R$ are exchanged with each other.

Respecting the above symmetries, we can expand the y-dependence of each field. The scalar field of five dimensional theory, $\Phi(x, y)$ is expressed as shown below.

$$\Phi_+^{KK}(x, y) = \sum_{n=0}^{\infty} \phi_+^{(n)}(x) f_+^{(n)}(y) = \frac{1}{\sqrt{\pi R}} \left\{ \phi_+^{(0)}(x) + \sqrt{2} \sum_{n=1}^{\infty} \phi_+^{(n)} \cos\left(\frac{y - \frac{\pi R}{2}}{R} n \right) \right\}, \tag{3.8}$$

$$\Phi_-^{KK}(x, y) = \sum_{n=0}^{\infty} \phi_-^{(n)}(x) f_-^{(n)}(y) = \sqrt{\frac{2}{\pi R}} \sum_{n=1}^{\infty} \phi_-^{(n)}(x) \sin\left(\frac{y - \frac{\pi R}{2}}{R} n \right), \tag{3.9}$$

where we use the following complete sets to expand y dependence.

$$f_+^{(0)}(y) = \frac{1}{\sqrt{\pi R}}, \tag{3.10}$$

$$f_+^{(n)}(y) = \sqrt{\frac{2}{\pi R}} \cos\left(\frac{y - \frac{\pi R}{2}}{R} n\right) \qquad (n = 1, 2, 3, \cdots), \tag{3.11}$$

$$f_-^{(n)}(y) = \sqrt{\frac{2}{\pi R}} \sin\left(\frac{y - \frac{\pi R}{2}}{R} n\right) \qquad (n = 1, 2, 3, \cdots). \tag{3.12}$$

The normalization factors are fixed to satisfy the following conditions.

$$\int_0^{\pi R} dy f_+^{(m)} f_+^{(n)} = \delta_{mn}, \qquad (m, n = 0, 1, 2, \cdots) \tag{3.13}$$

$$\int_0^{\pi R} dy f_-^{(m)} f_-^{(n)} = \delta_{mn}, \qquad (m, n = 1, 2, 3, \cdots) \tag{3.14}$$

$$\int_0^{\pi R} dy f_+^{(m)} f_-^{(n)} = 0. \qquad (m = 0, 1, 2, \cdots \text{ and } n = 1, 2, 3, \cdots) \tag{3.15}$$

Under the symmetry transformation shown in Eq. (3.7), $\phi_\pm^{(n)}$ transforms in the following way.

$$\phi_\pm^{(n)}(x) \mapsto \pm \phi_\pm^{(n)}(x). \tag{3.16}$$

The zero mode $\phi_+^{(0)}$, which is constant, obviously transforms as even fields. We also note that these parity assignments directly correspond to the choice of boundary conditions for the fifth coordinate as found in Eqs. (3.8)-(3.9). If we have no boundary localized terms, we obtain two types of natural boundary conditions by requiring that all the boundary terms vanish. In particular, we can choose ϕ_+ or ϕ_- by switching these boundary conditions.

$$\phi_+^{(n)}(x)\Big|_{0,\pi R} = 0, \qquad \text{(Neumann boundary condition)} \tag{3.17}$$

$$\partial_y \phi_-^{(n)}(x)\Big|_{0,\pi R} = 0. \qquad \text{(Dirichlet boundary condition)} \tag{3.18}$$

Since the four dimensional Lagrangian is obtained after performing the y integral, the coefficients $\{\phi_\pm^{(n)}\}$ correspond to the four dimensional fields. Therefore, the KK-parity is nothing but the Z_2-parity realization for the four dimensional fields as shown in Eq. (3.16). We also note that the KK number is conserved in all the interactions of the four dimensional theory due to the orthogonal relation between $\{f_\pm^{(n)}\}$.

The higher KK modes with $n \geq 1$ acquire $\mathcal{O}(n/R)$ mass from the kinetic term of the fifth component, while the zero mode does not. Therefore, we have a mass gap characterized by $\sim 1/R$ between zero mode and higher KK modes. Making use of this property, we identify the SM particles as zero modes in the KK expansion of each five dimensional field to realize the observed SM spectrum in low energy while higher KK modes tend to decouple from the

low energy physics. Since a zero mode only exists in KK-even modes, we may switch on and off each field to realize the observed spectrum by choosing boundary conditions.

The SM spectrum realization in the flat five dimensional theory is proposed and studied in Ref. [20]. In this model, all the SM fields are promoted to the field in a five dimensional theory. We prepare field contents and assign appropriate boundary conditions to realize the SM spectrum. For the scalar sector, we assign the Neumann boundary condition to realize a zero mode for the SM Higgs.

$$H(x,y) = \frac{1}{\sqrt{\pi R}}\left\{ H^{(0)}(x) + \sqrt{2}\sum_{n=1}^{\infty} H^{(n)} \cos\left(\frac{ny}{R}\right)\right\}, \tag{3.19}$$

For gauge fields, we assign different boundary conditions for $\mu = 0,1,2,3$ components and y component. The y component behaves as the Lorentz scalar under the SO(1,3) Lorentz transformation and is eaten by the KK modes with $n \geq 1$ through the Higgs mechanism in the five dimensional theory. Therefore, we only have a zero mode as a physical degree of freedom. We switch off the zero mode by assigning the Dirichlet boundary condition to avoid extra scalar degrees of freedom in the low energy. The Neumann boundary condition is assigned for $\mu = 0,1,2,3$ components to realize zero modes that behave as the Lorentz four vectors. Imposing the above boundary conditions, we obtain the following expression for the gauge field.

$$A_\mu(x,y) = \frac{1}{\sqrt{\pi R}}\left\{ A_\mu^{(0)}(x) + \sqrt{2}\sum_{n=1}^{\infty} A_\mu^{(n)} \cos\left(\frac{ny}{R}\right)\right\}, \tag{3.20}$$

$$A_5(x,y) = \sum_{n=1} A_5^{(n)}(x)\sqrt{\frac{2}{\pi R}} \sin\left(\frac{ny}{R}\right). \tag{3.21}$$

The physical degrees of freedoms are $A_\mu^{(n)}$ and the KK modes with $n \geq 1$ acquire masses of $\mathcal{O}(n/R)$.

In the five dimensional theory, we need to consider vector like fermions to realize the fermion mass term. To show this fact, we write down the kinetic term for a fermion field in the fifth dimensional theory. The five dimensional Gamma matrices are expressed as shown below.

$$\{\Gamma^M, \Gamma^N\} = 2\eta^{MN}. \quad (M,N = 0,1,2,3,y) \tag{3.22}$$

We choose the following four-times-four representation as shown below.

$$\Gamma^\mu \equiv \gamma^\mu, \qquad\qquad \Gamma^5 = i\gamma^5, \tag{3.23}$$

where

$$\Gamma^\mu = \begin{pmatrix} 0 & \sigma^\mu \\ \sigma^\mu & 0 \end{pmatrix}, \qquad\qquad \Gamma^5 = \begin{pmatrix} -i\mathbf{1} & 0 \\ 0 & i\mathbf{1} \end{pmatrix}, \tag{3.24}$$

where we define $\sigma^\mu \equiv (1, \sigma^i)$. The fermion fields are also expressed in four component spinor representations. From Eq. (3.24), we are no longer able to perform the chiral projection for the five dimensional fermion. We use γ^5 for the chiral projection in the four dimensional theory using $P_R = (1+\gamma^5)/2$ and $P_L = (1-\gamma^5)/2$. However, in the five dimensional theory, we need γ^5 to realize the Clifford algebras and can not define the projection operator into two different chiralities. In other words, the kinetic terms can not be decomposed into the left-hand field and the right-hand field. This can be shown by using the following notation for the four component fermion.

$$\Psi(x,y) = \begin{pmatrix} \psi_L(x,y) \\ \psi_R(x,y) \end{pmatrix}, \tag{3.25}$$

and the kinetic term is decomposed into the following expression.

$$\bar{\Psi} i\partial\!\!\!/ \Psi = \psi_R^\dagger i\partial_\mu \sigma^\mu \psi_R + \psi_L^\dagger i\partial_\mu \bar{\sigma}^\mu \psi_L + \psi_R^\dagger \partial_y \psi_L - \psi_L^\dagger \partial_y \psi_R. \tag{3.26}$$

We find the left-handed and right-handed fermions are coupled in the last two terms, which is necessary to realize the fifth kinetic terms. The SM is a chiral theory where left-handed field and right-handed field are assigned to the different gauge assignments. To realize the chiral fermion in the five dimensional theory, the following two methods are often discussed: (1) introducing chiral fermions on boundaries and (2) imposing the orbifold compactification. Both of these methods break the five dimensional Lorentz invariance. If we choose the latter solution, we may realize the KK-parity by requiring the equivalent boundary terms on boundaries. Besides, we can switch off and on zero modes by assigning appropriate boundary conditions, which is crucial to realize four dimensional chiral fermions from five dimensional theories. In particular, we introduce vector like fermion fields, corresponding to each of the SM fermions, and assign the Neumann (Dirichlet) boundary condition for the fermion with

correct (wrong) chirality. Under this setup, we obtain the following expressions.

$$Q(x,y) = \frac{1}{\sqrt{\pi R}}\left\{ P_L Q^{(0)}(x) + \sqrt{2}\sum_{n=1}^{\infty} P_L Q^{(n)} \cos\left(\frac{ny}{R}\right)\right\} + \sum_{n=1} P_R Q^{(n)}(x)\sqrt{\frac{2}{\pi R}}\sin\left(\frac{ny}{R}\right), \tag{3.27}$$

$$u(x,y) = \frac{1}{\sqrt{\pi R}}\left\{ P_R u^{(0)}(x) + \sqrt{2}\sum_{n=1}^{\infty} P_R u^{(n)} \cos\left(\frac{ny}{R}\right)\right\} + \sum_{n=1} P_L u^{(n)}(x)\sqrt{\frac{2}{\pi R}}\sin\left(\frac{ny}{R}\right), \tag{3.28}$$

$$d(x,y) = \frac{1}{\sqrt{\pi R}}\left\{ P_R d^{(0)}(x) + \sqrt{2}\sum_{n=1}^{\infty} P_R d^{(n)} \cos\left(\frac{ny}{R}\right)\right\} + \sum_{n=1} P_L d^{(n)}(x)\sqrt{\frac{2}{\pi R}}\sin\left(\frac{ny}{R}\right), \tag{3.29}$$

where indices of generations are implicit and $f_L(f_R)$ denotes the left-handed (right-handed) fermion field.

We omit the boundary localized term in the above argument. However, we need to include the boundary localized term in the orbifold theory because the coefficients of boundary localized terms receive the infinite loop corrections. In Ref. [21], one-loop calculations in the five dimensional Yukawa theory are performed, and they showed the boundary interactions acquire divergent corrections. This result implies that the boundary localized terms are necessary to renormalize couplings, and thus it is inconsistent NOT to include these boundary terms in the orbifold theory. These parameters are incalculable and treated as free parameters in the theory, which also receive the corrections from the physics beyond the cut off scale as well as the calculable radiative corrections. Therefore, it is worth discussing the physical effects of the boundary localized terms. As mentioned above, if we have nonzero boundary localized terms, the translation invariance for the fifth direction is broken. Therefore, these boundary terms cause the KK number violation. However, if the boundary localized terms are suppressed by some mechanism the KK number conservation can be the approximate symmetry.

In the analysis called *Minimal Universal Extra Dimension* (MUED), it is assumed that the boundary localized terms respect the reflection symmetry about the middle point of the line segment. Under this setup, we have the exact KK-parity symmetry, and thus the LKP turns out to be a stable DM candidate. It is also assumed that we have no boundary localized term at the cutoff scale, which is a free parameter in this setup, and all the boundary localized terms are induced through the renormalization group evolution. Consequently, boundary lo-

calized terms always appear with loop suppression factors and the KK number conservation is still good symmetry. In this MUED approach, the radiative corrections are well-defined and calculable without cutoff dependence. The point is that the finite mass corrections are only induced by the non-local effects, which have nonzero winding numbers around the compactified finite fifth dimension. Therefore, we obtain the finite loop amplitude by subtracting the corresponding amplitude in uncompactified theory. This subtraction formula is proposed by Ref. [22], and the mass splitting for the SM spectrum in the MUED model is calculated at the one-loop level. According to their analysis, the KK photon turns out to be the LKP and stable DM candidate. Therefore, the DM candidate in the MUED approach has no electroweak interactions.

3.1.2 Minimal Universal Extra-Dimension

This situation drastically changes if we consider relatively large boundary localized terms as pointed out in Ref. [10]. To demonstrate the effects of boundary localized terms on the mass spectrum, let us consider a simple scalar theory with relatively large boundary localized terms.

$$S = S_{\rm bulk} + S_{\rm bound}, \tag{3.30}$$

where

$$S_{bulk} = \frac{1}{2}\int d^5x \left(\partial^M\Phi\partial_M\Phi - m^2\Phi^2\right), \tag{3.31}$$

$$S_{bound} = \frac{1}{2}\int d^5x \left(r_\Phi\partial^M\Phi\partial_M\Phi - m_b^2\Phi^2\right)\left[\delta(y) + \delta(y-\pi R)\right]. \tag{3.32}$$

In Eq. (3.32), we introduced dimension full parameters, r_Φ (mass dimension -1) and m_b^2 (mass dimension 1), to characterize the boundary localized terms. Due to the finite fifth dimension, the boundary contributions are induced by the partial integral. We obtain the following equation of motion,

$$\left(\Box - \partial_y^2 + m^2\right)\Phi = 0, \tag{3.33}$$

and boundary conditions.

$$\left(\partial_5 - r_\Phi\Box - m_b^2\right)\Phi\Big|_{y=0} = 0, \tag{3.34}$$

$$\left(\partial_5 + r_\Phi\Box + m_b^2\right)\Phi\Big|_{y=\pi R} = 0. \tag{3.35}$$

We expand the field using a complete set of functions.

$$\Phi_\pm(x) = \sum_n \phi_\pm^{(n)}(x) f_\pm^{(n)}(y). \tag{3.36}$$

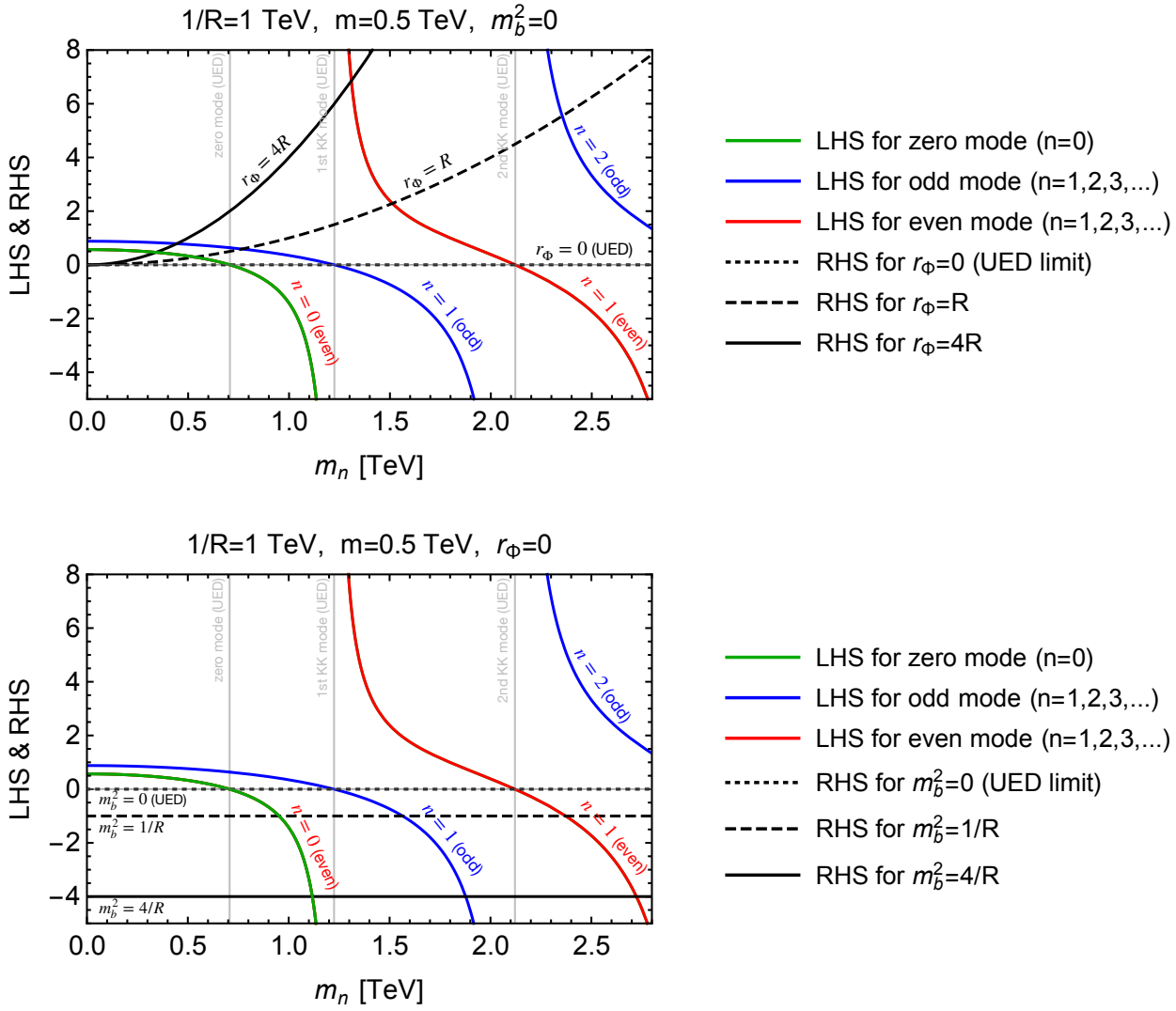

Figure 2: Plots of quantization conditions with nonzero boundary terms. The solution corresponds to the intersection of black and colored curves. The green, blue, and red curves show RHSs of zero modes ($n = 0$), even modes ($n \geq 1$), and odd modes ($n \geq 1$) in each panel. The intersections with the black dashed line in each panel show the UED solutions where we switch off all the boundary localized terms. In the upper panel, we fix $m_b^2 = 0$ and change the value of r_Φ. The black dotted, black dashed, and black solid curves show the RHS of Eq. (3.39) with $r_\Phi = 0, R$, and $4R$, respectively. In the lower panel, we fix $r_\Phi = 0$ and change the value of m_b^2. The black dotted, black dashed, and black solid curves show the RHS of Eq. (3.39) with $m_b^2 = 0, 1/R$, and $4/R$, respectively.

If we expand the trigonometric function to expand the y dependence,[1] we obtain the following relation from Eq. (3.33).

$$M_n^2 \equiv \left(\frac{n}{R}\right)^2 = m_n^2 - m^2, \tag{3.37}$$

where m_n denotes the mass eigenvalue of the four dimensional Proca equation for the n-th KK mode.

$$\left(\Box + m_n^2\right) \Phi^{(n)}(x) = 0. \tag{3.38}$$

The quantization conditions in Eq. (3.34) and Eq. (3.35) give the following constraint on m_n.

$$r_\Phi m_n^2 - m_b^2 = \begin{cases} -M_n \tan\left(\frac{M_n \pi R}{2}\right), & \text{(even)} \\ \\ M_n \cot\left(\frac{M_n \pi R}{2}\right). & \text{(odd)} \end{cases} \tag{3.39}$$

Since we consider relatively large boundary localized terms, we can not treat these parameters perturbatively. Consequently, quantization conditions are altered, which also affects the mass spectrum for the four dimensional fields.

In Fig. 2, we show the plots of the LHS and the RHS of the quantization conditions with nonzero boundary kinetic terms. In each panel, the solution corresponds to the intersection of black and colored curves. The black curves show the LHS. The green, blue, and red curves show the RHS of zero modes ($n = 0$), even modes ($n \geq 1$), and odd modes ($n \geq 1$) in each panel, respectively. If we switch off all the boundary localized terms, the LHS turns to be zero as shown in the black dashed lines in each panel, which corresponds to the UED case. Therefore, the intersections with the black dashed lines show the UED solutions. In the upper panel, we fix $m_b^2 = 0$ and change the value of r_Φ. The black dotted, black dashed, and black solid curves show the RHS of Eq. (3.39) with $r_\Phi = 0, R$, and $4R$, respectively. In the lower panel, we fix $r_\Phi = 0$ and change the value of m_b^2. The black dotted, black dashed, and black solid curves show the RHS of Eq. (3.39) with $m_b^2 = 0, 1/R$, and $4/R$, respectively. If we take a limit of $m^2 \to 0$, the solutions saturate to be $m_n = 0, 1/R, 2/R, \cdots$ in the UED case. Due to the trigonometric profile, the RHSs for $n = 0$ (even) and $n = 1$ (odd) modes have different behaviors. Consequently, we obtain the anomalously lighter mass for the lightest zero mode and the first KK mode compared with the second KK mode and higher modes.

The solutions of m_n and their dependence on the boundary localized terms are shown in Fig. 3. The UED limit for m_n are shown by gray horizontal lines in each panel. We take $1/R = 1$ TeV$, m = 0.5$ TeV, and $m_b^2 = 0$ in the upper figure and shows r_Φ-dependence of m_n. The boundary localized kinetic terms cause the drastic change of the mass splitting due to the trigonometric profiles. We take $1/R = 1$ TeV$, m = 0.5$ TeV, and $r_\Phi = 0$ in the lower figure and shows m_b^2-dependence of m_n. The boundary localized mass terms cause almost the overall shift since the LHS is shifted perpendicular to the y-axis. From this discussion

[1]The KK number conservation is broken if we introduce the large boundary localized term. Therefore, another choice of the functional basis is the hyperbolic functions to expand the even and odd function $\{f_\pm^{(n)}\}$ as discussed in Ref. [10].

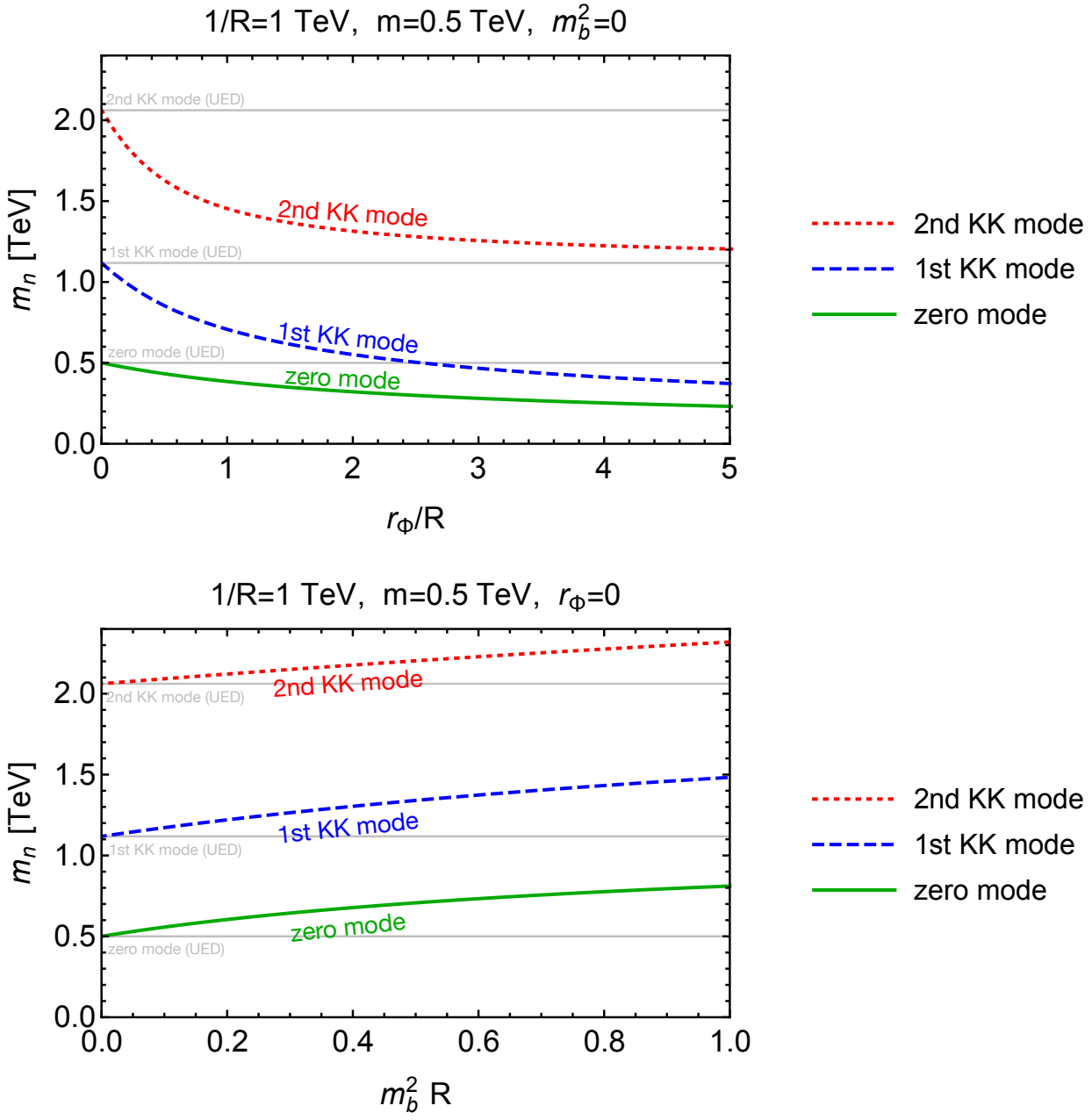

Figure 3: Plots of m_n in the non-MUED approach. The green solid, blue dashed, and red dotted curves show the zero mode, 1st KK mode, and 2nd KK mode, respectively. In the upper panel, we fix $m_b^2 = 0$ and change the value of r_Φ on the x-axis. In the lower panel, we fix $r_\Phi = 0$ and change the value of m_b^2 on the x-axis.

using the simple toy model, we find the mass spectrum will be drastically changed from the UED scenario if we introduce boundary localized terms. In particular, the boundary localized kinetic term may realize an anomalously lighter first KK mass compared with the UED results.

We also note that the mass spectrum is not taken to be completely free even though we take the arbitrary values of the boundary localized parameters. The most remarkable feature is a mass relation between the first KK mode and the second KK mode. As can be seen from Fig. 3, the first KK mass can be even lighter than zero mode mass in the UED setup while the second KK mass is bounded by the first KK mass in the UED setup. Consequently, we have $m^{(\mathrm{2nd})} > 2m^{(\mathrm{1st})}$ in the whole range of plots in this non-MUED scenario.

According to Ref. [10], the KK mode for the electroweak neutral boson may be LKP if we consider the large boundary localized term for the electroweak bosons. The KK parity is still exact symmetry by assuming the same boundary localized term on each boundary. Therefore, this first KK electroweak boson can be a stable spin-1 DM candidate with the electroweak couplings of $\mathrm{SU}(2)_L$ triplet. The model construction and the dedicated phenomenological studies are done by Ref. [12]. The KK number violation may be significant in this non-MUED scenario since we consider relatively large boundary localized terms.

3.1.3 Warped Extra-Dimension

Let us consider one more example to construct the extra-dimensional DM model with the curved metric. In this case, the translation symmetry in the y axis does not exist from the beginning. However, we are still able to realize the KK-parity in this curved extra-dimension case such as the warped extra-dimension model. Note that the KK-parity is originated from the geometric reflection symmetry about the middle point of extra dimensional coordinate. To realize this symmetry, the symmetric warped metric is considered in Ref. [19].

$$d^2s = d^2x + e^{-2k|y|}d^2y. \tag{3.40}$$

In particular, the extra-dimensional coordinate is on $y \in [-L, L]$ and symmetric under reflection about $y = 0$. Since this theory respects the reflection symmetry, we realize the discrete symmetry corresponding to the KK parity in the UED model as long as we assume the boundary localized terms are the same at the boundary point, $y = -L$ and $y = L$. To illustrate the effects of the boundary localized term in this setup, we review the abelian gauge theory following Ref. [19].

$$\begin{aligned}\mathcal{L} = -\int d^4x \int_{-L}^{L} dy\sqrt{-g}\frac{1}{4g_5^2}\Big[&F^{MN}F_{MN} + 2r_{\mathrm{UV}}F^{\mu\nu}F_{\mu\nu}\delta(y) \\ &+ 2r_{\mathrm{IR}}F^{\mu\nu}F_{\mu\nu}\delta(y-L) + 2r_{\mathrm{IR}}F^{\mu\nu}F_{\mu\nu}\delta(y+L)\Big],\end{aligned} \tag{3.41}$$

where we define $F_{MN} \equiv \partial_M A_N - \partial_N A_M$. The determinant of the metric shown in Eq. (3.40) is denoted by g, and thus we can express $\sqrt{-g}$ as follows.

$$\sqrt{-g} = a^4(|y|). \tag{3.42}$$

where we introduce a warp factor $a(y) \equiv e^{-ky}$. We also introduce g_5 as a gauge coupling (mass dimension $-1/2$) of the five dimensional theory. This action is invariant under $y \to -y$. Using this reflection symmetry about $y = 0$, we can rewrite Eq. (3.41) as shown below.[2]

$$\mathcal{L} = -\int d^4x \int_0^L dy \sqrt{-g} \frac{1}{4\tilde{g_5}^2} \Big[F^{MN} F_{MN} + 2r_{\rm UV} F^{\mu\nu} F_{\mu\nu} \delta(y) \tag{3.43}$$

$$+ 2r_{\rm IR} F^{\mu\nu} F_{\mu\nu} \delta(y - L) \Big], \tag{3.44}$$

where the factor of $1/2$ comes from the integral of $y \supset [-L, 0]$ is absorbed in the squared gauge coupling, $\tilde{g_5}^2 \equiv g_5^2/2$. This action reduced to the single-slice AdS_5 with the gauge coupling $\tilde{g_5} = g_5/\sqrt{2}$. We again expand the five dimensional gauge field using the complete set of the function.

$$A_{\mu\pm}(x) = \sum_n A^{(n)}_{\mu\pm}(x) f^{(n)}_{\pm}(y). \tag{3.45}$$

The F^{MN} is defined as below.

$$F^{\mu\nu} \equiv F_{\rho\sigma} g^{\rho\mu} g^{\sigma\nu} = F_{\rho\sigma} \eta^{\rho\mu} \eta^{\sigma\nu} a^{-4}(|y|), \tag{3.46}$$

$$F^{\mu 5} \equiv F_{\rho\tau} g^{\rho\mu} g^{\tau 5} = F_{\rho\tau} \eta^{\rho\mu} \eta^{\tau 5} a^{-2}(|y|), \tag{3.47}$$

Using these definition, we obtain the following equation of motion.

$$\partial_y \left(e^{-2y} \partial_y f^{(n)}_{\pm}(y) \right) + m_n^2 f^{(n)}_{\pm}(y) = 0. \tag{3.48}$$

The orthogonal relation is modified by the boundary localized terms.

$$\frac{1}{\tilde{g_5}^2} \int_0^L dy \left[1 + 2r_{\rm UV} \delta(y) + 2r_{\rm IR} \delta(y - L) \right] f^{(m)}(y) f^{(n)}(y) = \delta_{mn}, \tag{3.49}$$

where the indices for $\pm$ are implicit. This condition realizes the canonical kinetic term for the four dimensional gauge field. The boundary conditions are obtained as below.

$$e^{-2kL} \partial_y f^{(n)}_{\pm}(L) = m^2_{n\pm} r_{\rm IR} f^{(n)}_{\pm}(L), \tag{3.50}$$

$$\partial_y f^{(n)}_{+}(0) = -m^2_{n+} r_{\rm UV} f^{(n)}_{+}(0), \tag{3.51}$$

$$f^{(n)}_{-}(0) = 0, \tag{3.52}$$

where we impose the Neumann boundary condition for $L = R$ to realize the zero mode while we have two choices for the boundary condition for $L = 0$. We use $(-+)$ and $(++)$ to express the parity of the wave function profiles on $(y = 0, y = \pm L)$ under $y \mapsto -y$, which are

[2]The Chern-Simons term is Z_2 odd if exist in five dimensional theory. Therefore, this violation term may affect the stability of LKP [23]. The Chern-Simons term could arise in the presence of brane-localized anomalies as studied in Ref. [24]. In the analysis of Ref. [19], they assume that all the brane-localized anomalies cancel.

Table 1: Summary table of the DM candidate, mass spectrum, and the KK number conservation in each extra-dimensional DM model.

Scenario	DM candidate	mass spectrum	KK number
MUED	first KK mode for photon	$m^{(2\text{nd})} \simeq 2m^{(1\text{st})}$	conserved
non-MUED	eg. first KK mode for electroweak boson	$m^{(2\text{nd})} > 2m^{(1\text{st})}$	violated
Warped	eg. first KK mode for electroweak boson	$m^{(2\text{nd})} \lesssim 2m^{(1\text{st})}$	violated

determined by the continuity condition. We obtain two towers of modes corresponding to $(-+)$ and $(++)$ modes, which are KK-odd and KK-even, respectively. We have a massless mode for $(++)$ tower realized independent of the boundary localized terms. Besides, we have two interlacing mass spectra that is originated from both $(-+)$ and $(++)$ modes. These modes start at $\sim m_{\rm KK} \equiv ke^{-kL}$. In the limit of $r_{\rm IR} \ll 1/k$, we can read out the following approximated mass spectrum for the lightest even and odd modes, respectively.

$$m_{1-}^2 \simeq \frac{2}{kr_{\rm IR}} m_{\rm KK}^2, \tag{3.53}$$

$$m_{1+}^2 \simeq \frac{r_{\rm UV} + r_{\rm IR} + L}{r_{\rm UV} + L} \frac{2}{kr_{\rm IR}} m_{\rm KK}^2. \tag{3.54}$$

The mass relation is obtained depending on the boundary parameters.

$$\frac{m_{1+}}{m_{1-}} \simeq \sqrt{1 + \frac{r_{\rm IR}}{r_{\rm UV} + L}}, \tag{3.55}$$

which guarantees that $m_{1+} \gtrsim m_{1-}$. The mass splitting between these modes is controlled by the boundary kinetic terms. In particular, the value of $r_{\rm IR}$ compared to L tunes, in principle, arbitrary values of mass splitting. From this fact, we have wider possibilities in the mass spectrum depending on the boundary localized terms than the case in the non-MUED setup. The mass spectrum is no longer equally separated by $1/R$, and we may have $m^{(2\text{nd})} \lesssim 2m^{(1\text{st})}$ depending on the boundary localized terms. Besides, we have no KK number conservation from the beginning in this setup, and there is no reason to consider the suppressed boundary localized terms.

In Table 1, we summarize the features of the spin-1 DM candidates in each extra-dimensional scenario. An electroweakly interacting spin-1 DM candidate is predicted in both non-MUED and warped extra-dimension cases, but mass relations differ due to the difference in quantization conditions. For the warped extra-dimension, we may have $m^{(2\text{nd})} \lesssim 2m^{(1\text{st})}$ and the KK number violation. If these conditions are satisfied at the same time, we may have new annihilation channels for a pair of first KK modes into zero mode and the second KK mode as shown in Fig. 4. We will consider phenomenological implications of this possible new annihilation channel in the succeeding sections.

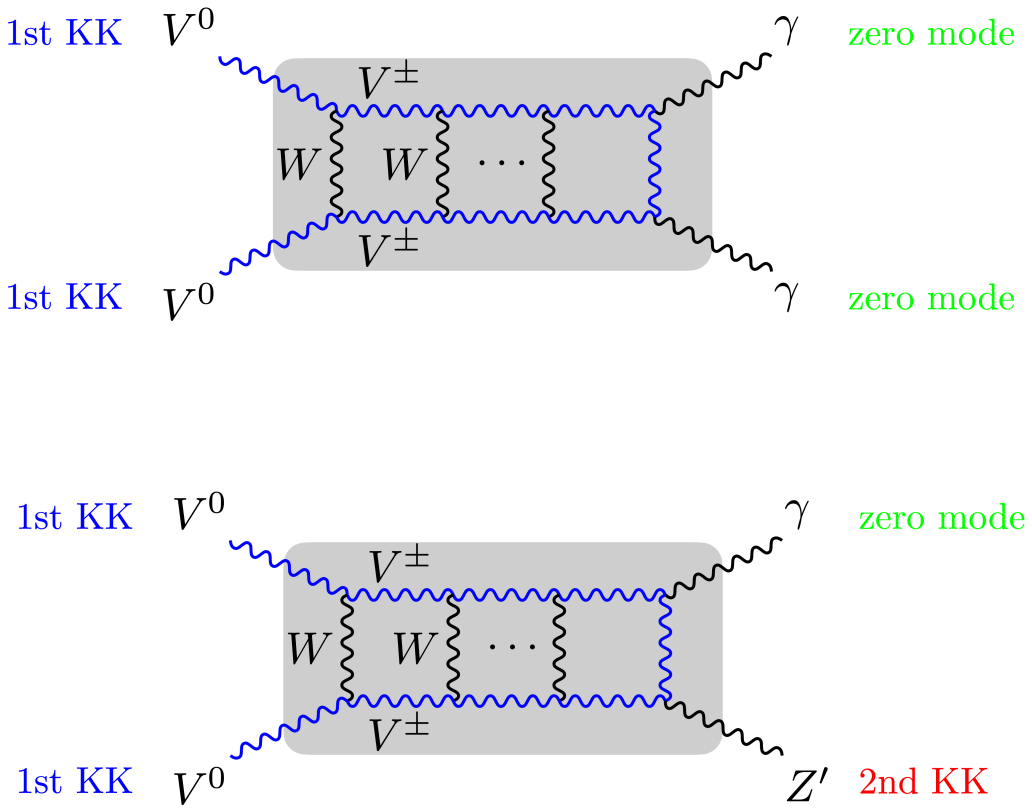

Figure 4: Examples for spin-1 DM annihilation diagrams into two vectors. The upper diagram shows annihilation into $\gamma\gamma$ (zero mode + zero mode) where the KK number is conserved. The lower diagram shows annihilation into $\gamma Z'$ (zero mode + second KK mode), which we need $m_{Z'} \leq 2m_V$ and the KK number violation.

Since we have wide possibilities in the mass spectrum, it is useful to perform the simplified model analysis to reveal the phenomenology of spin-1 DM as general as possible. In the next section, we introduce the spin-1 DM models that realize a similar spectrum as theories with an extra-dimension. We will also review relations and correspondence between our simplified model and the extra-dimensional model.

3.2 Non-abelian vector DM model

As revealed in Sec. 3.2, the mass spectrum and the interaction channels depend on the setup of extra-dimensional models such as the metric and the boundary localized terms. Since these variables directly affect the quantization condition of extra dimensions that give physical mass spectrum. There are various possibilities for DM candidates as listed in Table 1. One interesting possibility is that the first KK mode for the electroweak boson turns out to be LKP, which appears in the non-MUED and the warped metric models. DM candidate is $\mathrm{SU}(2)_L$ triplet spin-1 particle in this case, and thus electroweak features may crucially determine the procedure to test this scenario. The value of DM mass where we reach the

correct thermal relic abundance tends to be heavier since non-abelian vector electroweak interactions realize a larger number of DM annihilation channels. Throughout this thesis, we will focus on the possibility that the first KK mode for the electroweak bosons is a stable DM candidate.

We have two stabilization mechanisms for electroweakly interacting DM: R-parity in the supersymmetric scenario and KK-parity in the extra-dimensional scenario. We may construct models making use of each mechanism and have two DM candidates with the same electroweak interactions but with different spins, the Wino DM (spin-1/2) and electroweak KK boson (spin-1). It is important to discriminate the signatures from two DM candidates because these candidates are directly related to the scenarios where we can address the SM hierarchy problems.

For the spin-1 DM scenario, the mass relation between the first KK mode and the second KK mode is important to reveal phenomenology. Annihilation modes into not only the SM particles but also the final states including a second KK particle will be predicted if we have $m^{(\mathrm{2nd})} > m^{(\mathrm{1st})}$ and the KK number violation. This situation will be realized in the warped extra dimension. DM annihilation processes are crucial to determine the thermal relic prediction and the annihilation signatures in the current universe. To reveal the non-abelian vector DM features as general as possible, we use a simplified model that realizes the following features for DM predicted in a five dimensional setup.

- Z_2 parity assignment for physical spectrum
- $\mathrm{SU}(2)_L$ triplet spin-1 particles
- general mass spectrum for spin-1 particles

The simplest model, *non-abelian spin*-1 *DM*, is proposed in Ref. [25], which is constructed by the inspired method of the deconstructing dimension [26, 27]. This method realizes the mass spectrum of a five dimensional theory in the setup of four dimensional theory. In particular, we consider the theory with many direct products of gauge symmetries and impose the exchange symmetry between the gauge groups, which realizes the parity symmetry corresponding to the KK parity in extra-dimensional theories. The original formalism chooses the non-linear representation for the scalar fields, and thus the theory is not renormalizable. Our model, on the other hand, is renormalizable since the linear representation is applied for the scalar fields. We can still realize a similar mass spectrum as five dimensional setups through the spontaneous symmetry breaking in the scalar sector. Consequently, we have Z_2-odd physical spectra in the electroweak vector sector, which corresponds to the KK DM candidate in the context of the extra-dimensional theory.

3.3 Simplified model of spin-1 DM in extra-dimensional theory

Let us show the detailed setup of the electroweakly interacting vector DM model proposed in Ref. [25]. The gauge symmetry is extended into

$$\mathrm{SU}(3)_c\times\ \mathrm{SU}(2)_0\times\ \mathrm{SU}(2)_1\times\ \mathrm{SU}(2)_2\times\ \mathrm{U}(1)_Y, \tag{3.56}$$

where $\mathrm{SU}(3)_c$ and $\mathrm{U}(1)_Y$ corresponds to the color and hypercharge symmetry in the SM. Note that $\mathrm{SU}(2)_L$ symmetry in the SM is promoted into the three direct products of SU(2) gauge groups. The gauge bosons for $\mathrm{SU}(2)_0$, $\mathrm{SU}(2)_1$, $\mathrm{SU}(2)_2$, and $\mathrm{U}(1)_Y$ are denoted as $W^a_{0\mu}$, $W^a_{1\mu}$, $W^a_{2\mu}$, and B_μ, respectively ($a = 1, 2, 3$). The gauge couplings for each symmetry are denoted as g_0, g_1, g_2, and g', respectively. In Table 2, we summarize the matter fields and Higgs fields. Each fermion field corresponds to the SM fermion with the same $\mathrm{SU}(3)_c$ and $\mathrm{U}(1)_Y$ charge assignment. To reduce the extended electroweak symmetry, we introduce bi-fundamental scalar fields, Φ_j ($j = 1, 2$), expressed as two-by-two matrices. The real conditions are imposed for Φ_j to reduce the degrees of freedom.

$$\Phi_j = -\epsilon \Phi_j^* \epsilon, \quad \text{where} \quad \epsilon = \begin{pmatrix} 0 & 1 \\ -1 & 0 \end{pmatrix}. \tag{3.57}$$

Thanks to this condition, each of Φ_j contains four real degrees of freedom. The gauge transformations for Φ_j and H are expressed below.

$$\Phi_1 \mapsto U_0 \Phi_1 U_1^\dagger, \qquad \Phi_2 \mapsto U_2 \Phi_2 U_1^\dagger, \qquad H \mapsto e^{i\theta_Y} U_1 H, \tag{3.58}$$

where U_n denote the two-by-two matrices for the gauge transformation of $\mathrm{SU}(2)_n$ symmetry ($n = 0, 1, 2$) and θ_Y denotes the phase of the $\mathrm{U}(1)_Y$ symmetry. We further impose a discrete symmetry under the following transformation.

$$\Phi_1 \mapsto \Phi_2, \qquad \Phi_2 \mapsto \Phi_1, \qquad W^a_{0\mu} \mapsto W^a_{2\mu}, \qquad W^a_{2\mu} \mapsto W^a_{0\mu}, \tag{3.59}$$

where all the other fields remain unchanged. This transformation is equivalent to the exchange of $\mathrm{SU}(2)_0$ and $\mathrm{SU}(2)_2$, and thus this discrete symmetry requires $g_0 = g_2$.

The Lagrangian for the extended bosonic sector is shown below.

$$\begin{aligned} \mathcal{L} \supset & -\frac{1}{4} B_{\mu\nu} B^{\mu\nu} - \sum_{j=0}^{2} \sum_{a=1}^{3} \frac{1}{4} W^a_{j\mu\nu} W_j^{a\mu\nu} \\ & + D_\mu H^\dagger D^\mu H + \frac{1}{2} \mathrm{Tr} D_\mu \Phi_1^\dagger D_\mu \Phi_1 + \frac{1}{2} \mathrm{Tr} D_\mu \Phi_2^\dagger D_\mu \Phi_2 \\ & - V_{\text{scalar}}, \end{aligned} \tag{3.60}$$

where V_{scalar} is the scalar potential.

$$\begin{aligned} V_{\text{scalar}} = & m^2 H^\dagger H + m_\Phi^2 \left[\mathrm{Tr}\left(\Phi_1^\dagger \Phi_1\right) + \mathrm{Tr}\left(\Phi_2^\dagger \Phi_2\right) \right] \\ & + \lambda (H^\dagger H)^2 + \lambda_\Phi \left[\left(\mathrm{Tr}\left(\Phi_1^\dagger \Phi_1\right) \right)^2 + \left(\mathrm{Tr}\left(\Phi_2^\dagger \Phi_2\right) \right)^2 \right] \\ & + \lambda_{h\Phi} H^\dagger H \left[\mathrm{Tr}\left(\Phi_1^\dagger \Phi_1\right) + \mathrm{Tr}\left(\Phi_2^\dagger \Phi_2\right) \right] + \lambda_{12} \mathrm{Tr}\left(\Phi_1^\dagger \Phi_1\right) \mathrm{Tr}\left(\Phi_2^\dagger \Phi_2\right). \end{aligned} \tag{3.61}$$

We assume the following vacuum expectation values (VEVs) to realize the $\mathrm{U}(1)_{em}$ symmetry in the low energy.

$$\langle \Phi_1 \rangle = \langle \Phi_2 \rangle = \frac{1}{\sqrt{2}} \begin{pmatrix} v_\Phi & 0 \\ 0 & v_\Phi \end{pmatrix}, \qquad \langle H \rangle = \begin{pmatrix} 0 \\ \frac{v}{\sqrt{2}} \end{pmatrix}, \tag{3.62}$$

Table 2: The matter and Higgs fields and their gauge charges. The generation indices for the matter fields are implicit.

field	spin	$SU(3)_c$	$SU(2)_0$	$SU(2)_1$	$SU(2)_2$	$U(1)_Y$
q_L	$\frac{1}{2}$	3	1	2	1	$\frac{1}{6}$
u_R	$\frac{1}{2}$	3	1	1	1	$\frac{2}{3}$
d_R	$\frac{1}{2}$	3	1	1	1	$-\frac{1}{3}$
ℓ_L	$\frac{1}{2}$	1	1	2	1	$-\frac{1}{2}$
e_R	$\frac{1}{2}$	1	1	1	1	-1
H	0	1	1	2	1	$\frac{1}{2}$
Φ_1	0	1	2	2	1	0
Φ_2	0	1	1	2	2	0

where we assume the hierarchy between these VEVs, $v_\Phi \gg v$, throughout our analysis. We define component fields around the VEVs.

$$\Phi_j = \begin{pmatrix} \frac{v_\Phi+\sigma_j+i\pi_j^0}{\sqrt{2}} & i\pi_j^+ \\ i\pi_j^- & \frac{v_\Phi+\sigma_j-i\pi_j^0}{\sqrt{2}} \end{pmatrix}, \qquad H = \begin{pmatrix} i\pi_3^+ \\ \frac{v+\sigma_3-i\pi_3^0}{\sqrt{2}} \end{pmatrix}. \tag{3.63}$$

The diagonal and the same VEVs for both Φ_1 and Φ_2 are important to realize the desired low energy spectrum. Thanks to the diagonal structure, we still have the residual $SU(2)\times U(1)_Y$ gauge symmetry after Φ_1 and Φ_2 develop the nonzero VEVs. The corresponding gauge transformation is shown below.

$$\Phi_1 \mapsto U\Phi_1 U^\dagger, \qquad \Phi_2 \mapsto U\Phi_2 U^\dagger, \qquad H \mapsto e^{i\theta_Y} UH, \tag{3.64}$$

where U is a two-by-two matrix for the SU(2) gauge transformation. This SU(2) transformation corresponds to the $SU(2)_0\times$ $SU(2)_1\times$ $SU(2)_2$ transformation with $U_0 = U_1 = U_2 \equiv U$. This SU(2) is regarded as the $SU(2)_L$ in the SM and simply called the $SU(2)_L$ in the following discussion. The $SU(2)_L\times$ $U(1)_Y$ symmetry is broken by $\langle H\rangle$ to the $U(1)_{em}$ symmetry.

After all the Higgs fields develop nonzero VEVs, we still have the exchange symmetry since we assume the same VEVs for Φ_1 and Φ_2 fields. The discrete symmetry transformations after the symmetry breaking are shown below.

$$\sigma_1 \mapsto \sigma_2, \qquad \sigma_2 \mapsto \sigma_1, \qquad W_{0\mu}^a \mapsto W_{2\mu}^a, \qquad W_{2\mu}^a \mapsto W_{0\mu}^a. \tag{3.65}$$

We find out a Z_2 parity from this residual discrete symmetry by anti-symmetrizing the

exchanged fields.

$$h_D \equiv \frac{\sigma_1 - \sigma_2}{\sqrt{2}}, \tag{3.66}$$

$$V^0_\mu \equiv \frac{W^0_{0\mu} - W^0_{2\mu}}{\sqrt{2}}, \tag{3.67}$$

$$V^\pm_\mu \equiv \frac{W^\pm_{0\mu} - W^\pm_{2\mu}}{\sqrt{2}}, \tag{3.68}$$

where

$$W^\pm_{n\mu} = \frac{W^1_{n\mu} \mp i W^2_{n\mu}}{\sqrt{2}} \quad (n = 0, 2). \tag{3.69}$$

These fields are eigenstates of the $\mathrm{U}(1)_{em}$ charge.[3] These states acquire (-1) factors under the transformation in Eq. (3.65) and correspond to the odd fields. All the other states remain unchanged and correspond to the even fields. This is nothing but a Z_2 parity assignment for all the physical spectrum in our model. Note that the Z_2-odd states are automatically mass eigenstates since the mass mixing terms with other states are forbidden by Lorentz symmetry, $\mathrm{U}(1)_{em}$ symmetry, and Z_2 parity.

We refer to Z_2-odd spin-1 particles, V^0 and $V^\pm$, as *V-particles*. The V-particles are approximately regarded as the spin-1 triplet of $\mathrm{SU}(2)_L$ and have degenerated masses at the tree-level.

$$m^2_{V^0} = m^2_{V^\pm} = \frac{g_0^2 v_\Phi^2}{4} \equiv m^2_V. \tag{3.70}$$

The electroweak radiative corrections break this degeneracy, which makes the charged component slightly heavier than the neutral one. We find the following value for mass splitting at the one-loop level.

$$\delta m_V \equiv m_{V^\pm} - m_{V_0} \simeq 168 \text{ MeV}. \tag{3.71}$$

We want to focus on the spin-1 DM scenario to study the low energy phenomenology corresponding to the DM candidate from extra-dimensional setups and assume h_D is heavier than V^0. Consequently, V^0 is the lightest Z_2-odd particle and our stable spin-1 DM candidate.

3.3.1 Physical spectrum

The physical spectra can be read out by diagonalizing the mass matrices. We obtain the following mass eigenstates in the Higgs sector.

$$\begin{pmatrix} h_D \\ h \\ h' \end{pmatrix} = \begin{pmatrix} 1 & 0 & 0 \\ 0 & \sin\phi_h & \cos\phi_h \\ 0 & \cos\phi_h & -\sin\phi_h \end{pmatrix} \begin{pmatrix} \frac{1}{\sqrt{2}} & -\frac{1}{\sqrt{2}} & 0 \\ \frac{1}{\sqrt{2}} & \frac{1}{\sqrt{2}} & 0 \\ 0 & 0 & 1 \end{pmatrix} \begin{pmatrix} \sigma_1 \\ \sigma_2 \\ \sigma_3 \end{pmatrix}. \tag{3.72}$$

[3]The $\mathrm{U}(1)_{em}$ symmetry generator is expressed as $Q = T^3_0 + T^3_1 + T^3_2 + Y$ where T^3_n denote the third generators of $\mathrm{SU}(2)_n$ $(n = 0, 1, 2)$.

We take the scalar masses, $\{m_h, m_{h'}, m_{h_D}\}$, and the mixing angle, ϕ_h, as input parameters. The dimensionless couplings of $V_{\rm scalar}$ can be expressed in these input parameters.

$$\lambda = \frac{m_h^2 \cos^2\phi_h + m_{h'}^2 \sin^2\phi_h}{2v^2}, \tag{3.73}$$

$$\lambda_{h\Phi} = -\frac{\sin\phi_h \cos\phi_h}{2\sqrt{2}vv_\Phi}(m_{h'}^2 - m_h^2), \tag{3.74}$$

$$\lambda_\Phi = \frac{m_h^2 \sin^2\phi_h + m_{h'}^2 \cos^2\phi_h + m_{h_D}^2}{16v_\Phi^2}, \tag{3.75}$$

$$\lambda_{12} = \frac{m_h^2 \sin^2\phi_h + m_{h'}^2 \cos^2\phi_h - m_{h_D}^2}{8v_\Phi^2}. \tag{3.76}$$

For the charged gauge bosons, we obtain

$$\begin{pmatrix} V_\mu^\pm \\ W_\mu^\pm \\ W_\mu'^\pm \end{pmatrix} = \begin{pmatrix} 1 & 0 & 0 \\ 0 & \cos\phi_\pm & \sin\phi_\pm \\ 0 & -\sin\phi_\pm & \cos\phi_\pm \end{pmatrix} \begin{pmatrix} \frac{1}{\sqrt{2}} & 0 & -\frac{1}{\sqrt{2}} \\ 0 & 1 & 0 \\ \frac{1}{\sqrt{2}} & 0 & \frac{1}{\sqrt{2}} \end{pmatrix} \begin{pmatrix} W_{0\mu}^\pm \\ W_{1\mu}^\pm \\ W_{2\mu}^\mu \end{pmatrix}, \tag{3.77}$$

where

$$\cos\phi_\pm = \sqrt{\frac{m_{V^\pm}^2 - m_W^2}{m_{W'}^2 - m_W^2}}, \quad \sin\phi_\pm = \sqrt{\frac{m_{W'}^2 - m_{V^\pm}^2}{m_{W'}^2 - m_W^2}}. \tag{3.78}$$

The masses of charged Z_2-even vectors are obtained as

$$m_W^2 = \frac{1}{8}\left\{ g_1^2 v^2 + (g_0^2 + 2g_1^2)v_\Phi^2 - \sqrt{-4g_0^2 g_1^2 v^2 v_\Phi^2 + [g_1^2 v^2 + (g_0^2 + 2g_1^2)v_\Phi^2]^2} \right\}, \tag{3.79}$$

$$m_{W'}^2 = \frac{1}{8}\left\{ g_1^2 v^2 + (g_0^2 + 2g_1^2)v_\Phi^2 + \sqrt{-4g_0^2 g_1^2 v^2 v_\Phi^2 + [g_1^2 v^2 + (g_0^2 + 2g_1^2)v_\Phi^2]^2} \right\}. \tag{3.80}$$

For the neutral gauge bosons, we obtain

$$\begin{pmatrix} V_\mu^0 \\ A_\mu \\ Z_\mu \\ Z'_\mu \end{pmatrix} = \begin{pmatrix} \frac{1}{\sqrt{2}} & 0 & -\frac{1}{\sqrt{2}} & 0 \\ \frac{e}{g_0} & \frac{e}{g_1} & \frac{e}{g_0} & \frac{e}{g'} \\ \omega_Z^0 & \omega_Z^1 & \omega_Z^0 & \omega_Z^B \\ \omega_{Z'}^0 & \omega_{Z'}^1 & \omega_{Z'}^0 & \omega_{Z'}^B \end{pmatrix} \begin{pmatrix} W_{0\mu}^3 \\ W_{1\mu}^3 \\ W_{2\mu}^3 \\ B_\mu \end{pmatrix}, \tag{3.81}$$

where

$$e = \left(\frac{2}{g_0^2} + \frac{1}{g_1^2} + \frac{1}{g'^2}\right)^{-1/2}, \tag{3.82}$$

$$\omega_Z^0 = \frac{eg_1}{\sqrt{g_0^2 + 2g_1^2 g'}} \cos\phi_0 + \frac{g_0}{\sqrt{2(g_0^2 + 2g_1^2)}} \sin\phi_0, \tag{3.83}$$

$$\omega_Z^1 = \frac{eg_0}{\sqrt{g_0^2 + 2g_1^2 g'}} \cos\phi_0 - \frac{\sqrt{2}g_1}{\sqrt{g_0^2 + 2g_1^2}} \sin\phi_0, \tag{3.84}$$

$$\omega_Z^B = -\frac{e\sqrt{g_0^2 + 2g_1^2}}{g_0 g_1} \cos\phi_0, \tag{3.85}$$

$$\omega_{Z'}^0 = \frac{g_0}{\sqrt{2(g_0^2 + 2g_1^2)}} \cos\phi_0 - \frac{eg_1}{\sqrt{g_0^2 + 2g_1^2 g'}} \sin\phi_0, \tag{3.86}$$

$$\omega_{Z'}^1 = -\frac{\sqrt{2}g_1}{\sqrt{g_0^2 + 2g_1^2}} \cos\phi_0 - \frac{eg_0}{\sqrt{g_0^2 + 2g_1^2 g'}} \sin\phi_0, \tag{3.87}$$

$$\omega_{Z'}^B = \frac{e\sqrt{g_0^2 + 2g_1^2}}{g_0 g_1} \sin\phi_0. \tag{3.88}$$

We define ϕ_0 that satisfies the following relation.

$$\frac{1}{4}\begin{pmatrix} \frac{g_0^2 g_1^2 g'^2}{e^2(g_0^2+2g_1^2)} v^2 & -\frac{\sqrt{2}g_0 g_1^3 g'}{e(g_0^2+2g_1^2)} v^2 \\ -\frac{\sqrt{2}g_0 g_1^3 g'}{e(g_0^2+2g_1^2)} v^2 & \frac{(g_0^2+2g_1^2)^2 v_\Phi^2 + 2g_1^4 v^2}{(g_0^2+2g_1^2)} \end{pmatrix} \begin{pmatrix} \cos\phi_0 & -\sin\phi_0 \\ \sin\phi_0 & \cos\phi_0 \end{pmatrix} = \begin{pmatrix} \cos\phi_0 & -\sin\phi_0 \\ \sin\phi_0 & \cos\phi_0 \end{pmatrix} \begin{pmatrix} m_Z^2 & 0 \\ 0 & m_{Z'}^2 \end{pmatrix}. \tag{3.89}$$

3.3.2 Couplings of V-particles

We show the couplings of the V-particles in the limit of $v_\Phi \gg v$ to evaluate the V-particle annihilation processes. The vector triple couplings are shown below.

$$\mathcal{L} \supset i g_{X^+Y^-Z^0} \left[\left(X_\nu^+ \overleftrightarrow{\partial}^\mu Y^{-\nu} \right) Z_\mu^0 + \left(Y_\nu^- \overleftrightarrow{\partial}^\mu Z^{0\nu} \right) X_\mu^+ + \left(Z_\nu^0 \overleftrightarrow{\partial}^\mu X^{+\nu} \right) Y_\mu^- \right], \tag{3.90}$$

where

$$g_{W^+V^-V^0} = g_{V^+W^-V^0} \simeq g_W, \tag{3.91}$$

$$g_{W'^+V^-V^0} = g_{V^+W'^-V^0} = g_{V^+V^-Z'} \simeq \frac{g_W}{\sqrt{\frac{m_{Z'}^2}{m_V^2} - 1}} \equiv g_{Z'}, \tag{3.92}$$

$$g_{V^+V^-A} = e, \tag{3.93}$$

$$g_{V^+V^-Z} \simeq g_W c_W. \tag{3.94}$$

We define $s_W \equiv \sin\theta_W$ and $c_W \equiv \cos\theta_W$ where θ_W is the Weinberg angle. We also define $g_{Z'}$ in Eq. (3.92) to characterize the couplings between the V-particles and the Z_2-even vectors,

W' and Z'. We have two types of vector quartic couplings,

$$\begin{aligned}\mathcal{L} \supset & C^{cc}_{X^-Y^+Z^-W^+}\ X^+_\rho Y^-_\sigma Z^+_\mu W^-_\nu\ (2g^{\rho\mu}g^{\sigma\nu} - g^{\rho\nu}g^{\sigma\mu} - g^{\rho\sigma}g^{\mu\nu}) \\ & + C^{cn}_{X^-Y^+Z^0W^0}\ X^+_\rho Y^-_\sigma Z^0_\mu W^0_\nu\ (g^{\rho\mu}g^{\sigma\nu} + g^{\rho\nu}g^{\sigma\mu} - 2g^{\rho\sigma}g^{\mu\nu})\,,\end{aligned} \tag{3.95}$$

where

$$C^{cc}_{V^-V^+W^-W^+} = C^{cc}_{V^-V^+W^-W'^+} \simeq g_W^2, \tag{3.96}$$

$$C^{cn}_{W^-W^+V^0V^0} = C^{cn}_{W^-W'^+V^0V^0} \simeq \frac{1}{2}g_W^2, \tag{3.97}$$

$$C^{cn}_{V^-V^+ZZ} \simeq \frac{1}{2}g_W^2 c_W^2, \tag{3.98}$$

$$C_{V^+V^-AA} = \frac{e^2}{2}, \tag{3.99}$$

$$C_{V^+V^-AZ} \simeq e g_W c_W, \tag{3.100}$$

$$C_{V^+V^-AZ'} = e g_{Z'}, \tag{3.101}$$

$$C^{cn}_{V^-V^+ZZ'} \simeq g_W c_W g_{Z'}. \tag{3.102}$$

The V-particles have the Higgs coupling as well as above electroweak couplings. The triple couplings are expressed as

$$\mathcal{L} \supset \sum_{\phi=h,h'} g_\phi \phi \left(V^+_\mu V^{-\mu} + V^0_\mu V^{0\mu}\right), \tag{3.103}$$

The couplings are expressed as shown below.

$$g_h \simeq \left(\frac{2m_V^2}{v_\Phi}\right)\frac{\sin\phi_h}{\sqrt{2}}, \tag{3.104}$$

$$g_{h'} \simeq \left(\frac{2m_V^2}{v_\Phi}\right)\frac{\cos\phi_h}{\sqrt{2}}, \tag{3.105}$$

where ϕ_h is the mixing angle between Z_2-even Higgs bosons as introduced in Sec. 3.3.1. The quadratic couplings are given as

$$\mathcal{L} \supset (C_{hh}hh + 2C_{hh'}hh' + C_{h'h'}h'h')\left(V^+_\mu V^{-\mu} + \frac{1}{2}V^0_\mu V^{0\mu}\right), \tag{3.106}$$

where

$$C_{\phi_1\phi_2} \simeq g_{\phi_1} g_{\phi_2} \quad (\phi_1, \phi_2 = h, h'). \tag{3.107}$$

3.3.3 Parameters and Constraints

The parameters in the Lagrangian in Eq. (3.60) are summarized below.

$$\left\{g_0,\ g_1,\ g',\ m^2,\ m^2_\Phi,\ \lambda,\ \lambda_\Phi,\ \lambda_{h\Phi}, \lambda_{12}\right\}. \tag{3.108}$$

We choose the following input parameters for our phenomenological study.

$$\{e,\ m_Z,\ v,\ m_h,\ m_{Z'},\ m_V,\ m_{h'},\ m_{h_D}, \phi_h\}\,. \tag{3.109}$$

The first four parameters are already fixed by the experiments, while the last five parameters are free. Our spin-1 DM candidate has not only electroweak interactions but also Higgs interactions. Couplings between V-particles and Z_2-even Higgs are proportional to mixing angle factors shown in Eq. (3.104) and Eq. (3.105). The Higgs exchange channels are already probed by the latest direct detection experiment, and we obtain the following bound to evade the direct detection constraints [25].

$$\phi_h \lesssim 0.1. \tag{3.110}$$

Throughout our discussion, therefore, we take the small ϕ_h regime and the SM Higgs coupling with the V-particles are suppressed by the small mixing factor, $\sin\phi_h$. Although we do not specify the values of $m_{h'}$ and m_{h_D} in the following discussion, we assume these scalar masses are in the TeV scale to focus on the phenomenological aspects resulting from the electroweak interactions. The constraints on these parameters in the scalar sector are studied in Ref. [25]. For later convenience, we introduce g_W as defined below.

$$g_W \equiv \left(\frac{2}{g_0^2} + \frac{1}{g_1^2}\right)^{-1/2}. \tag{3.111}$$

This coupling corresponds to the $\mathrm{SU}(2)_L$ gauge coupling approximately, and we obtain $g_W \simeq 0.65$, which is the same value as the $\mathrm{SU}(2)_L$ gauge coupling in the SM, in the limit of $v_\Phi \gg v$.

We assume $v_\Phi \gg v$ throughout our study, and it is useful to derive the approximated forms for the physical values in this limit. For m_W and $m_{W'}$, we obtain

$$m_W \simeq \frac{g_W v}{2}, \tag{3.112}$$

$$m_{W'} \simeq m_{Z'}, \tag{3.113}$$

and thus we easily obtain the correct value of m_W. The gauge couplings, g_0 and g_1, are expressed as

$$g_0 \simeq \sqrt{2} g_W \frac{m_{Z'}}{m_V} \frac{1}{\sqrt{\frac{m_{Z'}^2}{m_V^2} - 1}}, \tag{3.114}$$

$$g_1 \simeq g_W \frac{m_{Z'}}{m_V}. \tag{3.115}$$

These couplings are constrained by the perturbative unitarity bounds. We obtain the following constraints in the high energy regime [28].

$$g_j < \sqrt{\frac{16\pi}{\sqrt{6}}} \simeq 4.53 \quad (j = 0, 1). \tag{3.116}$$

From these bounds, we can narrow down the viable range of the mass ratio, $\frac{m_{Z'}}{m_V}$. If we take $g_W \simeq 0.65$, we obtain

$$1.02 \lesssim \frac{m_{Z'}}{m_V} \lesssim 6.97. \tag{3.117}$$

More detailed explanations of our model are given in Ref. [25].

It is worth mentioning the relation between the spectrum of extra-dimensional models and our renormalized model. We immediately find the following mass ratio between m_V and $m_{Z'}$ from Eq. (3.114) and Eq. (3.115).

$$\frac{m_{Z'}}{m_V} \simeq \sqrt{1 + \frac{2g_1^2}{g_0^2}}. \tag{3.118}$$

Noting that the Z_2-odd V-particles (Z_2-even $m_{Z'}$) correspond to the first (second) KK mode in the extra-dimensional model. The relation of $m_V < m_{Z'}$ is trivially followed from this expression. Comparing with Eq. (3.55) and Eq. (3.118), the mass ratio between the first KK and the second KK modes are characterized by the boundary localized terms $\{r_{\rm IR}, r_{\rm UV}\}$ in the extra-dimensional and by the gauge couplings $\{g_0, g_1\}$ in our model, respectively. We may realize the general mass spectrum for the vector sector by taking arbitrary values of g_0 and g_1, which are independent parameters. Let us mention two limits of the coupling values. If we take $g_0 \ll g_1$, the mass splitting gets larger. This limit corresponds to the warped metric model where the IR modes are localized around $y = \pm L$, because a larger coupling indicates the lower cutoff scale of the theory. If we take $g_0 \gg g_1$, the mass splitting gets degenerated, which corresponds to the warped metric setup where the IR modes are localized around the symmetric point $y = 0$. The corresponding extra-dimensional models are studied in Ref. [19]. In Sec. 6.2, we will study the distinctive signatures predicted from the later degenerated region, $m_{Z'} \simeq m_V$.

4 Non-relativistic effective field theory for spin-1 DM

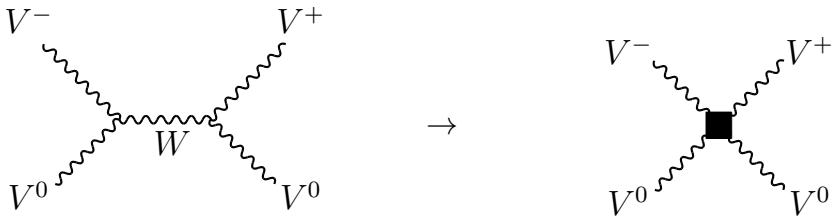

Figure 5: The philosophy of the effective field theory approach.

In the non-relativistic (NR) DM pair annihilation with the electroweak interactions, the electroweak potential gets effectively large, which is called the Sommerfeld effect. In this region, perturbative calculations of the annihilation cross section break down, and we have to use the distorted wave function profiles for a DM pair in order to include the potential force. The distortion is represented as a factor, which is called the Sommerfeld factor, in the final formula of DM annihilation cross section.

We take the effective field theoretical approach and perform the matching to determine the effective couplings so that the effective operators realize the non-relativistic amplitudes of the full theory. The philosophy of the effective field theory approach is shown in Fig. 5. In the full theory, we calculate the scattering amplitudes, which is evaluated in the appropriate regime. These results are described by the effective action. A effective coupling, which is denoted by the black box in the figure, is determined to realize the same amplitude of the full theory through the matching procedures. In particular, we take the non-relativistic limit and focus on the region where $m_{\rm DM} \gtrsim \mathcal{O}(1)$ TeV $\gg m_W$. In this limit, the electroweak forces mediated by W/Z boson and γ are imprinted in the potential between a pair of DM multiplets. The W, Z boson form the Yukawa potential while the photon form the Coulomb potential. Although the Yukawa potentials are exponentially suppressed for $r \gtrsim 1/m_{W/Z}$, the wave function of a heavy DM, which is typically localized $r \lesssim 1/m_{\rm DM}$, feels effectively long-range potential force. One of the most important features is that this potential force may mix the two-body states with the same quantum numbers. In particular, as shown in Fig. 5, the W boson exchanging process mixes V^0V^0 and V^-V^+. Therefore, the V^0V^0 state may annihilate into electrically neutral vectors such as photon and Z boson through this mixing via potential effects. This mixing effect plays a crucial role to search the DM annihilation signatures in the current universe.

These effects caused by the electroweak potential are crucial for our spin-1 DM because the DM mass should be $m_V \gtrsim \mathcal{O}(1)$ TeV to explain the correct DM relic abundance which is the same as other electroweak interacting DM with other spins. In this region, the W and Z bosons effectively form the long-range force potential for the V-particles. This implies we have the sizable Sommerfeld enhancement in the DM annihilation processes such as the evaluation of the thermal relic abundance and the predicted DM annihilation cross section

in the current universe. In particular, the monochromatic gamma-ray line from the DM annihilation is an excellent probe. This is our motivation to study the annihilation process of our spin-1 DM including the Sommerfeld effects.

In Sec. 4.1, we review how to construct the NR effective field theory in the quantum electrodynamics (QED). We also clarify the condition where viable Sommerfeld effects are expected in electroweakly interacting DM systems by taking the analogy of electrodynamics. In Sec. 4.2, we derive the effective action for electroweakly interacting spin-1 DM with triplet-like features and show the matching procedure to determine the effective coefficients from the full theory. The formulas of the DM annihilation cross section are derived including the electroweak potential force in Sec. 4.3. We will apply the derived formalism to the SM thermal relic evaluation in Sec. 5 and the DM annihilation signatures in Sec. 6, respectively.

4.1 Sommerfeld effect

The importance of the (effectively) long-range electroweak potential in DM pair annihilation is found by taking the analogy with the annihilation of positronium. We may derive the condition where the perturbative calculation breaks down and the Sommerfeld effects get viable in annihilation processes. To demonstrate the essential part to construct the effective theory, we will start from the review of the *non-relativistic quantum electrodynamics* (NRQED). The discussion in this abelian gauge theory is straightforwardly applied to electroweakly interacting DM systems. In Sec. 4.1.1, we review NRQED and estimate each operator in the power-counting regime of the velocity expansion. In Sec. 4.1.2, we derive the effective action of NRQED systematically following the power-counting laws of the relative velocity. In Sec. 4.1.3, we estimate the higher order corrections induced from the electromagnetic forces and find when these corrections get relevant. We also apply the discussions for annihilation processes of electroweakly interacting DM where we generalize the framework of electromagnetism to the electroweak theory.

4.1.1 Non-relativistic quantum electrodynamics

We first review NRQED, which is the effective field theory for the QED in the low energy regime. We follow Ref. [29] where *the non-relativistic quantum chromodynamics* (NRQCD) in the quarkonium system is studied to construct the NR effective theory with the presence of the gauge fields. The building blocks of NRQED are summarized below.

- NR fermion with a nonzero electrical charge (ψ)
- Electric field ($\boldsymbol{E}$)
- Magnetic field ($\boldsymbol{B}$)

Requiring the desired symmetry in the NR system, we may systematically construct operators using the above building blocks. The coefficient of each operator is determined to realize QED calculations in the NR limit according to the standard procedure to construct the effective field theory. All the processes in NRQED are estimated by the following variables:

- A fermion mass, M
- A relative velocity for two fermions, v

Since we are taking the NR regime, the relative velocity is treated as a perturbative parameter, $v \ll 1$, the higher order corrections of v get irrelevant.[4] Each building block of NRQED, and thus each operator, is characterized by a certain order of M and v, which is consistent with all the fundamental laws in the NR system. These laws provide a way to estimate the order of physical processes. We have to consider a complete set of operators that contains sufficiently higher order corrections of v to describe each physical process with the required accuracy.

The NR regime to construct NRQED is described in terms of the typical momentum of fermion fields, p, and its kinetic energy, K. These observables are characterized by using v and M.

$$p \sim Mv, \qquad\qquad K \sim Mv^2. \tag{4.1}$$

Orders of other operators are also determined by the field equations in the NR system.

Let us consider the fermion (ψ) and anti-fermion system (χ) such as the positronium system as a concrete application for NRQED. We will apply the same discussion to the electroweakly interacting DM system. focusing on DM pair annihilation processes. In the positronium-like system, the expectation value of the fermion number density operator is nearly one.

$$\int d^3x \psi^\dagger \psi \sim 1. \tag{4.2}$$

Noting that the fermions are localized within $\Delta x \sim 1/p$ by the uncertainty principle, we may read out the typical order of fermion field.

$$\psi \sim p^{\frac{3}{2}}. \tag{4.3}$$

The master equation for NR fermions is the Schrödinger equation.

$$\left(iD_t + \frac{\boldsymbol{D}^2}{2M} \right) \psi = 0, \tag{4.4}$$

where D_t and $\boldsymbol{D}$ denote covariant derivatives for time and spatial coordinates, respectively. The kinetic energy is the expectation value of the second term in the equation.

$$\int d^3x \psi^\dagger \frac{\boldsymbol{D}^2}{2M} \psi \sim K, \tag{4.5}$$

[4]Note that we also have $\alpha_{\rm em}$ as a perturbative parameter in QED calculation, which is the same order as v in NRQED power-counting rules. We will discuss in Sec. 4.1.3 that QED loop corrections appear as the power of $\alpha_{\rm em}/v$ and thus perturbative calculations break down if $\alpha_{\rm em} \lesssim v$.

and we obtain

$$\boldsymbol{D} \sim p \sim Mv. \tag{4.6}$$

From Eq. (4.4), we obtain

$$D_t \sim \frac{\boldsymbol{D}^2}{2M} \sim K. \tag{4.7}$$

The order counting for gauge fields can be read out from the Schrödinger equation with the existence of the gauge field. If we take the Coulomb gauge, which is the suitable gauge to describe the NR QED processes, the scalar potential, ϕ, is dominant compared with the vector potential, $\boldsymbol{A}$. The field equations in this gauge are expressed as shown below.

$$\nabla^2 e\phi = -e^2\psi^\dagger\psi + \cdots, \tag{4.8}$$

$$\left(\partial_t^2 - \nabla^2\right) e\boldsymbol{A} = \frac{e^2}{M}\psi^\dagger\nabla\psi + e^2\phi\nabla\phi + \cdots, \tag{4.9}$$

where ellipsis denotes the sub-leading terms in the NR expansion. The typical order of scalar potential is obtained as follows.

$$e\phi \sim \frac{e^2}{p^2}p^3 \sim e^2 p \sim K. \tag{4.10}$$

The last result is obtained by noting that the Schrödinger equation with the electromagnetic field is expressed as shown below.

$$\left(i\partial_t - e\phi + \frac{\nabla^2}{2M}\right) \sim 0. \tag{4.11}$$

Therefore, we may read out the order of gauge coupling, e. In particular, the QED fine structure constant, $\alpha_{\rm em}$ is estimated as shown below.

$$\alpha_{\rm em} \equiv \frac{e^2}{4\pi} \sim v. \tag{4.12}$$

Since the second term of LHS in Eq. (4.9) is relevant, we obtain the following estimation for $e\boldsymbol{A}$.

$$e\boldsymbol{A} \sim \frac{e^2}{p^2 M}p^4 \sim vK. \tag{4.13}$$

The orders of electromagnetic fields are derived below.

$$e\boldsymbol{E} = -\nabla e\phi + \cdots \sim M^2 v^3, \tag{4.14}$$

$$e\boldsymbol{B} = \nabla \times (e\boldsymbol{A}) + \cdots \sim M^2 v^4. \tag{4.15}$$

The above power-counting rule is summarized in Table 3, which corresponds to TABLE I in Ref. [29] for the NRQCD system.

Table 3: The power-counting rule for each operator in NRQED. The same table for the NRQCD, such as the quarkonium system, is summarized in TABLE I of Ref. [29].

Operator	Order of estimate	Description
ψ	$(Mv)^{3/2}$	Fermion field
χ	$(Mv)^{3/2}$	Anti-fermion field
D_t	Mv^2	Gauge covariant time derivative
$\boldsymbol{D}$	Mv	Gauge covariant spatial derivative
$e\phi$	Mv^2	Scalar potential
$e\boldsymbol{A}$	Mv^3	Vector potential
$e\boldsymbol{E}$	M^2v^3	Electric field
$e\boldsymbol{B}$	M^2v^4	Magnetic field

4.1.2 Effective interaction of NRQED

We derive effective interaction terms for NRQED. The time evolution of the NRQED system is described by the Schrödinger equation. described by the following leading order action.

$$S_0 = \int d^4x \psi^\dagger(x) \left(iD_t + \frac{\boldsymbol{D}^2}{2M} \right) \psi(x). \tag{4.16}$$

These interactions are the order of $\mathcal{O}(v^5)$ in the power-counting rules summarized in Table 3. We may write down all the possible interactions by requiring the following symmetry, which an original relativistic QED system respects in the NR limit.

- Gauge invariance
- Rotational invariance
- Charge conjugation invariance
- Parity invariance
- Unitarity

The relevant interaction terms are characterized by lower powers of v in the of NR expansion.

The bilinear form of fermions, which is suppressed by v^2 relative to the leading order interactions, are obtained as follows.

$$\begin{aligned}
\mathcal{L}_{\text{bilinear}} = & \frac{c_1}{M^3} \psi^\dagger \boldsymbol{D}^4 \psi \\
& + \frac{c_2}{M^2} \psi^\dagger \left[\boldsymbol{D} \cdot (e\boldsymbol{E}) - (e\boldsymbol{E}) \cdot \boldsymbol{D} \right] \psi \\
& + \frac{c_3}{M^2} \psi^\dagger \boldsymbol{\sigma} \cdot \left[\boldsymbol{D} \times (e\boldsymbol{E}) - (e\boldsymbol{E}) \times \boldsymbol{D} \right] \psi \\
& + \frac{c_4}{M} \psi^\dagger \boldsymbol{\sigma} \cdot (e\boldsymbol{B}) \, \psi,
\end{aligned} \tag{4.17}$$

where $\boldsymbol{\sigma}$ denotes the spin operator. We show the interaction terms focusing on the particle sector. We may derive the effective couplings for χ straightforwardly from the requirement of the charge conjugation invariance. The parity-odd intrinsic electric dipole moment interaction, $\psi^\dagger \boldsymbol{\sigma} \cdot (e\boldsymbol{E})\psi$, is not allowed because the parity invariance is required. The effective coefficients are denoted by c_i $(i = 1, 2, 3, 4)$ starting at the zeroth order of the relative velocity. The interaction relating to the higher order of time derivatives, such as $\psi^\dagger (iD_t)^2 \psi$, can be redefined as the first term of Eq. (4.17) using the zeroth order Schrödinger equation.

Besides, we also have contact interaction terms between fermion and anti-fermion.

$$\mathcal{L}_{\rm contact} = \frac{d_1}{M^2}\psi^\dagger\chi\ \chi^\dagger\psi + \frac{d_2}{M^2}\psi^\dagger\boldsymbol{\sigma}\chi\ \chi^\dagger\boldsymbol{\sigma}\psi. \tag{4.18}$$

These interactions have no counterpart in the relativistic theory and are induced at the loop level. This means that the effective coefficients, d_i $(i = 1, 2)$, are the order of $\mathcal{O}(\alpha_{\rm em}^2) \sim v^2$. These interaction terms, therefore, are suppressed by v^3 compared with the leading order terms. The annihilation and creation of (anti-)particles are described by these terms if the coefficients have the nonzero imaginary part. The nonzero imaginary part breaks down the unitarity requirement in the construction of effective field theory, but these effects are consistently induced from the QED loop effects. In particular, the imaginary part of the coefficient d_i is derived to realize the imaginary part of the amplitude calculated by QED in the NR limit. Since these terms are the leading order effects to describe the annihilation and creation of (anti-)particles, we have to include these higher order terms of $\mathcal{O}(v)$ to describe these phenomena. The imaginary part of the forward scattering amplitude is related to the cross section through the optical theorem. We will apply the same matching procedures in Sec. 4.2 for the NR system of electroweakly interacting spin-1 DM. Before moving to the spin-1 DM system, we show that the perturbative calculation will fail with the presence of the (effectively) long-range potential. This fact can be found by estimating the loop diagrams in the power-counting rule. We may straightforwardly generalize this fact to the electroweakly interacting DM system.

4.1.3 Threshold singularity of loop corrections

We review the threshold singularity, which appears in the positronium-like system in the NRQED framework. This singularity is related to a ladder diagram shown in Fig. 6. The left panel shows an electron-positron annihilation process into two photons. This diagram schematically shows the importance of the higher order corrections in the annihilation processes. We can estimate each QED corrections, which is depicted in red color in Fig. 6, by using the power-counting law and find the condition where the perturbative expansion of the cross section by $\alpha_{\rm em}$ brakes down. A fermion propagator corresponds to an inverse of the Schrödinger operator, $(i\partial_t - \frac{\boldsymbol{D}^2}{2M})^{-1}$, and thus we estimate each fermion propagator as $\sim 1/K$. A photon propagator corresponds to an inverse of the wave equation operator, $(\partial_t^2 - \nabla^2)^{-1}$. Since spatial derivatives are more relevant than time derivatives in the NRQED power-counting law, a photon propagator scales as $\sim 1/p^2$. Applying these scaling laws, we

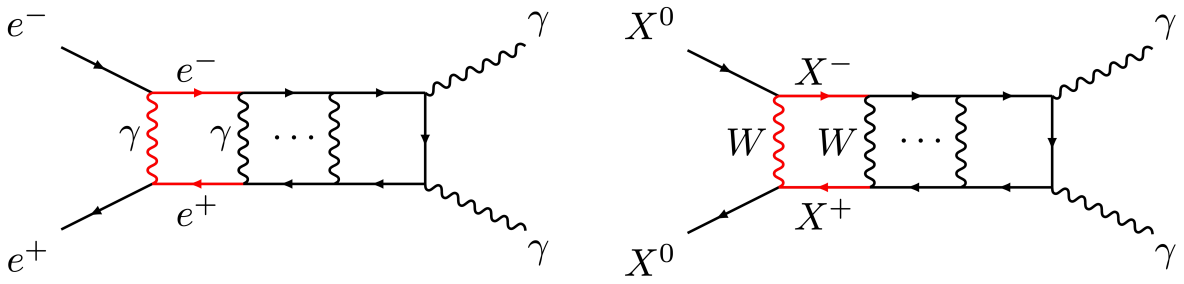

(a) $e^-e^+ \to 2\gamma$ (b) $X^-X^+ \to 2\gamma$

Figure 6: Ladder diagrams for annihilation processes into two photons. We show (a) electron-positron annihilation as an example of NRQED processes and (b) pair annihilation of an electroweakly interacting DM, respectively.

estimate the order of each QED loop correction as below.

$$\begin{aligned}(\text{QED loop}) &\simeq \int \frac{d\ell^0}{2\pi}\frac{d^3\ell}{(2\pi)^3}\cdot e^2\cdot(\text{NR fermion propagator})^2\cdot(\text{NR photon propagator})\\ &\simeq \alpha_{\rm em}\cdot K\cdot p^3\cdot\left(\frac{1}{K}\right)^2\cdot\frac{1}{p^2}\\ &\simeq \frac{\alpha_{\rm em}}{v}.\end{aligned} \tag{4.19}$$

This estimation immediately implies that higher order loop correction may be enhanced by a factor of $\alpha_{\rm em}/v$ in the NR limit, $v \lesssim \alpha_{\rm em}$. A ladder amplitude with n-th loop corrections scales as

$$i\mathcal{M} \sim \alpha_{\rm em}\cdot\left(\frac{\alpha_{\rm em}}{v}\right)^n. \tag{4.20}$$

Therefore, we obtain the following condition where the perturbative expansion of $\alpha_{\rm em}$ breaks down.

$$\alpha_{\rm em} \lesssim v, \tag{4.21}$$

which is known as a threshold singularity. In this region, we need to perform resummation of the ladder diagrams in Fig. 6.

In the system of an electroweakly interacting DM, we have a similar situation as that in NRQED system. The NR annihilation processes of the electroweakly interacting DM are important to investigate in various contexts. The annihilation of DM multiplets in the early universe is important to evaluate the thermal relic abundance. A DM pair annihilation in the current universe is necessary to probe DM signatures through astrophysical observation. Evaluating the annihilation cross sections in the NR limit is, therefore, relevant for DM physics. We may construct the NR effective theory for electroweakly interacting DM in the same procedures as those of NRQED. We may find a similar power-counting regime and

estimate the electroweak corrections. In particular, we have to know the order of the propagator for both NR DM and electroweak bosons to estimate the electroweak loop corrections shown in diagram (b) of Fig. 6. The momentum p of this annihilation process is estimated as $p = m_{DM}v \sim m_W$, and thus the relative velocity is $v \sim m_W/m_{DM}$. The kinetic energy K is, therefore, estimated as $K = m_{DM}v^2 \sim m_W^2/m_{DM}$. Note that an initial DM pair nearly satisfies the on-shell conditions, and the loop momentum for DM is typically a scale of DM mass, m_{DM}. Therefore, the propagator of DM scales as $\sim 1/m_{DM}$.[5] On the other hand, W boson in the loop has small momentum transfer and a propagator of W boson can be characterized as $\sim 1/m_W^2$. Using these estimations, we may derive the order of each electroweak loop correction in the same manner as that in QED.

$$\begin{aligned}(\text{Electroweak loop}) &\simeq \int \frac{d\ell^0}{2\pi}\frac{d^3\ell}{(2\pi)^3}\cdot 4\pi\alpha_2^2 \cdot (\text{propagator of DM})^2 \cdot (\text{propagator of } W \text{ boson}) \\ &\simeq \alpha_2 \cdot K \cdot p^3 \cdot \left(\frac{m_{DM}}{m_W}\right)^2 \cdot \frac{1}{m_W^2} \\ &\simeq \frac{\alpha_2 m_W}{m_{DM}}. \end{aligned} \tag{4.22}$$

This is the same estimation as that in the NRQED system with replacing v to m_W/m_{DM}, and we obtain the condition where perturbative calculations broke down in the electroweakly interacting DM system.

$$\frac{\alpha_2}{m_W} \lesssim \frac{1}{m_{DM}}. \tag{4.23}$$

This condition tells us a physical intuition why the perturbative calculations no longer work: The LHS of Eq. (4.23) expresses the typical range for the Yukawa force induced by W boson while the RHS expresses the typical range where DM wave functions are localized. Therefore, the condition of Eq. (4.23) can be restated as the condition where DM wave function is localized within the range of electroweak potential. If this condition is satisfied, a wave function for DM is distorted from plane wave profiles due to the significant potential force. This effect is called the Sommerfeld effect. To derive the annihilation cross section including this effect, we have to use the distorted plane wave profile. In the final formula, this distortion of the wave function is expressed as the Sommerfeld factor. We will review, in Sec. 4.2, the derivation of annihilation cross section including the Sommerfeld effects by constructing the NR effective theory of electroweakly interacting DM system.

4.2 Formalism

We show the effective action of the NR effective theory for spin-1 DM. The building block of effective action is two-body states that are composed of elementary particles. In Sec. 4.2.1, we will introduce the general framework for NR electroweakly interacting spin-1 theory and

[5] Interactions between spin-1 DM and electroweak bosons are derivative couplings where a derivative also scales as $\sim m_{DM}$, and thus the scaling is the same as the spin-1/2 DM case.

show the effective action in terms of two-body states. We decompose two-body states into each partial wave mode for the later convenience to solve the Schrödinger equations. In Sec. 4.2.2, we show the potential for $\mathrm{SU}(2)_L$ triplet spin-1 theory with $Y = 0$. In Sec. 4.2.3, we give the potential for the spin-1/2 system with the same electroweak charge and compare results with those in the spin-1 system.

4.2.1 Derivation of effective action

The DM annihilation processes including the Sommerfeld effects are studied in many contexts of the spin-1/2 DM system with electroweak interactions [14, 7]. The method to derive the effective action is systematically summarized in Ref. [30, 31] We use the same method to derive the effective theory for the spin-1 DM system with electroweak couplings. In particular, we will focus on the $\mathrm{SU}(2)_L$ triplet and $Y = 0$ spin-1 DM throughout this thesis, which corresponds to the electroweakly charged KK DM in the extra-dimensional scenario. The formalism is straightforwardly applicable to spin-1 DM system with more general interactions.

The asymptotic field operators of V-particles are expressed below.

$$V_\mu^0(x) = \sum_{A=1}^{3} \int \frac{d^3p}{(2\pi)^3} \frac{1}{\sqrt{2E_\mathrm{p}}} \left[a^A(\boldsymbol{p}) e^{-ip\cdot x} \epsilon_\mu^A(p) + a^{A\dagger}(\boldsymbol{p}) e^{ip\cdot x} \epsilon_\mu^{A*}(p) \right], \tag{4.24}$$

$$V_\mu^-(x) = \sum_{A=1}^{3} \int \frac{d^3p}{(2\pi)^3} \frac{1}{\sqrt{2E_\mathrm{p}}} \left[b^A(\boldsymbol{p}) e^{-ip\cdot x} \epsilon_\mu^A(p) + d^{A\dagger}(\boldsymbol{p}) e^{ip\cdot x} \epsilon_\mu^{A*}(p) \right], \tag{4.25}$$

$$V_\mu^+(x) = \sum_{A=1}^{3} \int \frac{d^3p}{(2\pi)^3} \frac{1}{\sqrt{2E_\mathrm{p}}} \left[d^A(\boldsymbol{p}) e^{-ip\cdot x} \epsilon_\mu^A(p) + b^{A\dagger}(\boldsymbol{p}) e^{ip\cdot x} \epsilon_\mu^{A*}(p) \right]. \tag{4.26}$$

We introduce the physical polarization vectors, $\epsilon_\mu^A(p)$ $(A = 1, 2, 3)$, which satisfy the following transverse condition,

$$p^\mu \epsilon_\mu^A(p) = 0, \tag{4.27}$$

and the orthogonal relation.

$$\epsilon_\mu^{A*}(p) \epsilon^{B\mu}(p) = -\delta^{AB}. \tag{4.28}$$

The annihilation and creation operators satisfy the canonical commutation relations.

$$[a^A(\boldsymbol{p}), a^{B\dagger}(\boldsymbol{p}')] = (2\pi)^3 \delta^3(\boldsymbol{p} - \boldsymbol{p}') \delta^{AB}, \tag{4.29}$$

$$[b^A(\boldsymbol{p}), b^{B\dagger}(\boldsymbol{p}')] = (2\pi)^3 \delta^3(\boldsymbol{p} - \boldsymbol{p}') \delta^{AB}, \tag{4.30}$$

$$[d^A(\boldsymbol{p}), d^{B\dagger}(\boldsymbol{p}')] = (2\pi)^3 \delta^3(\boldsymbol{p} - \boldsymbol{p}') \delta^{AB}. \tag{4.31}$$

The NR two-body effective action for V-particles are derived by performing the NR expansion for these operators and integrating out the large momentum modes. Since the zeroth

component of the polarization tensor is sub-leading in the NR limit, we leave the spatial components ($i = 1, 2, 3$) for the V-particle operators.

$$V_i^0(x) \simeq \frac{1}{\sqrt{2m_V}} \left[e^{-im_V t} \mathcal{A}_i(x) + e^{im_V t} \mathcal{A}_i^\dagger(x) \right], \tag{4.32}$$

$$V_i^-(x) \simeq \frac{1}{\sqrt{2m_V}} \left[e^{-im_V t} \mathcal{B}_i(x) + e^{im_V t} \mathcal{D}_i^\dagger(x) \right], \tag{4.33}$$

$$V_i^+(x) \simeq \frac{1}{\sqrt{2m_V}} \left[e^{-im_V t} \mathcal{D}_i(x) + e^{im_V t} \mathcal{B}_i^\dagger(x) \right], \tag{4.34}$$

where we define

$$\mathcal{A}_i(x) = \sum_{A=1}^{3} \int \frac{d^3p}{(2\pi)^3} a^A(\boldsymbol{p}) e^{-ip\cdot x} \epsilon_i^A(p), \tag{4.35}$$

$$\mathcal{B}_i(x) = \sum_{A=1}^{3} \int \frac{d^3p}{(2\pi)^3} b^A(\boldsymbol{p}) e^{-ip\cdot x} \epsilon_i^A(p), \tag{4.36}$$

$$\mathcal{D}_i(x) = \sum_{A=1}^{3} \int \frac{d^3p}{(2\pi)^3} d^A(\boldsymbol{p}) e^{-ip\cdot x} \epsilon_i^A(p). \tag{4.37}$$

We also express one particle states for NR V-particles with momentum $\boldsymbol{p}$ and polarization A.

$$\left| V^0; \boldsymbol{p}, A \right\rangle \simeq \sqrt{2m_V} a^{A\dagger}(\boldsymbol{p}) \left| 0 \right\rangle, \tag{4.38}$$

$$\left| V^-; \boldsymbol{p}, A \right\rangle \simeq \sqrt{2m_V} b^{A\dagger}(\boldsymbol{p}) \left| 0 \right\rangle, \tag{4.39}$$

$$\left| V^+; \boldsymbol{p}, A \right\rangle \simeq \sqrt{2m_V} d^{A\dagger}(\boldsymbol{p}) \left| 0 \right\rangle. \tag{4.40}$$

The effective action is expressed in the two-body states composed of the NR V-particle operators. If we focus on the leading-order effects in the NR limit, the orbital momentum and spin angular momentum are conserved independently. This is because the potential at the NR leading-order has a spherically symmetric form. Consequently, the total spin angular momentum, J, and z-component of the spin angular momentum, J_z, are good quantum numbers. The electric charge is also conserved in each process. Therefore, the effective action is decomposed into each partial wave mode and diagonalized in the electric charge.

It is convenient to change the space-time coordinates into the center of mass coordinate, $R = (R^0, \boldsymbol{R})$, and the relative coordinate, $\boldsymbol{r}$.

$$R^0 = t, \qquad \boldsymbol{R} \equiv \frac{\boldsymbol{x} + \boldsymbol{y}}{2}, \qquad \boldsymbol{r} \equiv \boldsymbol{x} - \boldsymbol{y}, \tag{4.41}$$

where $\boldsymbol{x}$ and $\boldsymbol{y}$ denote spatial coordinates of two elementary particles. The effective action

is obtained in the decomposed form into each partial wave state.

$$S_{\rm eff} = \sum_{J,J_z}\Bigg\{\int d^4Rd^3r\ \Phi_{Q=0}^{J,J_z\dagger}\cdot\left[\left(i\partial_{R^0}+\frac{\nabla_R^2}{4m_V}+\frac{\nabla_r^2}{m_V}\right)-\hat{V}_{Q=0}(r)+i\frac{9}{2}\hat{\Gamma}^J_{Q=0}\delta^3(\boldsymbol{r})\right]\cdot\Phi_{Q=0}^{J,J_z}$$
$$+\sum_{Q=\pm1,\pm2}\int d^4Rd^3r\ \phi_Q^{J,J_z\dagger}\left[\left(i\partial_{R^0}+\frac{\nabla_R^2}{4m_V}+\frac{\nabla_r^2}{m_V}\right)-V_Q(r)+i\frac{9}{2}\Gamma^J_Q\delta^3(\boldsymbol{r})\right]\phi_Q^{J,J_z}\Bigg\}, \tag{4.42}$$

where $r\equiv|\boldsymbol{r}|$ and $J=0,1,2$ with $|J_z|\le J$. For electrically neutral two-body states, we have two states composed of V^-V^+ or V^0V^0, and thus the potential for $Q=0$ two-body states is a two-by-two matrix form. We will show the explicit form for V and Γ in Sec. 4.2.2. We introduce the $Q=0$ two-body fields as defined below.

$$\Phi_{Q=0}^{J,J_z}(R,\boldsymbol{r})=\begin{pmatrix}\phi_C^{J,J_z}(R,\boldsymbol{r})\\ \phi_N^{J,J_z}(R,\boldsymbol{r})\end{pmatrix}. \tag{4.43}$$

Each component is defined as

$$\phi_C^{J,J_z}(R,\boldsymbol{r})=\mathcal{B}_i(R^0,\boldsymbol{R}+\boldsymbol{r}/2)\ S_{ij}^{J,J_z}\ \mathcal{D}_j(R^0,\boldsymbol{R}-\boldsymbol{r}/2)\qquad(J=0,1,2), \tag{4.44}$$
$$\phi_N^{J,J_z}(R,\boldsymbol{r})=\frac{1}{\sqrt{2}}\mathcal{A}_i(R^0,\boldsymbol{R}+\boldsymbol{r}/2)\ S_{ij}^{J,J_z}\ \mathcal{A}_j(R^0,\boldsymbol{R}-\boldsymbol{r}/2)\qquad(J=0,2), \tag{4.45}$$

where the upper and lower components correspond to V^-V^+ and V^0V^0, respectively. For electrically charged states, we define

$$\phi_{Q=-1}^{J,J_z}(R,\boldsymbol{r})=\mathcal{B}_i(R^0,\boldsymbol{R}+\boldsymbol{r}/2)\ S_{ij}^{J,J_z}\ \mathcal{A}_j(R^0,\boldsymbol{R}-\boldsymbol{r}/2)\qquad(J=0,1,2), \tag{4.46}$$
$$\phi_{Q=1}^{J,J_z}(R,\boldsymbol{r})=\mathcal{D}_i(R^0,\boldsymbol{R}+\boldsymbol{r}/2)\ S_{ij}^{J,J_z}\ \mathcal{A}_j(R^0,\boldsymbol{R}-\boldsymbol{r}/2)\qquad(J=0,1,2), \tag{4.47}$$

$$\phi_{Q=-2}^{J,J_z}(R,\boldsymbol{r})=\frac{1}{\sqrt{2}}\mathcal{B}_i(R^0,\boldsymbol{R}+\boldsymbol{r}/2)\ S_{ij}^{J,J_z}\ \mathcal{B}_j(R^0,\boldsymbol{R}-\boldsymbol{r}/2)\qquad(J=0,2), \tag{4.48}$$
$$\phi_{Q=2}^{J,J_z}(R,\boldsymbol{r})=\frac{1}{\sqrt{2}}\mathcal{D}_i(R^0,\boldsymbol{R}+\boldsymbol{r}/2)\ S_{ij}^{J,J_z}\ \mathcal{D}_j(R^0,\boldsymbol{R}-\boldsymbol{r}/2)\qquad(J=0,2). \tag{4.49}$$

In the above definition, we introduce the basis of three-by-three matrices.

$$\hat{S}^{J,J_z}\equiv S_{ij}^{J,J_z}\qquad(i,j=1,2,3), \tag{4.50}$$

where

$$\hat{S}^{0,0} = \frac{-1}{\sqrt{3}} \begin{pmatrix} 1 & 0 & 0 \\ 0 & 1 & 0 \\ 0 & 0 & 1 \end{pmatrix}, \tag{4.51}$$

$$\hat{S}^{1,1} = \frac{1}{2} \begin{pmatrix} 0 & 0 & -1 \\ 0 & 0 & -i \\ 1 & i & 0 \end{pmatrix}, \quad \hat{S}^{1,0} = \frac{1}{\sqrt{2}} \begin{pmatrix} 0 & i & 0 \\ -i & 0 & 0 \\ 0 & 0 & 0 \end{pmatrix}, \quad \hat{S}^{1,-1} = \frac{1}{2} \begin{pmatrix} 0 & 0 & -1 \\ 0 & 0 & i \\ 1 & -i & 0 \end{pmatrix}, \tag{4.52}$$

$$\hat{S}^{2,2} = \frac{1}{2} \begin{pmatrix} 1 & i & 0 \\ i & -1 & 0 \\ 0 & 0 & 0 \end{pmatrix}, \quad \hat{S}^{2,1} = \frac{1}{2} \begin{pmatrix} 0 & 0 & -1 \\ 0 & 0 & -i \\ -1 & -i & 0 \end{pmatrix}, \quad \hat{S}^{2,0} = \frac{1}{\sqrt{6}} \begin{pmatrix} -1 & 0 & 0 \\ 0 & -1 & 0 \\ 0 & 0 & 2 \end{pmatrix},$$
$$\hat{S}^{2,-1} = \frac{1}{2} \begin{pmatrix} 0 & 0 & 1 \\ 0 & 0 & -i \\ 1 & -i & 0 \end{pmatrix}, \quad \hat{S}^{2,-2} = \frac{1}{2} \begin{pmatrix} 1 & -i & 0 \\ -i & -1 & 0 \\ 0 & 0 & 0 \end{pmatrix}. \tag{4.53}$$

These matrices satisfy the following orthogonal relation.

$$\mathrm{Tr}\left[\hat{S}^{J,J_z}\hat{S}^{J',J'_z *}\right] = (-1)^J \delta^{JJ'}\delta^{J_z J'_z}, \tag{4.54}$$

These matrices play a role to decompose two elementary operators into irreducible decomposed two-body operators. Note that $\hat{S}^{J,J_z}$ is symmetric matrices for $J = 0, 2$ while anti-symmetric for $J = 1$. We have no ϕ_N^{1,J_z} and $\phi_{Q=\pm 2}^{1,J_z}$ because these states are composed of two identical particles. The spin-angular momentum J is conserved as long as we focus on the NR leading order contributions. Therefore, in our leading order calculations, the $J = 1$ contributions only arise in the annihilation of V^-V^+ and $V^0V^\mp$. For the thermal relic evaluation, the electrically charged components also contribute to change DM number density before decoupling from the thermal bath. On the other hand, the initial state of DM is fixed to be V^0V^0 to study DM annihilation signatures in the current universe because the charged components $V^\mp$ have already decoupled. The normalization factors in Eqs. (4.44)-(4.49) are fixed to realize the canonical weights for the two-body propagators. The two-body propagator of ϕ_C^{J,J_z} is defined as the time-ordered product.

$$\left\langle 0 \left| T\phi_C^{J,J_z}(R,\boldsymbol{r})\phi_C^{J,J_z\dagger}(0,\boldsymbol{0}) \right| 0 \right\rangle = \int \frac{d^3P}{(2\pi)^3}\frac{d^3k}{(2\pi)^3}\, e^{-i\left(\frac{|\boldsymbol{P}|^2}{4m}+\frac{\boldsymbol{k}^2}{m}\right)R^0 + i\boldsymbol{P}\cdot\boldsymbol{R}}\, e^{+i\boldsymbol{k}\cdot\boldsymbol{r}}\, \theta(R^0), \tag{4.55}$$

where $\theta(R^0)$ is the Heaviside step function. This expression is obtained by substituting the explicit forms of ϕ_C^{J,J_z} and $\phi_C^{J,J_z\dagger}$ and using the canonical commutation relation between them.[6] The definition of ϕ_N^{J,J_z} and $\phi_{Q=\pm 2}^{J,J_z}$ has another normalization factor of $1/\sqrt{2}$ because these two-body states are composed of two identical particles.

[6]Note that $(\hat{S}^{J,J_z})^\dagger = (-1)^J(\hat{S}^{J,J_z})^*$ because it is symmetric for $J = 0, 2$ but anti-symmetric for $J = 1$.

4.2.2 Two-body potential for the non-abelian vector DM system

The leading-order expressions for the real part of the potential, V, are shown below.

$$\hat{V}_{Q=0}(r) = \begin{pmatrix} 2\delta m_V - \dfrac{\alpha_2 s_W^2}{r} - \dfrac{\alpha_2 c_W^2 e^{-m_Z r}}{r} & -\dfrac{\sqrt{2}\alpha_2 e^{-m_W r}}{r} \\ -\dfrac{\sqrt{2}\alpha_2 e^{-m_W r}}{r} & 0 \end{pmatrix}, \tag{4.56}$$

$$V_{Q=\pm 1}(r) = \frac{\alpha_2 e^{-m_W r}}{r}, \tag{4.57}$$

$$V_{Q=\pm 2}(r) = \frac{\alpha_2 s_W^2 + \alpha_2 c_W^2 e^{-m_Z r}}{r}, \tag{4.58}$$

where $\alpha_2 \equiv g_W^2/4\pi$ corresponds to the $\mathrm{SU}(2)_L$ fine structure constant in non-abelian vector DM model. These potentials are read out from the NR scattering amplitudes of V-particles. The derivation is shown in Appendix A.1. As mentioned above, the potential for $Q = 0$ two-body states has a two-by-two matrix form. The off-diagonal elements induced by the W boson exchanging processes mix the ϕ_C and ϕ_N states, which realizes a sizable DM annihilation cross section into neutral vector bosons such as a photon and Z boson. In the above expressions, we focus on the potential induced by electroweak bosons. Compared with these contributions, the other channels are sub-leading due to the following reasons: The Higgs exchange contributions are suppressed by small ϕ_h. The W' and Z' exchange contributions are exponentially suppressed by $m_{W'}$ and $m_{Z'}$. The contributions from the vector quadratic couplings are suppressed by $1/m_V^2$.

The imaginary part of the potential, $\hat{\Gamma}^J$, is derived by operator matching between the two-body operators and the calculations of the loop amplitudes of the V-particles. We may derive Γ from the perturbative annihilation cross section of V-particles relating the forward scattering amplitude and the annihilation cross section through the optical theorem.[7] The detailed derivation is given in Appendix A.2. As discussed in Sec. 4.1.3, a perturbative expansion by α_2 breaks down for the TeV scale DM scenario. The cross section formula including the Sommerfeld effects is derived in Sec. 4.3.[8]

For the thermal relic evaluation discussed in Sec. 5, we need to treat all the annihilation modes of V-particles including longitudinal contributions of the final massive vectors. We will postpone to giving master formulas to express all the leading order perturbative annihilation cross section until Sec. 5.2.2 where the same matching procedures are applied to derive Γ. Here we give rather simpler results focusing on the line gamma-ray studies, which is more useful for the comparison with the results in the spin-1/2 system. The annihilation channels into more than one primary photon, γX, contribute to the narrow spectral line where X denotes neutral particles that may appear in the final state. This monochromatic channel

[7] We choose the factor of 9/2 in Eq. (4.42) so that the (1,1)-component of $\hat{\Gamma}^J$ is equal to the tree-level spin-averaged velocity-weighted annihilation cross sections of $V^- V^+$ with J. For spin-1/2 DM system, we have to replace $9/2 \to 2$ to hold the same cross section formulas.

[8] See Eq. (4.95).

is easy to separate with the astrophysical background and is expected to be a smoking-gun signal from DM annihilation. In particular, we focus on $X = \gamma, Z, Z'$ and derive Γ induced from these channels. We have to calculate the one-loop forward scattering amplitudes with $XX' = \gamma\gamma, Z\gamma, Z'\gamma$ for the intermediate states to derive the corresponding $\hat{\Gamma}^J$. The annihilation modes into $h\gamma$ and $h'\gamma$ induce $J = 1$ partial wave contributions only, which is irrelevant to DM annihilation in the current universe.[9] Noting that a photon has only the transverse modes, all the longitudinal contributions vanish. Therefore, we may safely take the massless limit of the SM particles in the final states. We decompose $\hat{\Gamma}^J$ into each contribution of the intermediate state, XX', as denoted by $\Gamma^J_{XX'}$. The leading order results are shown below where we omit the SM masses for the final states.

$$\hat{\Gamma}^{J=0}_{\gamma\gamma} = \frac{2}{3}\frac{\pi\alpha_2^2}{m_V^2}\begin{pmatrix} s_W^4 & 0 \\ 0 & 0 \end{pmatrix}, \tag{4.59}$$

$$\hat{\Gamma}^{J=2}_{\gamma\gamma} = \frac{32}{45}\frac{\pi\alpha_2^2}{m_V^2}\begin{pmatrix} s_W^4 & 0 \\ 0 & 0 \end{pmatrix}, \tag{4.60}$$

$$\hat{\Gamma}^{J=0}_{Z\gamma} = \frac{2}{3}\frac{\pi\alpha_2^2}{m_V^2}\begin{pmatrix} 2c_W^2 s_W^2 & 0 \\ 0 & 0 \end{pmatrix}, \tag{4.61}$$

$$\hat{\Gamma}^{J=2}_{Z\gamma} = \frac{32}{45}\frac{\pi\alpha_2^2}{m_V^2}\begin{pmatrix} 2c_W^2 s_W^2 & 0 \\ 0 & 0 \end{pmatrix}, \tag{4.62}$$

$$\hat{\Gamma}^{J=0}_{Z'\gamma} = \frac{1}{27}\frac{\alpha_2 g_{Z'}^2}{m_V^2}(1-r_{Z'})(3-2r_{Z'})^2\begin{pmatrix} s_W^2 & 0 \\ 0 & 0 \end{pmatrix}, \tag{4.63}$$

$$\hat{\Gamma}^{J=2}_{Z'\gamma} = \frac{8}{135}\frac{\alpha_2 g_{Z'}^2}{m_V^2}(1-r_{Z'})(6+3r_{Z'}+r_{Z'}^2)\begin{pmatrix} s_W^2 & 0 \\ 0 & 0 \end{pmatrix}, \tag{4.64}$$

where $r_{Z'} \equiv m_{Z'}^2/4m_V^2$, and $g_{Z'}$ is defined in Eq. (3.92).

4.2.3 Two-body potential for Wino DM system

To compare with the spin-1 DM system, we show the result of two-body potential in the Wino DM system, which the leading order result is derived in Ref. [32] including $Q \neq 0$ two-body states.

$$\hat{V}_{Q=0}(r) = \begin{pmatrix} 2\delta m_V - \dfrac{\alpha_2 s_W^2}{r} - \dfrac{\alpha_2 c_W^2 e^{-m_Z r}}{r} & -\dfrac{\sqrt{2}\alpha_2 e^{-m_W r}}{r} \\ -\dfrac{\sqrt{2}\alpha_2 e^{-m_W r}}{r} & 0 \end{pmatrix}, \tag{4.65}$$

$$V_{Q=\pm1}(r) = -\frac{\alpha_2 e^{-m_W r}}{r}, \tag{4.66}$$

$$V_{Q=\pm2}(r) = \frac{\alpha_2 s_W^2 + \alpha_2 c_W^2 e^{-m_Z r}}{r}. \tag{4.67}$$

[9] These channels contribute to thermal relic evaluation where electrically charged components are also relevant. We will show the formulas of V-particle annihilation cross section into scalar and vector particles in Eqs. (5.9)-(5.11).

The leading-order results is the same as that of the $\mathrm{SU}(2)_L$ triplet spin-1/2 DM except for the potential for $Q = \pm 1$ two-body states where overall signs are opposite. In particular, the potential is repulsive for spin-1 DM while attractive for spin-1/2 DM. The imaginary part of the potential is shown below.

$$\hat{\Gamma}^{Q=0}_{J=0} = \frac{\pi\alpha_2^2}{2m^2}\begin{pmatrix} 3 & \sqrt{2} \\ \sqrt{2} & 2 \end{pmatrix}, \tag{4.68}$$

$$\Gamma^{J=1}_{Q=0} = \frac{25}{24}\frac{\pi\alpha_2^2}{m^2}, \tag{4.69}$$

$$\Gamma^{J=0}_{Q=\pm 1} = \frac{1}{2}\frac{\pi\alpha_2^2}{m^2}, \tag{4.70}$$

$$\Gamma^{J=1}_{Q=\pm 1} = \frac{25}{24}\frac{\pi\alpha_2^2}{m^2}, \tag{4.71}$$

$$\Gamma^{J=0}_{Q=\pm 2} = \frac{1}{2}\frac{\pi\alpha_2^2}{m^2}, \tag{4.72}$$

where we sum over all the final states with neglecting masses of the SM particles. The partial contributions from $\gamma\gamma$ and $Z\gamma$ channels are shown below.

$$\hat{\Gamma}^{J=0}_{\gamma\gamma} = \frac{\pi\alpha_2^2}{m^2}\begin{pmatrix} s_W^4 & 0 \\ 0 & 0 \end{pmatrix}, \tag{4.73}$$

$$\hat{\Gamma}^{J=0}_{Z\gamma} = \frac{\pi\alpha_2^2}{m^2}\begin{pmatrix} c_W^2 s_W^2 & 0 \\ 0 & 0 \end{pmatrix}. \tag{4.74}$$

In the spin-1/2 DM system, we have two variations in two-body states with $(Q, J) = (0, 0)$, $\phi_C \simeq \chi^-\chi^+$ and $\phi_N \simeq \chi^0\chi^0$. Therefore, the potential has a two-by-two matrix form. This is the same situation as the case of the spin-1 system. The diagonal component of Γ corresponds to the velocity-weighted spin-averaged annihilation cross section in our matching procedure. In particular, Γ_{11} corresponds to the tree-level total annihilation cross section of $\chi^-\chi^+$ while $\Gamma_{22}/2$ corresponds to that of $\chi^0\chi^0$.[10]

Let us mention the electroweak higher order corrections in our analysis. For the spin-1/2 DM, the Sudakov log corrections [33, 34, 35, 36, 37] and the one-loop correction for the real part of the potential [38] are precisely evaluated in the context of the Wino DM study. In our spin-1 DM system, those potentially large corrections have not been evaluated yet, and thus our predictions have the uncertainty of $\mathcal{O}(1)$ factors. We focus on the leading-order results in both DM systems to show the comparison. Although the electroweak corrections also induce spin-dependence in signatures, these effects are sub-leading compared to the leading order results.

Before we show the procedure to evaluate DM annihilation processes including these potential effects, we remark the differences in effective action between spin-1 DM and spin-1/2 DM system focusing on the line gamma-ray channels. First, the Sommerfeld enhancement factor is approximately the same in both systems since we have the same $\hat{V}$ and the mass

[10] Factor of 1/2 comes from the fact that the $\chi^0\chi^0$ state is composed of identical particles.

splitting at the leading-order. Consequently, we have the same resonance structures as those in the Wino system. Second, if we compare the annihilation cross section into $\gamma\gamma$ and $Z\gamma$, a cross section value of spin-1 DM are larger than that of spin-1/2 DM by $38/9 \simeq 4.22\cdots$.[11] This is because spin-1 DM forms both $J = 0$ and $J = 2$ partial wave states while spin-1/2 DM forms only the $J = 0$ state. Third, our spin-1 DM may have a new annihilation mode into $Z'\gamma$ If this new channel is kinematically opened, the associated photon also contributes to a monochromatic peak. Besides, the photon energy is determined by m_V and $m_{Z'}$. We will study this topic in detail in Sec. 6.2.

4.3 Cross section formulas

We review how to evaluate the Sommerfeld factor and derive formulas for DM annihilation cross section. Let us consider a scattering process of $\chi^i\chi^j \to \chi^k\chi^\ell$ where X^i denotes DM multiplet. The following derivation can be applied to arbitrary DM spin by adjusting a spin-dependent factor. DM annihilation processes are described by two-body states. We start from the Schwinger-Dyson equation for the Green functions of the two-body states. This equation is derived by using equal time commutation relation for two-body states and equations of motion.

$$\left[\left(i\partial_{R^0} + \frac{\nabla_R^2}{4m} + \frac{\nabla_r^2}{m}\right) - V_Q(r) + i\frac{N}{2}\Gamma\delta^3(\boldsymbol{r})\right]\left\langle 0 \,\middle|\, \mathrm{T}\phi_b(R',\boldsymbol{r}')\phi_a^\dagger(R,\boldsymbol{r}) \,\middle|\, 0\right\rangle = i\delta^4(R-R')\delta^3(\boldsymbol{r}-\boldsymbol{r}')\delta_{ba}, \tag{4.75}$$

where m denotes DM mass and ϕ_a (ϕ_b) denotes a two-body state composed of the components of the DM multiplet $\chi^i\chi^j$ ($\chi^k\chi^\ell$). The factor of N in front of Γ denotes degrees of spin states.

$$N = \begin{cases} 4, & \text{(spin-1/2)} \\ 9. & \text{(spin-1)} \end{cases} \tag{4.76}$$

This Green function describes the process of $\phi_a(R,\boldsymbol{r}) \to \phi_b(R',\boldsymbol{r}')$, and the corresponding scattering process of components $\chi^i(t,\boldsymbol{x})\chi^j(t,\boldsymbol{y}) \to \chi^k(t,\boldsymbol{x}')\chi^\ell(t,\boldsymbol{y}')$. The coordinate $R = (R^0,\boldsymbol{R})$ denote the center mass coordinate and $\boldsymbol{r}$ denotes the relative coordinate of DM multiplets as defined in Eq. (4.41). We also define R' and $\boldsymbol{r}'$ in the same manner. The imaginary part for the diagonal component of this Green function, $\left\langle 0 \,\middle|\, T\phi_b\phi_a^\dagger \,\middle|\, 0\right\rangle$, relates with the total annihilation cross section of $\chi^i\chi^j$. We expand the Green functions into each partial wave mode.

$$\left\langle 0 \,\middle|\, \mathrm{T}\phi_b(R',\boldsymbol{r}')\phi_a^\dagger(R,\boldsymbol{r}) \,\middle|\, 0\right\rangle = \int \frac{dP^4}{(2\pi)^4} e^{-iP\cdot(R-R')} \sum_\ell \frac{2\ell+1}{4\pi} P_\ell(\cos\gamma)(-i)G_{ba}^{(E,\ell)}(r',r), \tag{4.77}$$

[11] For the $\gamma\gamma$ ($Z\gamma$) channel, for example, we simply add the values in Eq. (4.59) and Eq. (4.60) (Eq. (4.61) and Eq. (4.62)) to compare with spin-1/2 results shown in Eq. (4.73). This is because the real part of the potential is the same for both $J = 0$ and $J = 2$ states in the spin-1 system.

where γ denotes the relative angle between $\boldsymbol{r}$ and $\boldsymbol{r}'$. The NR kinetic energy for a DM pair is denoted by E as defined below.

$$E \equiv P^0 - \frac{\boldsymbol{P}}{4m} = \frac{mv^2}{4}, \tag{4.78}$$

where v denotes the relative velocity between a DM pair. The NR kinetic energies for the heavier components are expressed by subtracting the mass differences from E, $E - (m_i + m_j - 2m)$. Substituting Eq. (4.77) into Eq. (4.75), we obtain

$$\left[-\frac{1}{mr}\frac{d}{dr^2}r - \frac{\ell(\ell+1)}{mr^2} - E + V(r) - i\Gamma\frac{N\delta(r)}{8\pi r^2}\right] G_{ba}^{(E,\ell)}(r', r) = \frac{\delta(r-r')}{r^2}\delta_{ba}. \tag{4.79}$$

Throughout our analysis, we focus on the s-wave annihilation processes ($\ell = 0$), which give leading order contributions in the NR limit. Therefore, the total angular momentum, J, is equal to the total spin angular momentum, S. The leading order potential terms are spherically symmetric, and thus J is conserved in annihilation processes. We also have conservation of the total electric charge, Q. Consequently, the Green function is expressed in the diagonal form of each eigenstate for Q and J. To simplify the differential equation, we introduce

$$G_{ba}^{(E,\ell=0)}(r', r) \equiv \frac{1}{rr'} g_{ba}(r', r), \tag{4.80}$$

and obtain

$$\left[-\frac{1}{m}\frac{d^2}{dr^2} - E + V(r) - i\Gamma\frac{N\delta(r)}{8\pi r^2}\right] g_{ba}(r', r) = \delta(r-r')\delta_{ba}. \tag{4.81}$$

The cross section is expressed by the imaginary part of the solution. We obtain the leading order solution in the perturbative expansion of α_2 as shown below.[12]

$$g_{ba}(r', r)|_{\text{leading-order}} = \frac{iNm^2}{8\pi}\left[g_>(r') \cdot \Gamma \cdot g_>^{\mathrm{T}}(r)\right]_{ba}. \tag{4.82}$$

In the above expression, we introduce the solution of the following equation.

$$\left[-\frac{1}{m}\frac{d}{dr^2} - E + V(r)\right] g_{>ab}(r) = 0, \tag{4.83}$$

with the following boundary conditions.

$$g_{<ba}(r=0) = \delta_{ba}, \tag{4.84}$$

$$g_{<ba}(r=0) = (\text{outgoing mode only}). \tag{4.85}$$

We impose different profiles depending on each potential. The short-range Yukawa potential damps at $r \to \infty$, and thus the solution behaves as the outgoing plane wave. For the long-range Coulomb potential, the asymptotic profile is also determined by solving the Schrödinger

[12] The real part of the potential is $\mathcal{O}(\alpha_2)$ while the imaginary part is $\mathcal{O}(\alpha_2^2)$.

equation in Eq. (4.83). In particular, we put the following condition as the asymptotic behavior.

$$g_{>ba}(r) \to \begin{cases} d_{ba}(E_a)\ e^{i\sqrt{mE_b}r}, & \text{(short-range potential)} \\ \\ d_{ba}(E_a)\ e^{i\sqrt{mE_b}r} e^{i\frac{m\alpha}{2\sqrt{mE_b}}\log(2\sqrt{mE_b}r)}, & \text{(long-range potential)} \end{cases} \tag{4.86}$$

where E_a and E_b denote the NR kinetic energy of ϕ_a and ϕ_b, respectively. Since we can not take $r \to \infty$ in numerical calculations, we impose these asymptotic behaviors in a sufficiently large value of r ($\equiv r_f$) so that the numerical solutions turn to be independent of r_f. The distortion from the asymptotic (modified) plane wave profile is expressed by $d_{ba}(E_a)$, which is called the Sommerfeld factor.

For $Q = 0$ two-body sector, we have matrix form of the Green function and the kinematical accessibility of an off-diagonal process is nontrivial. This property is already imprinted in the above boundary conditions. Let us consider the DM process of $\chi^i\chi^j \to \chi^k\chi^\ell$. If we have $2m < m_k + m_\ell$, this scattering channel is kinematically closed for

$$E_b = \frac{mv^2}{4} - (m_k + m_\ell - 2m) < 0. \tag{4.87}$$

In this region, the exponential factor $e^{\sqrt{mE_b}r}$ damps the asymptotic solution at $r \to \infty$. This behavior is consistent with the kinematical suppression of this annihilation mode. This property is automatically encoded in the boundary condition in Eq. (4.86). We introduce M_{ij} ($M_{k\ell}$) to denote the total mass of initial (final) states. The general relation between initial and final relative velocities is expressed as

$$v_{ij}^2 = v_{k\ell}^2 - \frac{4}{m}\left(M_{k\ell} - M_{ij}\right) \equiv \frac{4k^2}{m^2}. \tag{4.88}$$

From this relation, we may obtain the general expression for $\sqrt{mE_b}$ as shown below.

$$\sqrt{mE_b} = k = \sqrt{m\Big(\frac{mv_{k\ell}^2}{4} - \frac{M_{k\ell} - M_{ij}}{m}\Big)}. \tag{4.89}$$

We find k is pure imaginary for $mv_{k\ell}^2/4 < M_{k\ell} - M_{ij}$. Therefore, we have the exponential damping of the solution, $\sim e^{-|k|r}$ for $r \to \infty$, which is also consistent with the above discussion. We solve the equation numerically and obtain the Sommerfeld factors as a function of the relative velocity for the initial state, v_{ij}. This effect gets viable in the NR region, $v_{ij} \ll 1$, since the potential energy becomes relevant compared with the kinetic energy, $E \simeq mv_{ij}^2/4$, in the Schrödinger equations. On the other hand, the enhancement factors converge to 1 for $v_{ij} \gg 1$. Consequently, we can recover the perturbative cross section obtained by the Born approximation if we replace the Sommerfeld factor with 1. Through the optical theorem, $\mathrm{Im}G_{aa}^{E,\ell=0}(r', r)$ is related to the s-wave spin-averaged and velocity weighted annihilation cross section, $(\overline{\sigma_a v})$, and we obtain the following formula.

$$(\overline{\sigma_a v})_{s\text{-wave}} = c_a\ \frac{2\pi}{k^2}\ \lim_{E\to\frac{k^2}{E^2}} \left(E - \frac{k^2}{m^2}\right)^2 \int_0^\infty dr dr' \sin kr \cdot \mathrm{Im}\left[rr' G_{aa}^{(E,\ell=0)}(r', r)\right] \cdot \sin kr', \tag{4.90}$$

where we do not take summation over a, and σ_a describes the annihilation cross section of $\phi_a \sim \chi^i\chi^j$. We introduce a pre-factor c_a as defined below.

$$c_a = \begin{cases} 2, & \text{for initial states composed of two identical particles} \\ 1. & \text{otherwise} \end{cases} \tag{4.91}$$

If we substitute the leading order solution given in Eq. (4.82), we obtain

$$(\overline{\sigma_a v})_{s\text{-wave}}|_{\text{leadingorder}} = c_a \, \frac{m^2}{k^2} \lim_{E \to \frac{k^2}{E^2}} \left(E - \frac{k^2}{m^2}\right)^2 \left[\mathcal{A}(k) \cdot \Gamma \cdot \mathcal{A}^\dagger(k)\right]_{aa}, \tag{4.92}$$

where we define

$$\mathcal{A}_{ba}(k) \equiv \int_0^\infty dr \sin kr [g_>(r)]_{ba}. \tag{4.93}$$

The asymptotic behavior $r \to \infty$ is important to evaluate $\mathcal{A}_{ba}(k)$. Substituting Eq. (4.86) into Eq. (4.93), we obtain[13]

$$\begin{aligned} \mathcal{A}_{ba}(k) &\simeq \int_0^\infty dr \cdot d_{ba}(E) \; e^{i\sqrt{mE}r} \sin kr \\ &= d_{ba}(E) \times \left(-\frac{k}{m}\right) \frac{1}{E - \frac{k}{m^2}}. \end{aligned} \tag{4.94}$$

Using this approximated form, we express the annihilation cross section as below.

$$(\overline{\sigma_a v})_{s\text{-wave}} \simeq c_a \sum_{b,c} d_{ab}(E) \; \Gamma_{bc} \; d^*_{ac}(E). \quad \text{(No summation for } a) \tag{4.95}$$

In particular, the velocity-weighted annihilation cross section for partial annihilation processes, $V^0V^0 \to XX'$, are expressed using the notation introduced in Sec. 4.2.2.[14]

$$(\overline{\sigma_a v})_{XX'} \simeq c \sum_{\alpha,\beta} \sum_{J,J_z} \left(\Gamma^J_{XX'}\right)_{\alpha\beta} d_{2\alpha}(E) \; d^*_{2\beta}(E), \tag{4.96}$$

where $c = 2$ for the initial states composed of identical particles. We introduce $E \simeq \frac{m_V v^2_{\text{rel}}}{4}$ as the NR kinetic energy of the V-particles, and $d_{\alpha\beta}(E)$ $(\alpha, \beta = 1, 2)$ as the Sommerfeld enhancement factor. We numerically obtain $d_{\alpha\beta}(E)$ by solving the Schrödinger equation following the method described above.

[13]We assume $\text{Im}(\sqrt{mE}) > 0$ to obtain this result. This assumption is consistent with the asymptotic behavior shown in Eq (4.86) for the process with $M_{ij} < M_{k\ell}$. See the discussion below Eq. (4.87).

[14]We have to choose the appropriate value of coupling constants at the typical scale of each process. We use the couplings at the m_Z scale for the potential in solving the Schrödinger equation, while we use the couplings at DM mass for $\Gamma^J_{XX'}$ in Eq. (4.96).

5 Thermal relic evaluation

We evaluate thermal relic abundance predicted in the electroweakly interacting DM system. The DM thermal relic abundance is one of the most important predictions in WIMP scenario because we can infer one constraint on the DM theory by requiring to realize the value determined in the Planck experiments, $\Omega h^2 \simeq 0.12$. DM annihilation channels and cross section differ in each theory. Therefore, specifying the viable DM mass region for the WIMP scenario is the first step of DM identification.

In order to evaluate thermal relic abundance, we have to derive all the relevant annihilation cross section formulas for DM multiplet. Besides, we need to numerically evaluate the Sommerfeld factors for all the two-body states. We compare predictions between spin-1/2 and spin-1 DM and discuss possibilities for discrimination. The derived formulas in this section are also applied to study gamma-ray signatures discussed in Sec. 6. In Sec. 5.1, we classify all the annihilation diagrams of V-particles systematically. Through this classification, we specify the relevant modes to evaluate the DM abundance. The cross section formulas are summarized in Sec. 5.2. In Sec. 5.3, we show the numerical result of thermal relic evaluation.

5.1 Classification of annihilation diagrams

To collect all the leading-order contributions, we categorize annihilation diagrams of spin-1 DM by the following features.

(1) Initial states

(2) Final states

(3) Topology of diagrams

The initial and final states are characterized by the particle spices and the total spin angular momentum. We introduce labels for categorization in Sec. 5.1.1 and write down all the possible combinations of each label in Sec. 5.1.2.

5.1.1 Labels for categorization

First, we define labels of the initial state particles. As revealed in Sec. 3.3, we have nearly degenerated Z_2-odd spin-1 particles, V^0 and $V^\mp$ in our spin-1 DM system.[15] If the mass splitting between the V-particles, δm, is comparable with the temperature in the thermal bath, the coannihilation effects are viable. To evaluate the DM thermal relic abundance, we need to calculate the annihilation cross section of V-particles.[16] Pairs of V-particles, which

[15] We assume $m_{h_D} > m_V$ to focus on the spin-1 DM scenario, and thus h_D has nothing to do with the thermal relic evaluation. This relation is always achieved by choosing the parameters in the scalar sector.

[16] The scattering between V-particles and the decay of $V^\pm$ into V^0 do not directly reduce the total number of V-particles. Although these processes are assumed to occur with sufficient rate, we do not have to calculate explicitly.

are denoted by V_1V_2, are written down below.

$$V_1V_2 = \{V^0V^0, V^-V^+, V^0V^\mp, V^\mp V^\mp\}. \tag{5.1}$$

We also classify each initial state by the total spin angular momentum, $J_{\rm initial} = 0, 1, 2$ for the later convenience. Each initial state mode is specified by $(V_1V_2, J_{\rm initial})$.

Second, we define the labels to express the final state particles.

$$X_3X_4 = \{\phi_3\phi_4, \phi_3V_4, f_3f_4, V_3V_4\}, \tag{5.2}$$

where ϕ_i, f_i and V_i $(i = 3, 4)$ denote final state particles with spin-0, 1, and 2, respectively. The final states are composed of all parity-even particles due to the Z_2-charge conservation. Each final state is also classified by the total angular momentum, $J_{\rm final} = 0, 1, 2$, and specified by $(X_3X_4, J_{\rm final})$.

Third, the annihilation diagrams for V-particles are classified into the following two classes of the topology.

- *Topology s*

  The diagrams of the s-channel are classified into this class. These classes of diagrams are further labeled by the intermediate states. We use φ for spin-0 mediators and use X for spin-1 mediators, respectively. Therefore, each s-channel diagram is assigned by the labels of s-φ or s-X.

- *Topology tu4*

  The diagrams of t-channel, u-channel, and quadratic channel are classified into this class. We have nonzero amplitude in specific partial wave modes after adding up the three channels if we focus on NR leading order contributions.

All the partial wave annihilation modes of V-particles are specified by the following labels.

$$(V_1V_2, J_{\rm initial})\text{-}([\text{Topology}], X_3X_4, J_{\rm final}), \tag{5.3}$$

where [Topology] = s-φ, s-X for the topology s, and [Topology] = $tu4$ for the topology $tu4$. Once we assign these labels to each annihilation mode, we treat all the contributions systematically. Besides, possible annihilation channels are efficiently constrained due to the physical reasons by decomposing into each partial wave mode. For instance, we focus on the s-wave contribution throughout our analysis, and thus the total spin angular momentum is conserved.

$$J_{\rm initial} = J_{\rm final} \equiv J. \tag{5.4}$$

This constraint drastically reduces the number of possible annihilation modes in the partial wave basis. We also have p-wave or higher contributions if we include the relativistic corrections, which is sub-leading to the s-wave contribution in the NR limit.

5.1.2 Possible annihilation modes

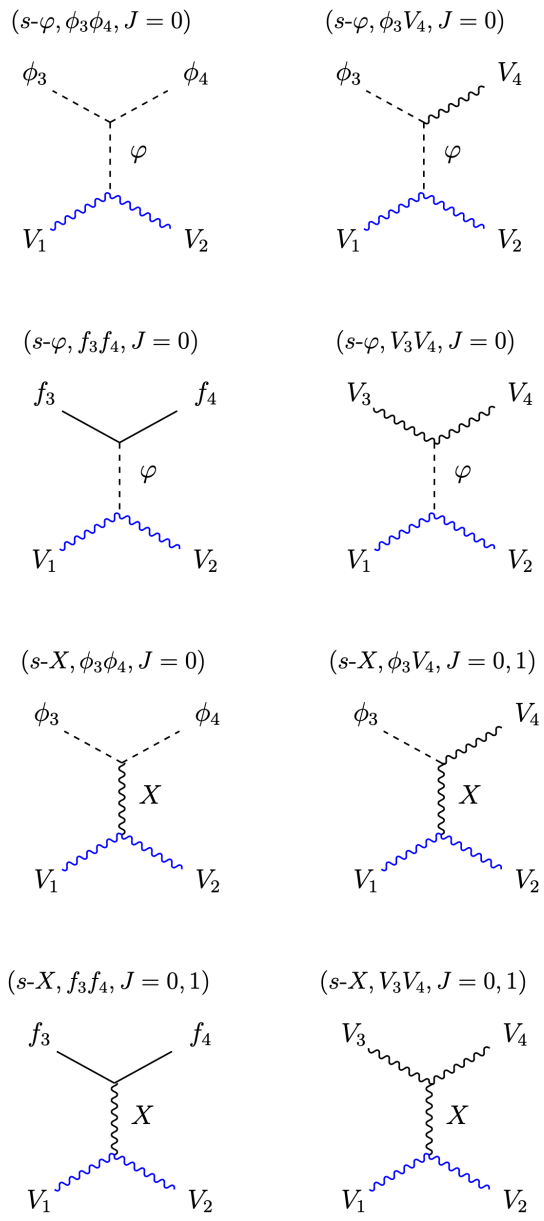

Figure 7: Annihilation diagrams of V-particles categorized with the topology s.

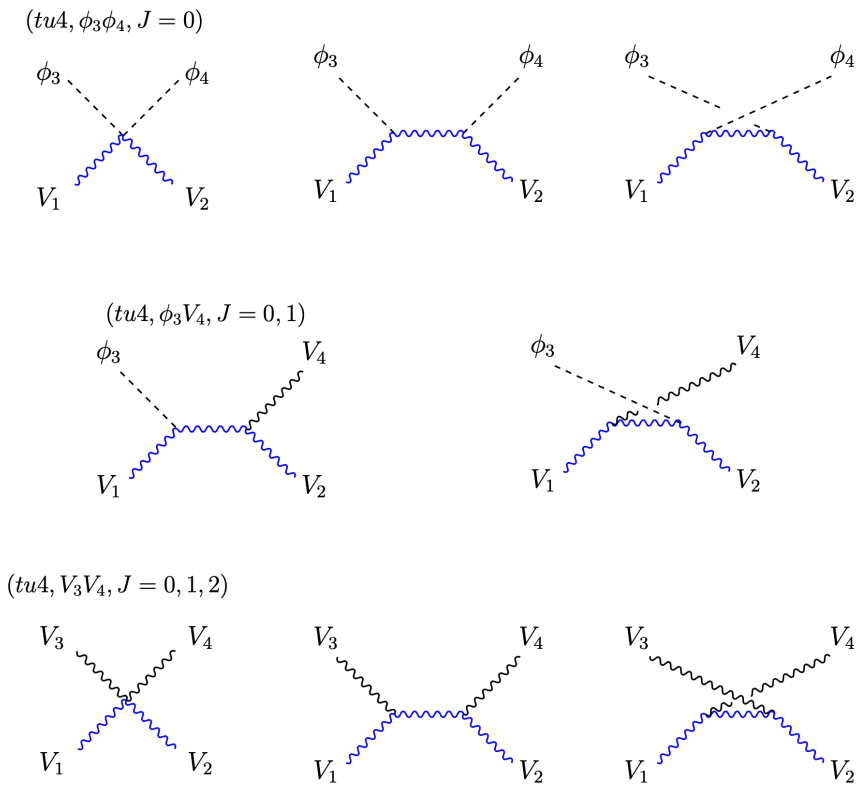

Figure 8: Annihilation diagrams of V-particles with the topology $tu4$.

We write down all the possible labels defined in Eq. (5.3). Only the limited combinations of labels are consistent with the conservation laws of the total electric charge, Q, and the total spin angular momentum, J.

- Possible initial states

  We have the following combinations of two V-particles where all the possible values of J are shown.

$$\begin{aligned}(V_1, V_2, J) = &(V^0V^0, J = 0, 2),\\ &(V^-V^+, J = 0, 1, 2),\\ &(V^0V^\mp, J = 0, 1, 2),\\ &(V^\mp V^\mp, J = 0, 2).\end{aligned} \tag{5.5}$$

  We do not have $J = 1$ state for V^0V^0 and $V^\mp V^\mp$ as long as we are focusing on the s-wave contribution due to the following reasons: Note that these states are composed of the two identical particles with Bose statics whose total wave function must be symmetric under the exchange of two wave functions. Since the s-wave spatial wave function is symmetric under the exchange of two V-particles, the spin wave function should be also symmetric under the exchange. Therefore, $J = 1$ states are forbidden by the wrong

spin-statics. If we consider the relativistic corrections, the $J = 1$ contributions appear even for V^0V^0 and $V^\mp V^\mp$ states.

- Possible final states with the topology s

  The diagrams with the topology s are categorized into the eight types of diagrams as shown in Fig. 7. All the possible labels are listed below.

$$\begin{aligned}([\text{Class}]\text{-}[\text{intermediate state}], [\text{final state}], J) = {} & (s\text{-}\varphi, \phi_3\phi_4, J = 0), \\ & (s\text{-}\varphi, \phi_3 V_4, J = 0), \\ & (s\text{-}\varphi, f_3 f_4, J = 0), \\ & (s\text{-}\varphi, V_3 V_4, J = 0), \\ & (s\text{-}X, \phi_3\phi_4, J = 0, 1), \\ & (s\text{-}X, \phi_3 V_4, J = 0, 1), \\ & (s\text{-}X, f_3 f_4, J = 0, 1), \\ & (s\text{-}X, V_3 V_4, J = 0, 1), \end{aligned} \tag{5.6}$$

  where $\varphi = h, h'$ denote the intermediate spin-0 particles and $X = \gamma, Z, W, Z', W'$ denote the intermediate spin-1 particles.[17] We have no final states with $J = 2$ for the topology s since we do not have spin-2 mediators.

- Possible final states with the topology $tu4$

  The diagrams with the topology $tu4$ have three possibilities in the final state particles, $\phi_3\phi_4$, $\phi_3 V_4$, and $V_3 V_4$.[18] In Fig. 8, we show these three types by specifying the corresponding diagrams. The following combinations of labels are possible.

$$\begin{aligned}([\text{Class}], [\text{final state}], J_{\text{final}}) = {} & (tu4, \phi_3\phi_4, J = 0, 1, 2), \\ & (tu4, \phi_3 V_4, J = 0, 1, 2), \\ & (tu4, V_3 V_4, J = 0, 1, 2). \end{aligned} \tag{5.7}$$

  Note that final state particles have nonzero momentum, and thus the total angular momentum J acquires contributions not only from the spin angular momentum but also the orbital angular momentum.[19]

In Table 4, we classify the initial and final states for each total angular momentum J. The states with the same J are allowed to have nonzero annihilation amplitude due to the total spin angular momentum conservation in the s-wave contribution. Thanks to this constraint, we can reduce the number of annihilation modes we have to consider.

[17] We only have $J = 1$ contribution for $X = \gamma$ since a photon has only transverse modes. On the other hand, we have both $J = 0$ and $J = 1$ contribution from massive bosons since these particles have a longitudinal mode corresponding to the NG boson.

[18] We have no annihilation mode into fermions for topology $tu4$ at the tree-level because we do not have Z_2-odd fermions.

[19] As shown in Sec. 5.2, nonzero cross sections are obtained only for specific values of J due to the (anti)symmetricity of the amplitudes.

Table 4: Possible combination of the initial and final states where X_3X_4 represents all the possible final states introduced in Eq. (5.2).

angular momentum	initial state	final state
$J=0$	$(V^0V^0,0)$	$(s\text{-}\varphi,\ X_3X_4,0)$ with $\varphi=h,h'$
	$(V^-V^+,0)$	$(s\text{-}X,\ X_3X_4,0)$ with $X=Z,W,Z',W'$ (longitudinal)
	$(V^0V^\mp,0)$	$(tu4,\ \phi_3\phi_4,0)$
	$(V^\mp V^\mp,0)$	$(tu4,\ \phi_3V_4,0)$
		$(tu4,\ V_3V_4,0)$
$J=1$	$(V^-V^+,1)$	$(s\text{-}X,\ X_3X_4,1)$ with $X=\gamma,Z,W,Z',W'$ (transverse)
	$(V^0V^\mp,1)$	$(tu4,\ \phi_3V_4,1)$
		$(tu4,\ V_3V_4,1)$
$J=2$	$(V^0V^0,2)$	$(tu4,\ \phi_3\phi_4,2)$
	$(V^-V^+,2)$	$(tu4,\ \phi_3V_4,2)$
	$(V^0V^\mp,2)$	$(tu4,\ V_3V_4,2)$
	$(V^\mp V^\mp,2)$	

5.2 Summary of annihilation modes

Combining initial and final states in the same row of Table 4, we can systematically obtain all the possible annihilation modes of the V-particles. In Sec. 5.2.1, we write down the annihilation modes by specifying the particle species in intermediate and final states. Focusing on the leading order contributions, we show the master formulas of the annihilation cross section in Sec. 5.2.2.

5.2.1 All the possible modes

All the possible annihilation modes are summarized in Table 5-8. The first column shows the labels indicating each mode, the second column shows possible intermediate and final states, and the third column shows descriptions for each mode, respectively. We specified the leading order (LO) contributions in these columns as remarked by red characters. We also show the reasons for suppression in the cross section for the sub-leading modes, which depends both on the model parameters and on the specific limit. The detailed explanations of each mode are listed below. These explanations are cited in Table 5-8.

- ♭ The neutral vector triple couplings are forbidden at the tree-level.
- ♯ The neutral vector quadratic couplings are forbidden at the tree-level.
- $*$ This mode may be kinematically allowed depending on $m_{Z'}$ ($\simeq m_{W'}$).
- △ This mode may be kinematically allowed depending on $m_{h'}$.
- ★ The final states composed of two heavier Z_2-even vectors (eg. $W'W'$, $W'Z'$, $Z'Z'$) are forbidden kinematically since we have $m_{Z',W'} > m_V$ in our setup.
- ♠ A longitudinal mode of a massive boson contributes to this $J = 0$ mode, while a photon only has transverse modes and does not contribute.
- ♣ The transverse modes of massive bosons may only contribute to this $J = 1$ mode.
- ♦ In order to realize $J = 0$ modes, a final massive vector must have a longitudinal polarization that corresponds to the Nambu-Goldstone (NG) boson. Since we have no tree-level coupling of neutral NG bosons such as V^--V^+-π^Z and V^--V^+-$\pi^{Z'}$, these modes are suppressed by $\mathcal{O}((v/v_\Phi)^2)$.
- ♢ We have tree-level couplings of charged NG bosons such as V^0-$V^\mp$-π^W and V^0-$V^\mp$-$\pi^{W'}$, and thus these modes do not have $\mathcal{O}((v/v_\Phi)^2)$ suppression. However, these modes are proportional to the initial DM momentum and sub-leading in the NR limit.
- ♡ If the final states are composed of two identical Bosons, $J = 1$ states are forbidden in the s-wave contributions due to the spin-statistics.

The following facts can be read out from these tables: We found the s-channel diagrams are all sub-leading due to the $\sin\phi_h$ suppression and momentum suppression in the NR limit, respectively. Lacking the s-channel annihilation modes, the annihilation modes into fermion pairs do not contribute to the leading order effects. This is because we do not have the Z_2-odd fermion in our framework. Consequently, we can focus on the following final states in the leading order calculation.

$$\{(tu4, \phi_3\phi_4, J), (tu4, \phi_3 V_4, J), (tu4, V_3 V_4, J)\}. \tag{5.8}$$

We will perform a more detailed classification of the annihilation modes and show the cross section formulas in Sec. 5.2.2.

Table 5: Possible annihilation modes for V^0V^0 ($J = 0, 2$). The $J = 1$ modes are forbidden in the s-wave contribution due to the spin-statics.

label	intermediate/final state	description
$(V^0V^0, 0)$-(s-φ, $X_3X_4, 0$)	$\varphi = h, h'/X_3X_4$	Suppressed by $(v/v_\Phi)^2$ and $(\sin 2\phi_h)^2$
$(V^0V^0, 0)$-(s-X, $X_3X_4, 0$)	—	No contribution at the tree-level$^\flat$
$(V^0V^0, 0)$-($tu4$, $\phi_3\phi_4, 0$)	hh	Suppressed by $(\sin\phi_h)^4$
	hh'	Suppressed by $(\sin 2\phi_h)^2$$^\triangle$
	$h'h'$	LO if kinematically allowed$^\triangle$
$(V^0V^0, 0)$-($tu4$, $\phi_3 V_4, 0$)	—	No contribution at the tree-level$^\flat$
$(V^0V^0, 0)$-($tu4$, $V_3V_4, 0$)	$W^\mp W^\pm$	LO
	$W^-W'^+, W'^-W^+$	LO if kinematically allowed*
	$W'^-W'^+, Z'Z'$	Kinematically forbidden$^\bigstar$
	$\gamma\gamma, \gamma Z, ZZ, \gamma Z', ZZ'$	No contribution at the tree-level$^{\flat\sharp}$
$(V^0V^0, 0)$-($tu4$, $\phi_3\phi_4, 2$)	hh	Suppressed by $(\sin\phi_h)^4$
	hh'	Suppressed by $(\sin 2\phi_h)^2$$^\triangle$
	$h'h'$	LO if kinematically allowed$^\triangle$
$(V^0V^0, 2)$-($tu4$, $V_3V_4, 2$)	$W^\mp W^\pm$	LO
	$W^-W'^+, W'^-W^+$	LO if kinematically allowed*
	$W'^-W'^+, Z'Z'$	Kinematically forbidden$^\bigstar$
	$\gamma\gamma, \gamma Z, ZZ, \gamma Z', ZZ'$	No contribution at the tree-level$^{\flat\sharp}$

Table 6: Possible annihilation modes for V^-V^+ $(J = 0, 1, 2)$.

label	intermediate / final state	description
$(V^-V^+, 0)$-$(s$-$\varphi,\ X_3X_4, 0)$	$\varphi = h, h'/X_3X_4$	Suppressed by $(v/v_\Phi)^2$ and $(\sin 2\phi_h)^2$
$(V^-V^+, 0)$-$(s$-$X,\ X_3X_4, 0)$	$X = Z, Z'^{\spadesuit}/X_3X_4$	No direct emission of NG boson$^{\blacklozenge}$ and sub-leading in NR limit
$(V^-V^+, 0)$-$(tu4,\ \phi_3\phi_4, 0)$	hh	Suppressed by $(\sin\phi_h)^4$
	hh'	Suppressed by $(\sin 2\phi_h)^{2\triangle}$
	$h'h'$	LO if kinematically allowed$^{\triangle}$
$(V^-V^+, 0)$-$(tu4,\ \phi_3V_4, 0)$	$hZ, h'Z, hZ', h'Z'$	No direct emission of NG boson$^{\blacklozenge}$
$(V^-V^+, 0)$-$(tu4,\ V_3V_4, 0)$	$W^\mp W^\pm, \gamma\gamma, \gamma Z, ZZ$	LO
	$W^-W'^+, W'^-W^+, \gamma Z', ZZ'$	LO if kinematically allowed*
	$W'^-W'^+, Z'Z'$	Kinematically forbidden$^{\bigstar}$
$(V^-V^+, 1)$-$(s$-$X,\ X_3X_4, 1)$	$X = \gamma, Z, Z'^{\clubsuit}/X_3X_4$	Sub-leading in NR limit
$(V^-V^+, 1)$-$(tu4,\ \phi_3V_4, 1)$	$h\gamma, hZ, hZ'$	Suppressed by $(\sin\phi_h)^2$
	$h'\gamma, h'Z, h'Z'$	LO if kinematically allowed$^{\triangle}$
$(V^-V^+, 1)$-$(tu4,\ V_3V_4, 1)$	$W^\mp W^\pm$	LO
	$W^-W'^+, W'^-W^+$	LO if kinematically allowed*
	$\gamma\gamma, ZZ$	Forbidden by the spin statistics$^{\heartsuit}$
	$\gamma Z, \gamma Z', ZZ'$	Sub-leading in NR limit
	$W'^-W'^+,\ Z'Z'$	Kinematically forbidden$^{\bigstar}$
$(V^-V^+, 2)$-$(tu4,\ V_3V_4, 2)$	$W^\mp W^\pm, \gamma\gamma, \gamma Z, ZZ$	LO
	$W^-W'^+, W'^-W^+, \gamma Z', ZZ'$	LO if kinematically allowed*
	$W'^-W'^+, Z'Z'$	Kinematically forbidden$^{\bigstar}$

Table 7: Possible annihilation modes from $V^0V^\mp(J=0,1,2)$.

label	intermediate / final state	description
$(V^0V^\mp,0)$-(s-φ, $X_3X_4,0$)	$\varphi=h,h'/X_3X_4$	Suppressed by $(v/v_\Phi)^2$ and $(\sin 2\phi_h)^2$
$(V^0V^\mp,0)$-(s-X, $X_3X_4,0$)	$X=W,W'^{\spadesuit}/X_3X_4$	We have direct emission of NG boson but sub-leading in NR limit$^{\diamond}$
$(V^0V^\mp,0)$-($tu4$, $\phi_3V_4,0$)	hW,hW'	Suppressed by $(\sin\phi_h)^2$
	$h'W,h'W'$	LO if kinematically allowed$^{\triangle}$
$(V^0V^\mp,0)$-($tu4$, $V_3V_4,0$)	$\gamma W^\mp,ZW^\mp$	LO
	$\gamma W'^\mp,Z'W^\mp,ZW'^\mp$	LO if kinematically allowed*
	$Z'W'^\mp$	Kinematically forbidden$^{\bigstar}$
$(V^0V^\mp,1)$-(s-X, $X_3X_4,1$)	$X=W,W'^{\clubsuit}/X_3X_4$	Sub-leading in NR limit
$(V^0V^\mp,1)$-($tu4$, $\phi_3V_4,1$)	hW,hW'	Suppressed by $(\sin\phi_h)^2$
	$h'W$, $h'W'$	LO if kinematically allowed$^{\triangle}$
$(V^0V^\mp,1)$-($tu4$, $V_3V_4,1$)	$\gamma W^\mp,ZW^\mp,Z'W^\mp,$	Sub-leading in NR limit
	$Z'W'^\mp$	Kinematically forbidden$^{\bigstar}$
$(V^0V^\mp,2)$-($tu4$, $V_3V_4,2$)	$\gamma W^\mp,ZW^\mp,Z'W^\mp,$	LO
	$\gamma W'^\mp,ZW'^\mp$	LO if kinematically allowed*
	$Z'W'^\mp$	Kinematically forbidden$^{\bigstar}$

5.2.2 Master formulas of annihilation cross section

We show formulas of spin-averaged perturbative annihilation cross section between V-particles focusing on the leading order effects. In Table 9, we summarize the channels that may induce the leading order effects. The first column shows the label of each mode, the second column shows the relevant diagrams, the third column shows the definition of the types for the cross section formulas, and the fourth column shows the factors of couplings in the cross sections, respectively. We use the definitions for the scalar-vector couplings and the vector triple couplings shown in Sec. 3.3.2. We use the relations between quadratic couplings and triple couplings to simplify the cross section formulas.

There are nine labels of leading order channels divided into four types, Type-A, -B, -C, and -D, which label the cross section formulas. The formulas for the spin-averaged cross

Table 8: Possible annihilation modes from $V^{\mp}V^{\mp}(J=0,2)$. The $J=1$ modes are forbidden in the s-wave contribution due to the spin-statistics. We only have two vector final states since we lack charged scalars in our spectrum. The final states with two fermions are not allowed since we have no doubly charged mediator.

label	intermediate/final state	description
$(V^{\mp}V^{\mp},0)$-$(tu4,\ V_3V_4,0)$	$W^{\mp}W^{\mp}$	LO
	$W^{\mp}W'^{\mp}$	LO if kinematically allowed*
	$W'^{\mp}W'^{\mp}$	Kinematically forbidden★
$(V^{\mp}V^{\mp},2)$-$(tu4,\ V_3V_4,2)$	$W^{\mp}W^{\mp}$	LO
	$W^{\mp}W'^{\mp}$	LO if kinematically allowed*
	$W'^{\mp}W'^{\mp}$	Kinematically forbidden★

section, which is divided by 1/9, are derived as follows.

$$\overline{(\sigma v_{\rm rel})}^{J=0}_{\text{Type-A}} = \frac{(\text{PS})}{36m_V^2}\cdot(\text{coupling})\cdot\frac{\left[40m_V^4-2m_V^2(m_3^2+m_4^2)+(m_3^2-m_4^2)^2\right]^2}{48m_V^8(4m_V^2-m_3^2-m_4^2)^2}, \tag{5.9}$$

$$\overline{(\sigma v_{\rm rel})}^{J=1}_{\text{Type-A}} = 0, \tag{5.10}$$

$$\overline{(\sigma v_{\rm rel})}^{J=2}_{\text{Type-A}} = \frac{(\text{PS})}{36m_V^2}\cdot(\text{coupling})\cdot\frac{\left[16m_V^4-8m_V^2(m_3^2+m_4^2)+(m_3^2-m_4^2)^2\right]^2}{120m_V^8(4m_V^2-m_3^2-m_4^2)^2}, \tag{5.11}$$

$$\overline{(\sigma v_{\rm rel})}^{J=0,2}_{\text{Type-B}} = 0, \tag{5.12}$$

$$\overline{(\sigma v_{\rm rel})}^{J=1}_{\text{Type-B}} = \frac{(\text{PS})}{108m_V^4}\cdot(\text{coupling})\cdot\left(\frac{1}{4m_V^2-m_3^2-m_4^2}\right)^2\left(4-\frac{m_4^2}{m_V^2}\right)^2 \times\left[16m_V^4-8m_V^2(m_3^2+m_4^2)+(m_3^2-m_4^2)^2\right], \tag{5.13}$$

$$\overline{(\sigma v_{\rm rel})}^{J}_{\text{Type-C}} = \frac{(\text{PS})}{9m_V^2}\cdot(\text{coupling})\cdot\overline{|\tilde{\mathcal{M}}^J|^2}, \quad (\text{for } J=0,2) \tag{5.14}$$

$$\overline{(\sigma v_{\rm rel})}^{J=1}_{\text{Type-C}} = 0, \tag{5.15}$$

$$\overline{(\sigma v_{\rm rel})}^{J}_{\text{Type-D}} = \frac{(\text{PS})}{36m_V^2}\cdot(\text{coupling})\cdot\overline{|\tilde{\mathcal{M}}^J|^2}, \quad (\text{for } J=0,1,2) \tag{5.16}$$

where $m_i(i=3,4)$ denote the masses of final state particles and (coupling) represents the factors shown in the fourth column of Table 9. The phase space in the center mass frame is

Table 9: Annihilation modes and topology of the diagrams that may induce the leading order effects. We categorize these modes into four types, Type-A, -B, -C, and -D.

label of mode	diagrams	Type	couplings
(V^0V^0, J)-$(tu4,\ \phi_3\phi_4, J)$	4-, t-, u-channel	Type-A	$g^2_{\phi_3}g^2_{\phi_4}$
(V^-V^+, J)-$(tu4,\ \phi_3\phi_4, J)$	4-, t-, u-channel	Type-A	$g^2_{\phi_3}g^2_{\phi_4}$
(V^-V^+, J)-$(tu4,\ \phi_3V_4^0, J)$	t-, u-channel	Type-B	$g^2_{\phi_3}g^2_{V^+V^-V_4^0}$
$(V^0V^\mp, J)$-$(tu4,\ \phi_3V_4^\mp, J)$	t-, u-channel	Type-B	$g^2_{\phi_3}g^2_{V_4^+V^-V^0}$
(V^0V^0, J)-$(tu4,\ V_3^-V_4^+, J)$	4-, t-, u-channel	Type-C	$g^2_{V_3^+V^-V^0}g^2_{V^+V_4^-V^0}$
(V^-V^+, J)-$(tu4,\ V_3^-V_4^+, J)$	4-, t-channel	Type-D	$g^2_{V_3^+V^-V^0}g^2_{V^+V_4^-V^0}$
(V^-V^+, J)-$(tu4,\ V_3^0V_4^0, J)$	4-, t-, u-channel	Type-C	$g^2_{V^+V^-V_3^0}g^2_{V^+V^-V_4^0}$
$(V^0V^\mp, J)$-$(tu4,\ V_3^0V_4^\mp, J)$	4-, u-channel	Type-D	$g^2_{V^+V^-V_3^0}g^2_{V_4^+V^-V^0}$
$(V^\mp V^\mp, J)$-$(tu4,\ V_3^\mp V_4^\mp, J)$	4-, t-, u-channel	Type-C	$g^2_{V_3^+V^-V^0}g^2_{V_4^+V^-V^0}$

given below.

$$(\mathrm{PS}) \equiv c_{34}\int d\Pi_{34} = \frac{c_{34}}{8\pi}\sqrt{1-\frac{2(m_3^2+m_4^2)}{s}+\left(\frac{m_3^2-m_4^2}{s}\right)^2}, \tag{5.17}$$

where $c_{34} = 1/2$ for the final states composed of two identical particles and otherwise $c_{34} = 1$. In the NR limit of the initial V-particles, we have $s \simeq 4m_V^2$.

To express the cross section for Type-C and Type-D, we introduce the following squared amplitudes which are taken averaged for polarization indices and $\cos\theta$ dependence.

$$\overline{\left|\tilde{\mathcal{M}}^J\right|^2} \equiv \frac{1}{2}\int_{-1}^{1} d\cos\theta \sum_{a,b} |\tilde{\mathcal{M}}^{J,J_z}_{ab}|^2, \qquad (|J_z| \le J) \tag{5.18}$$

where the sum over a, b is taken over physical polarization for the final vectors. The most

general expressions are shown below.

$$\overline{\left|\tilde{\mathcal{M}}^{J=0}\right|^2} = \frac{1}{192m_V^8(4m_V^2-m_3^2-m_4^2)^2} \times \Big[18432m_V^{12} - 15360m_V^{10}\left(m_3^2+m_4^2\right) + 128m_V^8\left(37m_3^4+37m_4^4+82m_3^2m_4^2\right) - 640m_V^6\left(m_3^2+m_4^2\right)^3 + 32m_V^4\left(m_3^8+m_4^8+2m_3^6m_4^2+2m_3^2m_4^6+10m_3^4m_4^4\right) + m_3^2m_4^2\left(m_3^2-m_4^2\right)^4\Big], \tag{5.19}$$

$$\overline{\left|\tilde{\mathcal{M}}^{J=1}\right|^2} = \frac{16m_V^4\left(m_3^2+m_4^2\right) - 8m_V^2\left(m_3^4+m_4^4-4m_3^2m_4^2\right) + \left(m_3^2+m_4^2\right)\left(m_3^2-m_4^2\right)^2}{24m_V^4(4m_V^2-m_3^2-m_4^2)}, \tag{5.20}$$

$$\overline{\left|\tilde{\mathcal{M}}^{J=2}\right|^2} = \frac{1}{480m_V^8(4m_V^2-m_3^2-m_4^2)^2} \times \Big[49152m_V^{12} - 18432m_V^{10}\left(m_3^2+m_4^2\right) + 256m_V^8\left(2m_3^4+2m_4^4+149m_3^2m_4^2\right) + 128m_V^6\left(m_3^6+m_4^6-18m_3^4m_4^2-18m_3^2m_4^4\right) + 32m_V^4\left(m_3^8+m_4^8-31m_3^6m_4^2-31m_3^2m_4^6+88m_3^4m_4^4\right) + 24m_V^2m_3^2m4^2\left(m_3^2-m_4^2\right)^2\left(m_3^2+m_4^2\right) + m_3^2m_4^2\left(m_3^2-m_4^2\right)^4\Big]. \tag{5.21}$$

The comments on these derived formulas are summarized below: First, we obtain nonzero results for the specific partial wave modes due to the following reasons. For Type-A, the amplitude turns to be symmetric under two initial $V-$particles after adding all the diagrams. Therefore, we have no $J=1$ contribution. For Type-B, $J=0,2$ modes are exactly canceled between t-channel and u-channel, and only $J=1$ cross section remains nonzero. Although both Type-C and Type-D have two vector states in initial and final states, we obtain different formulas. The difference comes from the variations of the diagrams and the vector quadratic couplings. For Type-C, the $J=1$ contribution vanishes after adding up all the diagrams while the $J=0,2$ contribution remains nonzero. For Type-D, on the other hand, we obtain nonzero cross sections for $J=0,1,2$ in general.

Second, we can apply Eqs. (5.12)-(5.16) even for the channels including photons in the final state. For the photon channels, we have to omit the longitudinal contributions from the polarization sum, which is automatically done by taking a massless limit of a final vector mass. In Eq. (5.13) for Type-B mode, the longitudinal contributions are all canceled in the final results. This is because a longitudinal mode corresponds to the NG boson contribution of a final state vector, which can not form $J=1$ states with the scalar particle. Therefore, Eq. (5.13) can be applied for photon channels by taking $m_4 \to 0$. In Eqs. (5.14)-(5.16) for Type-C and Type-D, we have nonzero contributions from the longitudinal modes in the final forms but all these longitudinal contributions are proportional to masses of final vector particles. Therefore, we can apply Eqs. (5.14)-(5.16) for photon channels by taking a massless

limit of final vectors. We may derive these formulas for photon channels directly by switching off the longitudinal polarization.

5.2.3 Perturbative cross section

In Figs. 9-18, we plot perturbative results of the spin-averaged cross section for the relevant annihilation modes of V-particles as functions of DM mass. We changed the mass ratio between DM and Z_2-even vector (scalar), $m_{Z'}/m_V$ ($m_{h'}/m_V$), to show the parameter dependence. The scalar mixing angle is fixed to be $\phi_h = 0.1$ in all panels.[20] The parameters are shown on the upper sides of each panel. Since we fix the ratio $m_{Z'}/m_V$ and $m_{h'}/m_V$ in these plots, the dominant parts of the spin-averaged annihilation cross sections scale as $\propto 1/m_V^2$ for all the modes except for Type-D two vector channels with $J = 1$, which appear in Fig. 12 and Fig. 15. This is because the cross sections of these channels are proportional to the squared masses of the final state vectors, $m_3^2 m_4^2$ (See Eq. (B.24)). Each channel is kinematically allowed for $2m_V \geq m_3 + m_4$. Therefore, these annihilation cross sections into the SM vectors scale higher negative order of m_V. The cross section may depend on $m_{Z'}$ through couplings. In Fig. 19, we plot the scalar-vector couplings, g_ϕ ($\phi = h, h'$), and the vector triple coupling for Z' and W', $g_{Z'}$. The scalar-vector couplings are normalized by DM mass to show the dimensionless values. These couplings are enhanced for the degenerated region, $m_{Z'} \simeq m_V$, and thus the associated annihilation channels may get relevant.

In Fig. 9, we show the annihilation cross section for V^0V^0 ($J = 0$). We have five annihilation modes $\{hh, hh', h'h', WW, WW'\}$. The annihilation modes into the SM Higgs are suppressed by small ϕ_h while the $h'h'$ mode may give leading order contribution if kinematically allowed. The scalar states get more relevant for $m_{Z'}/m_V \simeq 1$ due to the enhancement of the scalar-vector couplings. In all panels, two vector channels dominate the cross section. The WW' mode is larger for $m_{Z'}/m_V \simeq 1$ due to the enhancement of $g_{Z'}$. After decoupling of the WW' channel, the WW channel dominates the cross section. Figure 10 shows the $V^0V^0(J = 2)$ annihilation cross sections into $\{hh, hh', h'h', WW, WW'\}$. The behaviors are the same as described in Fig. 9. In Fig. 11, we show the annihilation cross section for V^-V^+ ($J = 0$) into $\{hh, hh', h'h', WW, WW', \gamma\gamma, \gamma Z, ZZ, \gamma Z', ZZ'\}$ where final states of two neutral vectors newly appear compared with Fig. 9. The V^-V^+ state may annihilate into $J = 1$ states as shown in Fig. 12. we have eight annihilation modes into $\{h\gamma, hZ, hZ', h'\gamma, h'Z, h'Z', WW, WW'\}$. The $h'V_4$ modes ($V_4 = \gamma, Z, Z'$) may dominate cross section because we have no ϕ_h suppression. After decoupling of these $h'V_4$ modes, the hV_4 modes get dominant. The cross sections for the two vector states are highly suppressed by m_W^2 and sub-leading in all the panels. In Fig. 13, we show $V^-V^+(J = 2)$ annihilation cross section into $\{WW, WW', \gamma\gamma, \gamma Z, ZZ, \gamma Z', ZZ'\}$. In Fig. 14, we show $V^0V^-(J = 0)$ annihilation cross section into $\{\gamma W, ZW, \gamma W', Z'W, ZW'\}$. In Fig. 15, we show $V^0V^-(J = 1)$ annihilation cross section into $\{hW, h'W, hW', ZW, Z'W, ZW'\}$. The annihilation modes including γW and $\gamma W'$ vanish since $J = 1$ contributions vanish in the massless limit of the final vector mass. The $Z'W$ and ZW' modes almost degenerate in the figure. In Fig. 16,

[20] Although the SM Higgs channels are not the leading order due to the small ϕ_h suppression, we show these modes in the figures to show the irrelevance to the other channels.

we show $V^0V^-(J=2)$ annihilation into $\{\gamma W, ZW, \gamma W', Z'W, ZW'\}$. In Fig. 17, we show $V^-V^-(J=0)$ annihilation into $\{WW, WW'\}$. In Fig. 18, we show $V^-V^-(J=2)$ annihilation into $\{WW, WW'\}$.

5.3 Evaluation of thermal relic abundance

The DM thermal relic abundance is numerically evaluated by solving the Boltzmann equations as reviewed in Sec. 2.1. Since we have degenerated spectrum of the Z_2-odd particles in the electroweakly interacting DM system, coannihilation effects, which are reviewed in Sec. 2.2, get viable to evaluate the correct abundance. We apply the general formulas to the concrete models. We derive the effective cross section predicted in the Wino system and non-abelian vector DM system and compare the results.

5.3.1 Effective annihilation cross section for Wino DM

The effective annihilation cross section of DM multiplets is expressed as shown below.

$$\sigma_{\rm eff} v = \sum_i \sum_j \sigma_{ij} v \; r_i r_j, \tag{5.22}$$

where $i = 0, -, +$ denotes the label of each component field and r_i is defined in Eq. (2.32).[21] In this system, we have

$$\Delta_0 = 0, \tag{5.23}$$

$$\Delta_- = \Delta_+ = \frac{\delta m}{m}, \tag{5.24}$$

$$g_0 = g_- = g_+ = 2, \tag{5.25}$$

where δm denotes a mass splitting in $\mathrm{SU}(2)_L$ triplet of spin-1/2. The explicit forms of $g_{\rm eff}$ and r_i are shown below.

$$g_{\rm eff}(x) = 2 + 4\left(1 + \frac{\delta m}{m}\right)^{\frac{3}{2}} \exp\left[-x\frac{\delta m}{m}\right], \tag{5.26}$$

$$r_0(x) = \frac{2}{g_{\rm eff}(x)}, \tag{5.27}$$

$$r_-(x) = r_+(x) = \frac{2(1+\frac{\delta m}{m})^{\frac{3}{2}} \exp\left[-x\frac{\delta m}{m}\right]}{g_{\rm eff}(x)}, \tag{5.28}$$

which all depend on the temperature through the x dependence.

We show the plots of $g_{\rm eff}(x)$, $r_0(x)$, and $r_\pm(x)$ in Fig. 20. The black solid, red dashed, and blue dot-dashed curves show $g_{\rm eff}$, r_0, and $r_\pm$, respectively. From this figure, we read out the following behavior.

[21] In Sec. 4.3, we use the label of two-body state, a, to express each partial wave mode of σv. In this section, we explicitly show labels of component fields, Q, and J. See Eq. (5.29).

- For $T \gg \delta m$ ($x \ll 1/\Delta_\pm$), all the components participate in the annihilation processes. Therefore, we have $r_i \simeq 1/3$ ($i = 0, \pm$) for all the component fields and $g_{\rm eff} \simeq 6$.
- For $T \simeq \delta m$ ($x \simeq 1/\Delta_\pm$), the number density of charged components, $\chi^\pm$, is suppressed compared with that of neutral components, χ^0. This fact is reflected in $r_\pm$ as the exponential suppression. The effective degree of freedom drops to $g_{\rm eff} \simeq 2$ due to the decoupling of the charged components.
- For $T \ll \delta m$ ($x \gg 1/\Delta_\pm$), we have $r_0 \simeq 1$, $r_\pm \simeq 0$ and $g_{\rm eff} \simeq 2$.

Since we have the conservation of (Q, J), $\sigma_{ij}v$ is divided into the following partial contributions.

$$\sigma_{ij}v = \sum_{Q=0,1,2} \sum_{J=0,1} (\sigma_{ij}v)^{Q,J}. \tag{5.29}$$

At the tree-level, we obtain the following results.

$$(\sigma_{00}v)^{Q=0,J=0} = 2\frac{\pi\alpha_2^2}{m^2}, \tag{5.30}$$

$$(\sigma_{-+}v)^{Q=0,J=0} = (\sigma_{+-}v)^{Q=0,J=0} = \frac{3}{2}\frac{\pi\alpha_2^2}{m^2}, \tag{5.31}$$

$$(\sigma_{-+}v)^{Q=0,J=1} = (\sigma_{+-}v)^{Q=0,J=1} = 3 \cdot \frac{25}{24}\frac{\pi\alpha_2^2}{m^2}, \tag{5.32}$$

$$(\sigma_{\mp 0}v)^{Q=1,J=0} = (\sigma_{0\pm}v)^{Q=1,J=0} = \frac{1}{2}\frac{\pi\alpha_2^2}{m^2}, \tag{5.33}$$

$$(\sigma_{\mp 0}v)^{Q=1,J=1} = (\sigma_{0\pm}v)^{Q=1,J=1} = 3 \cdot \frac{25}{24}\frac{\pi\alpha_2^2}{m^2}, \tag{5.34}$$

$$(\sigma_{--}v)^{Q=2,J=0} = (\sigma_{++}v)^{Q=2,J=0} = \frac{\pi\alpha_2^2}{m^2}. \tag{5.35}$$

The above cross sections are related to the imaginary part of the two-body potential through matching. We multiply the factor of two for $\sigma_{ii}v$ where initial states are composed of two identical particles. The factors of three for $J = 1$ mode come from the summation over $J_z = 0, \pm 1$.

These tree-level expressions are modified due to the NR potential force by the Sommerfeld

factors.

$$(\sigma_{00}v)^{Q=0,J=0} = \frac{\pi\alpha_2^2}{m^2} D_{00}(E), \tag{5.36}$$

$$(\sigma_{-+}v)^{Q=0,J=0} = (\sigma_{+-}v)^{Q=0,J=0} = \frac{\pi\alpha_2^2}{2m^2} D_{-+}(E), \tag{5.37}$$

$$(\sigma_{-+}v)^{Q=0,J=1} = (\sigma_{+-}v)^{Q=0,J=1} = 3 \cdot \frac{25}{24}\frac{\pi\alpha_2^2}{m^2} |d^{(Q=0,J=1)}|^2, \tag{5.38}$$

$$(\sigma_{\mp 0}v)^{Q=1,J=0} = (\sigma_{0\mp}v)^{Q=1,J=0} = \frac{1}{2}\frac{\pi\alpha_2^2}{m^2} |d^{(Q=1,J=0)}|^2, \tag{5.39}$$

$$(\sigma_{\mp 0}v)^{Q=1,J=1} = (\sigma_{0\mp}v)^{Q=1,J=1} = 3 \cdot \frac{25}{24}\frac{\pi\alpha_2^2}{m^2} |d^{(Q=1,J=1)}|^2, \tag{5.40}$$

$$(\sigma_{--}v)^{Q=2,J=0} = (\sigma_{++}v)^{Q=2,J=0} = \frac{\pi\alpha_2^2}{m^2} |d^{(Q=2,J=0)}|^2. \tag{5.41}$$

We define the following functions to express the Sommerfeld factors for $Q = 0, J = 0$ modes where the Schrödinger equation is expected in a two-by-two matrix form.

$$D_{00}(E) \equiv 3|d^{(Q=0,J=0)}_{00,-+}|^2 + \sqrt{2} d^{(Q=0,J=0)}_{00,-+} d^{*(Q=0,J=0)}_{00,00} + \sqrt{2} d^{(Q=0,J=0)}_{00,00} d^{*(Q=0,J=0)}_{00,-+} + 2|d^{(Q=0,J=0)}_{00,00}|^2, \tag{5.42}$$

$$D_{-+}(E) \equiv 3|d^{(Q=0,J=0)}_{-+,-+}|^2 + \sqrt{2} d^{(Q=0,J=0)}_{-+,-+} d^{*(Q=0,J=0)}_{-+,00} + \sqrt{2} d^{(Q=0,J=0)}_{-+,00} d^{*(Q=0,J=0)}_{-+,-+} + 2|d^{(Q=0,J=0)}_{-+,00}|^2. \tag{5.43}$$

For the other modes, we simply attached the squared factor of the Sommerfeld factors where labels of the component fields are implicit. In the relativistic limit, $v_{ij} \to 1$, we have the following converged values for each factor.

$$D_{00}(E) \to 2, \qquad \text{(for } Q = 0, J = 0 \text{ with } \chi^0\chi^0 \text{ initial state)} \tag{5.44}$$

$$D_{-+}(E) \to 3, \qquad \text{(for } Q = 0, J = 0 \text{ with } \chi^-\chi^+ \text{ initial state)} \tag{5.45}$$

$$|d^{(Q,J)}|^2(E) \to 1, \qquad \text{(otherwise)} \tag{5.46}$$

and thus we reproduce the tree-level results shown in Eqs. (5.30)-(5.35).

The Sommerfeld factors and the effective cross sections are calculated numerically as a function of x. We use the mathematica module to solve the differential equations. In Fig. 21, we show the Sommerfeld factors for each partial wave mode. We take $m = 2.8$ TeV and $\delta m = 170$ MeV as benchmark values. We consider the scattering process, $\chi^i\chi^j \to \chi^k\chi^\ell$, and express these factors as the function of relative velocity between initial two particles, $v \equiv v_{ij}$. For $(Q, J) = (0, 0)$ mode, we show $D_{00}(E)$ and $D_{-+}(E)$ in the left and right panels in the first row, respectively. For the other modes, we plot the squared Sommerfeld factors. The converged values are shown as the horizontal dashed black lines in each plot. In the plot of

$\chi^0\chi^0$, we have the singular behavior for $D_{00}(E)$ around $v \simeq \sqrt{8\delta m/m}$. This is because the charged states are not achievable kinematically if the mass splitting is larger than the kinetic energy. This value is shown as the black vertical dashed line. We have the repulsive potential for the state with $Q = 2, J = 0$, and thus the Sommerfeld factor gives suppression for $v \ll 1$.

In Fig. 22, we show the effective cross section in the Wino DM system. We show the perturbative result in the top panel and show the result in the Sommerfeld effect in the center panel. The black curves show $\langle \sigma_{\rm eff} v \rangle$ in each panel. The orange dashed and red dot-dashed curves show the partial contributions of $(Q, J) = (0, 0)_{\chi^0\chi^0}$ and $(0, 0)_{\chi^-\chi^+}$, respectively.[22] The red dashed curve shows $(Q, J) = (0, 1)$ contribution. The blue dashed, blue dot-dashed, and green dashed curves show the contributions from states with $(Q, J) = (1, 0), (1, 1)$, and $(2, 0)$, respectively. After the decoupling of the charged components, $x \gtrsim 1/\Delta_\pm$, $\langle \sigma_{\rm eff} v \rangle$ converges to the value of $(Q, J) = (0, 0)_{\chi^0\chi^0}$ mode. In the bottom panel, we show the comparison of results without and with Sommerfeld effects. The green dashed curve shows the perturbative result and the red dot-dashed curve shows the result including the Sommerfeld effect. We find a large discrepancy between these two results for the NR region $m/T \gg 1$ where the potential force effectively affects the DM annihilation.

5.3.2 Effective annihilation cross section for non-abelian vector DM

In the $\mathrm{SU}(2)_L$ triplet spin-1 system, we have

$$\Delta_0 = 0, \tag{5.47}$$

$$\Delta_- = \Delta_+ = \frac{\delta m_V}{m_V}, \tag{5.48}$$

$$g_0 = g_- = g_+ = 3. \tag{5.49}$$

The explicit forms of $g_{\rm eff}$ and r_i are shown below.

$$g_{\rm eff}(x) = 3 + 6\left(1 + \frac{\delta m_V}{m_V}\right)^{\frac{3}{2}} \exp\left[-x\frac{\delta m_V}{m_V}\right], \tag{5.50}$$

$$r_0(x) = \frac{3}{g_{\rm eff}(x)}, \tag{5.51}$$

$$r_-(x) = r_+(x) = \frac{3(1 + \frac{\delta m_V}{m_V})^{\frac{3}{2}} \exp\left[-x\frac{\delta m_V}{m_V}\right]}{g_{\rm eff}(x)}. \tag{5.52}$$

We show the plots of $g_{\rm eff}(x)$, $r_0(x)$, and $r_\pm(x)$ in Fig. 23. The black solid, red dashed, and blue dot-dashed curves show $g_{\rm eff}$, r_0, and $r_\pm$, respectively. In this vector DM case, we have $g_{\rm eff} \simeq 3$ for $x \gg 1$.

We decompose the cross section into partial modes.

$$\sigma_{ij} v = \sum_{Q=0,1,2} \sum_{J=0,1,2} (\sigma_{ij} v)^{Q,J}, \tag{5.53}$$

[22] Lower subscription denotes the initial state.

where $i, j = 0, \pm$. At the tree-level, we have the following expressions.

$$(\sigma_{00}v)^{Q=0,J=0} = 2 \cdot (\Gamma_{\rm SM}^{J=0} + \Gamma_{\rm Z'}^{J=0}), \tag{5.54}$$
$$(\sigma_{00}v)^{Q=0,J=2} = 2 \cdot 5 \cdot (\Gamma_{\rm SM}^{J=2} + \Gamma_{\rm Z'}^{J=2}), \tag{5.55}$$

$$(\sigma_{-+}v)^{Q=0,J=0} = (\sigma_{+-}v)^{Q=0,J=0} = (\Gamma_{\rm SM}^{J=0} + \Gamma_{\rm Z'}^{J=0}), \tag{5.56}$$
$$(\sigma_{-+}v)^{Q=0,J=1} = (\sigma_{+-}v)^{Q=0,J=1} = 3 \cdot (\Gamma_{\rm SM}^{J=1} + \Gamma_{\rm Z'}^{J=1}), \tag{5.57}$$
$$(\sigma_{-+}v)^{Q=0,J=2} = (\sigma_{+-}v)^{Q=0,J=2} = 5 \cdot (\Gamma_{\rm SM}^{J=2} + \Gamma_{\rm Z'}^{J=2}), \tag{5.58}$$

$$(\sigma_{\mp 0}v)^{Q=1,J=0} = (\sigma_{0\mp}v)^{Q=1,J=0} = (\Gamma_{\rm SM}^{J=0} + \Gamma_{\rm Z'}^{J=0}), \tag{5.59}$$
$$(\sigma_{\mp 0}v)^{Q=1,J=1} = (\sigma_{0\mp}v)^{Q=1,J=1} = 3 \cdot (\Gamma_{\rm SM}^{J=0} + \Gamma_{\rm Z'}^{J=0}), \tag{5.60}$$
$$(\sigma_{\mp 0}v)^{Q=1,J=2} = (\sigma_{0\mp}v)^{Q=1,J=2} = 5 \cdot (\Gamma_{\rm SM}^{J=2} + \Gamma_{\rm Z'}^{J=2}), \tag{5.61}$$

$$(\sigma_{--}v)^{Q=2,J=0} = (\sigma_{++}v)^{Q=2,J=0} = 2 \cdot (\Gamma_{\rm SM}^{J=0} + \Gamma_{\rm Z'}^{J=0}), \tag{5.62}$$
$$(\sigma_{--}v)^{Q=2,J=2} = (\sigma_{++}v)^{Q=2,J=2} = 2 \cdot 5 \cdot (\Gamma_{\rm SM}^{J=2} + \Gamma_{\rm Z'}^{J=2}), \tag{5.63}$$

We multiply the factor of two for $\sigma_{ii}v$. The factors of five for $J = 2$ contributions come from the summation over $J_z = 0, \pm 1, \pm 2$.

Including the Sommerfeld effect, we have to attach the Sommerfeld factors for each annihilation mode.

$$(\sigma_{00}v)^{Q=0,J=0} = 2 \cdot (\Gamma_{\rm SM}^{J=0} + \Gamma_{\rm Z'}^{J=0}) D_{00}^{J=0}(E), \tag{5.64}$$
$$(\sigma_{00}v)^{Q=0,J=2} = 2 \cdot 5 \cdot (\Gamma_{\rm SM}^{J=2} + \Gamma_{\rm Z'}^{J=2}) D_{-+}^{J=2}(E), \tag{5.65}$$

$$(\sigma_{-+}v)^{Q=0,J=0} = (\sigma_{+-}v)^{Q=0,J=0} = (\Gamma_{\rm SM}^{J=0} + \Gamma_{\rm Z'}^{J=0}) D_{00}^{J=0}(E), \tag{5.66}$$
$$(\sigma_{-+}v)^{Q=0,J=1} = (\sigma_{+-}v)^{Q=0,J=1} = 3 \cdot (\Gamma_{\rm SM}^{J=1} + \Gamma_{\rm Z'}^{J=1}) D_{-+}^{J=1}(E), \tag{5.67}$$
$$(\sigma_{-+}v)^{Q=0,J=2} = (\sigma_{+-}v)^{Q=0,J=2} = 5 \cdot (\Gamma_{\rm SM}^{J=2} + \Gamma_{\rm Z'}^{J=2}) D_{-+}^{J=2}(E), \tag{5.68}$$

$$(\sigma_{\mp 0}v)^{Q=1,J=0} = (\sigma_{0\mp}v)^{Q=1,J=0} = (\Gamma_{\rm SM}^{J=0} + \Gamma_{\rm Z'}^{J=0}) |d^{(Q=1,J=0)}|^2, \tag{5.69}$$
$$(\sigma_{\mp 0}v)^{Q=1,J=1} = (\sigma_{0\mp}v)^{Q=1,J=1} = 3 \cdot (\Gamma_{\rm SM}^{J=1} + \Gamma_{\rm Z'}^{J=1}) |d^{(Q=1,J=1)}|^2, \tag{5.70}$$
$$(\sigma_{\mp 0}v)^{Q=1,J=2} = (\sigma_{0\mp}v)^{Q=1,J=2} = 5 \cdot (\Gamma_{\rm SM}^{J=2} + \Gamma_{\rm Z'}^{J=2}) |d^{(Q=1,J=2)}|^2, \tag{5.71}$$

$$(\sigma_{--}v)^{Q=2,J=0} = (\sigma_{++}v)^{Q=2,J=0} = 2 \cdot (\Gamma_{\rm SM}^{J=0} + \Gamma_{\rm Z'}^{J=0}) |d^{(Q=2,J=0)}|^2, \tag{5.72}$$
$$(\sigma_{--}v)^{Q=2,J=2} = (\sigma_{++}v)^{Q=2,J=2} = 2 \cdot 5 \cdot (\Gamma_{\rm SM}^{J=2} + \Gamma_{\rm Z'}^{J=2}) |d^{(Q=2,J=2)}|^2, \tag{5.73}$$

where we define the functions $D_{00}^J(E)$ and $D_{-+}^J(E)$ in the same manner as defined in Eqs. (5.42), (5.43) to express the Sommerfeld factors for $Q = 0$ modes.

In Fig. 24, we show the Sommerfeld factors for each partial wave mode. We consider the scattering processes, $V^iV^j \to V^kV^\ell$, as the function of relative velocity for the initial two-body state $v \equiv v_{ij}$. We take $m_V = 2.8$ TeV, $\delta m_V = 170$ MeV, and $m_{Z'} = 1.5\ m_V$ as benchmark values to compare with spin-1/2 result. The left column shows the results for $J = 0$ mode, and the right column shows the results for $J = 2$ mode. We have almost the same plots for $J = 0, 1, 2$. For $Q = 0$ and $Q = 2$ modes, we have the same real part of the potential both in the Wino system and the vector DM system, and thus we obtain almost the same Sommerfeld factors. For $Q = 1$ mode, on the other hand, we obtain the opposite sign compared with the potential of the Wino DM system. Consequently, we have the repulsive potential not only for $Q = 2$ but also for $Q = 1$ modes. For these cases, the Sommerfeld factor gives suppression in the NR region.

In Fig. 25, we show $\langle \sigma_{\rm eff} v \rangle$ with and without the Sommerfeld factors in the vector DM system. We show the tree-level result in the top panel and show the result with the Sommerfeld effect in the center panel. The black curves show $\langle \sigma_{\rm eff} v \rangle$ in each panel. The orange dashed, orange dot-dashed, red dashed, and red dot-dashed curves show the partial contributions from $(Q, J) = (0, 0)_{V^0V^0},\ (0, 2)_{V^0V^0},\ (0, 0)_{V^-V^+},$ and $(0, 2)_{V^-V^+}$ respectively. The blue dashed, blue dot-dashed, green dashed, and green dot-dashed curves show the partial contributions from $(Q, J) = (1, 0), (1, 2), (2, 0),$ and $(2, 2)$, respectively. After the decoupling of the charged components, $x \simeq 1/\Delta_\pm$, $\langle \sigma_{\rm eff} v \rangle$ converges to partial cross contribution from V^0V^0 annihilation cross section. In the bottom panel, we show the comparison of the results without and with the Sommerfeld effect. The green dashed curve shows the perturbative result without the Sommerfeld factor and the red dot-dashed curve shows the result including the Sommerfeld factor.

The thermal relic abundance of DM is derived from the current value of the yield.

$$\Omega_{\rm DM} \equiv \frac{m_V Y_{\rm DM}(T_0)}{\rho_c}, \tag{5.74}$$

where ρ_c is the critical density of the universe, which is taken from Ref. [39], and T_0 is the temperature of the current universe determined in the CMB observations [40].

$$\rho_c = 1.05368 \times 10^{-5} h^2\ {\rm GeV} \cdot {\rm cm}^{-3}, \tag{5.75}$$

$$T_0 = 2.7255 \pm 0.0006\ {\rm K}, \tag{5.76}$$

where h is the Hubble parameter.

We numerically evaluate the value of $Y_{\rm DM}(T_0)$ by solving the Boltzmann equation. In Fig. 27, we compare the predicted value of Ωh^2 in $\mathrm{SU}(2)_L$ triplet spin-1/2 and spin-1 DM system. The green and red lines show the result without and with the Sommerfeld effects. The dashed lines show the result for the Wino DM (spin-1/2) and the solid lines for Vector DM (spin-1). The darker (lighter) gray regions show the value of Ωh^2 in the $1\sigma(2\sigma)$ level determined in the Planck observation [5].

The predicted value of Ωh^2 depends on DM spin mainly for the following two reasons: First, the potential for $Q = 1$ two-body states have opposite signs between the spin-1/2 DM and the spin-1 DM system. The spin-1/2 DM system has the attractive potential and

Table 10: The DM masses to realize the correct value of Ωh^2 for each DM system.

Wino DM (spin-1/2)	Vector DM (spin-1)	
3.1 TeV	6.4 TeV	$(m_{Z'}/m_V = 1.25)$
	4.6 TeV	$(m_{Z'}/m_V = 1.5)$
	3.8 TeV	$(m_{Z'}/m_V = 1.75)$
	3.4 TeV	$(m_{Z'}/m_V = 2.5)$

the Sommerfeld effects turn out to enhance the cross section. In the non relativistic region, $v_{\rm rel} \ll 1$, the Sommerfeld factor converges to $|d|^2 \simeq \mathcal{O}(10)$ as shown in Fig. 21. The spin-1 DM system has the repulsive potential, which causes suppression. The Sommerfeld factor, therefore, converges to $|d|^2 \simeq 0.1$ for $v_{\rm rel} \ll 1$ with $m_{Z'}/m_V = 1.5$ as shown in Fig. 24. Consequently, in the spin-1 DM system, the $Q = 1$ states are irrelevant in the DM annihilation in the early universe as well as the $Q = 2$ states. Due to this decoupling of the $Q = 1$ states for $x \simeq 1$, the deviation from the tree-level result gets smaller in the spin-1 DM system.

Second, V-particles predict the larger annihilation cross section compared with the Wino DM multiplet. If we compare the annihilation cross section into the same SM particle pair such as $\gamma\gamma$ mode, the cross section of V-particles are larger by 38/9, which realize the larger value of $\langle \sigma_{\rm eff} v \rangle$. Besides, V-particles have new annihilation channels into Z_2-even vectors such as W' and Z' if kinematically allowed. Therefore, the effective cross section for the V-particles strongly depends on the mass ratio $m_{Z'}/m_V$. We show this dependence by taking $m_{Z'}/m_V = 1.25$, 1.5, 1.75, and 2.5 in the upper left, upper right, lower left, and lower right panels of Fig. 27, respectively. We also plot the ratio of Ωh^2 without and with the Sommerfeld effects. The dashed blue and solid blue curves show the result for the Wino DM (spin-1/2) and the Vector DM (spin-1), respectively. This ratio in spin-1 DM is almost independent of the value of $m_{Z'}/m_V$. This is because the $m_{Z'}/m_V$ only change the tree-level annihilation cross section, which is canceled in the ratio of tree-level and result with the Sommerfeld effects. We have numerically checked this fact and show the plot taking $m_{Z'}/m_V = 1.5$.

If DM is a single component, the DM mass is constrained by the observed value in the Planck experiments. The DM masses to realize the correct value of Ωh^2 for each DM system are summarized in Table. 10. Due to the difference in the predicted annihilation cross section, we obtain the finite mass gap between predictions from spin-1/2 DM and spin-1 DM. In particular, the value of $m_{Z'}/m_V$ is crucial parameter to tune the predicted value of Ωh^2. This is because Z' or W' may appear in the final state if kinematically allowed, and we obtain the larger annihilation cross section. Besides, the coupling between V-particles and Z'/W' are enhanced for $m_{Z'}/m_V \simeq 1$ as shown in 19. The viable parameter region is, therefore, separated by 0.3 TeV scale DM, which corresponds to ~ 10 % of TeV scale DM. Therefore, interesting DM mass regions are separately predicted for spin-1/2 and spin-1 DM through the freeze-out mechanism.

One interesting possibility is that we may test this prediction through the monochromatic gamma-ray search in upcoming observations where we may reconstruct the DM mass from the exotic peak location in the gamma-ray energy spectrum. In the current and future gamma-ray observation, we expect the energy resolution is expected to be 10 % for TeV scale DM mass. Therefore, we may separate spin of electroweakly interacting DM through the possible signals in future experiments. We will give a detailed study of this direction in Sec. 6.

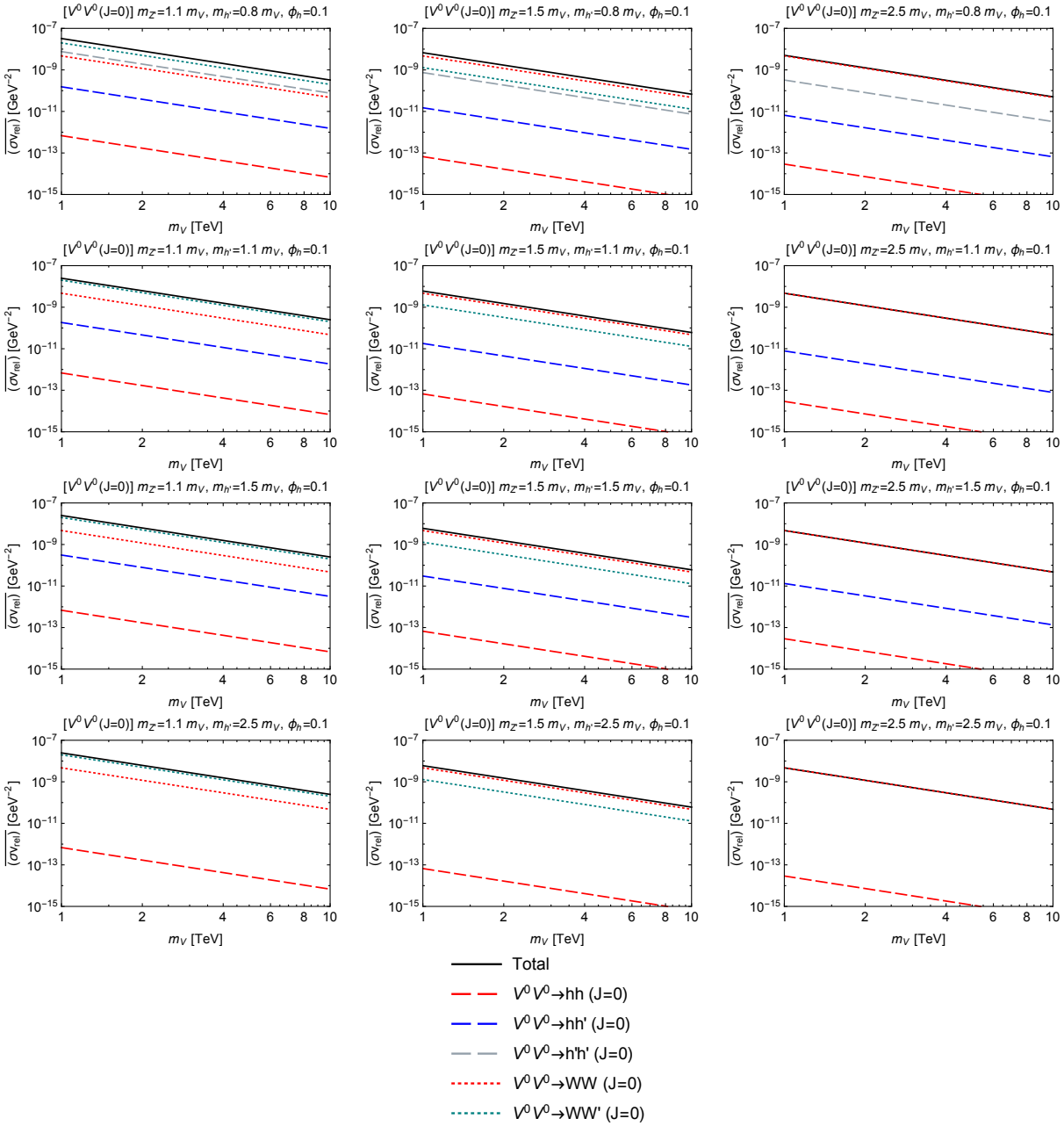

Figure 9: Spin-averaged annihilation cross section of $V^0V^0(J=0)$.

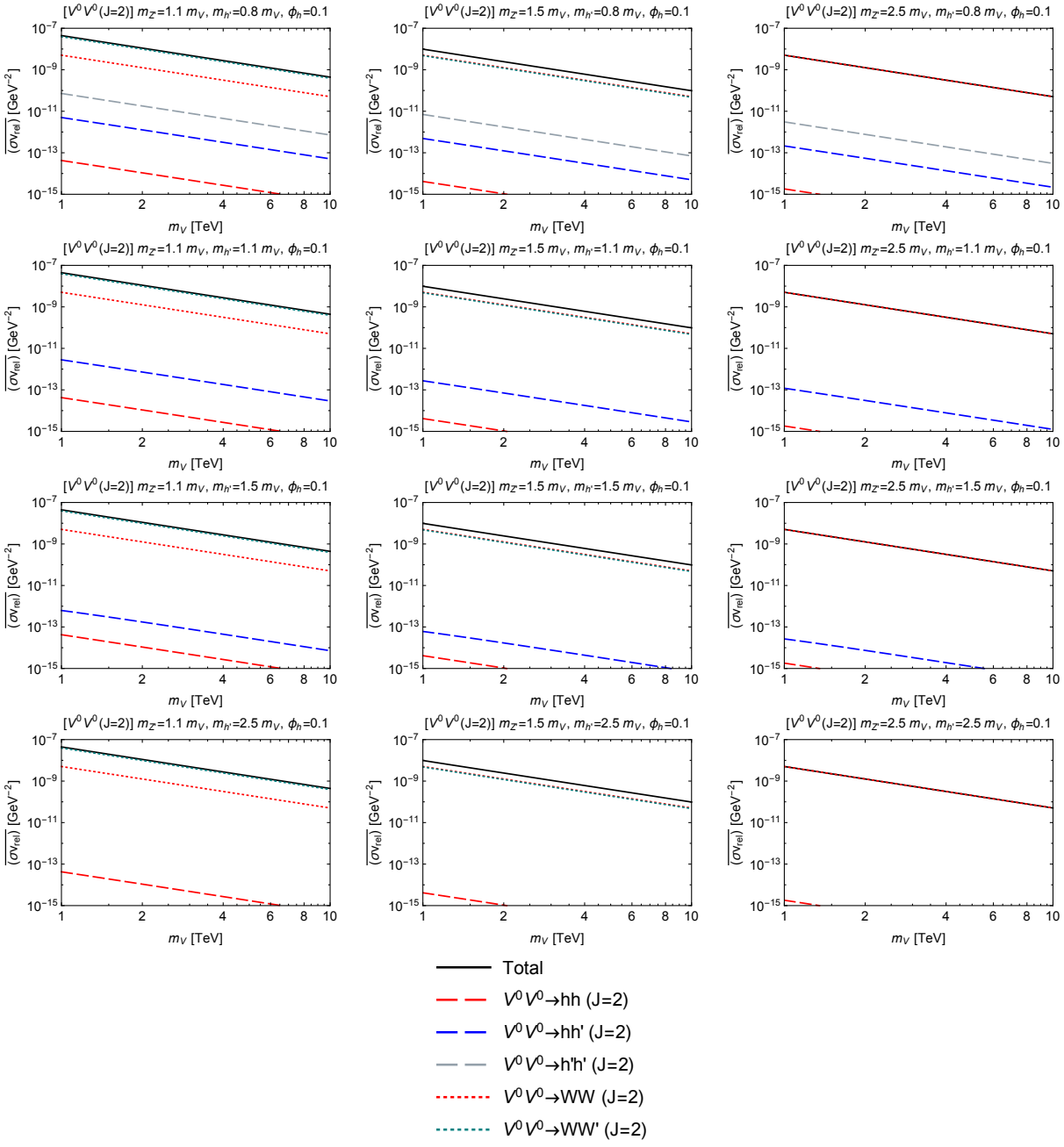

Figure 10: Spin-averaged annihilation cross section of $V^0V^0(J=2)$.

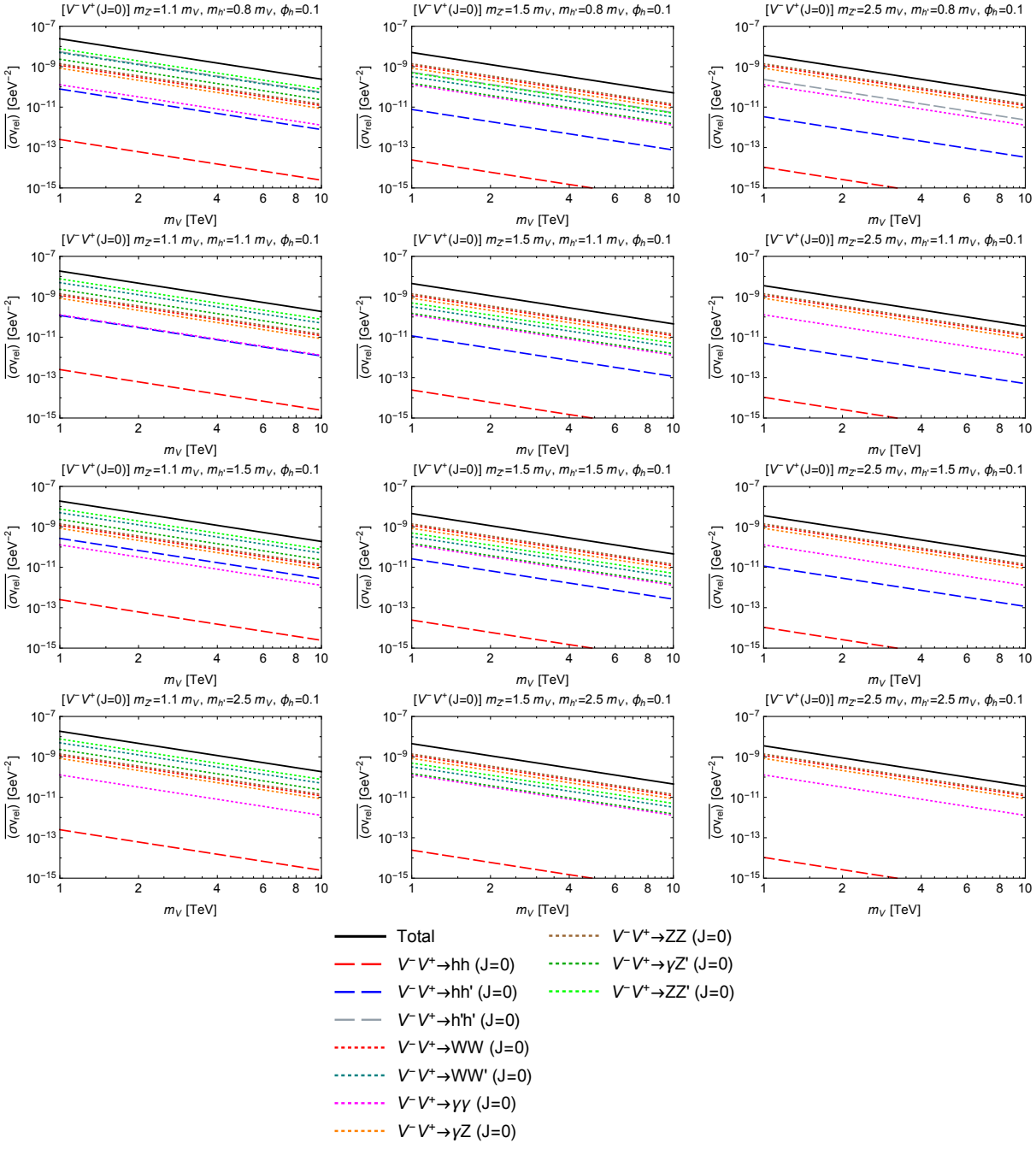

Figure 11: Spin-averaged annihilation cross section of $V^-V^+(J=0)$.

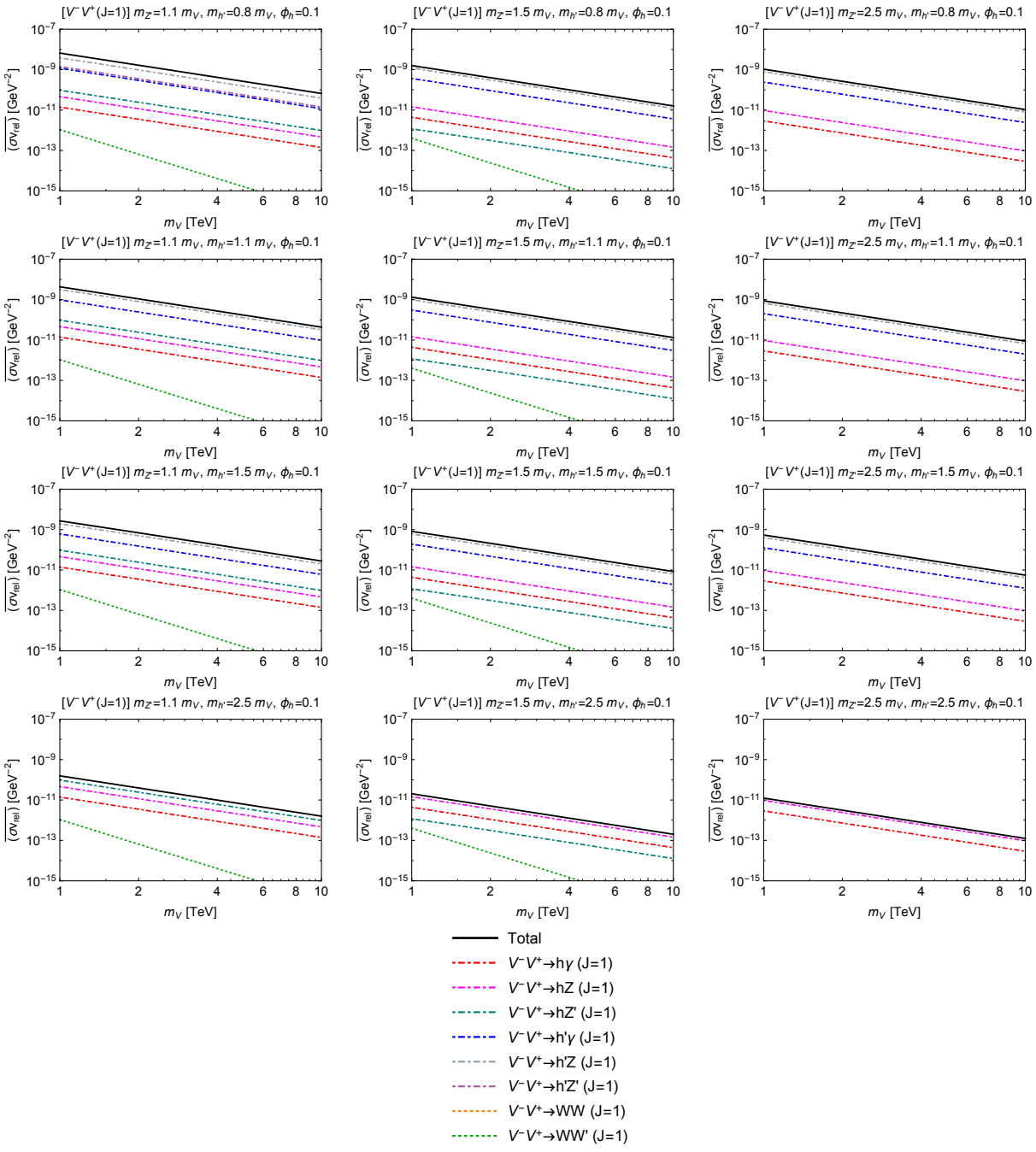

Figure 12: Spin-averaged annihilation cross section of $V^-V^+(J=1)$. The WW mode is irrelevant and does not appear in all the panels.

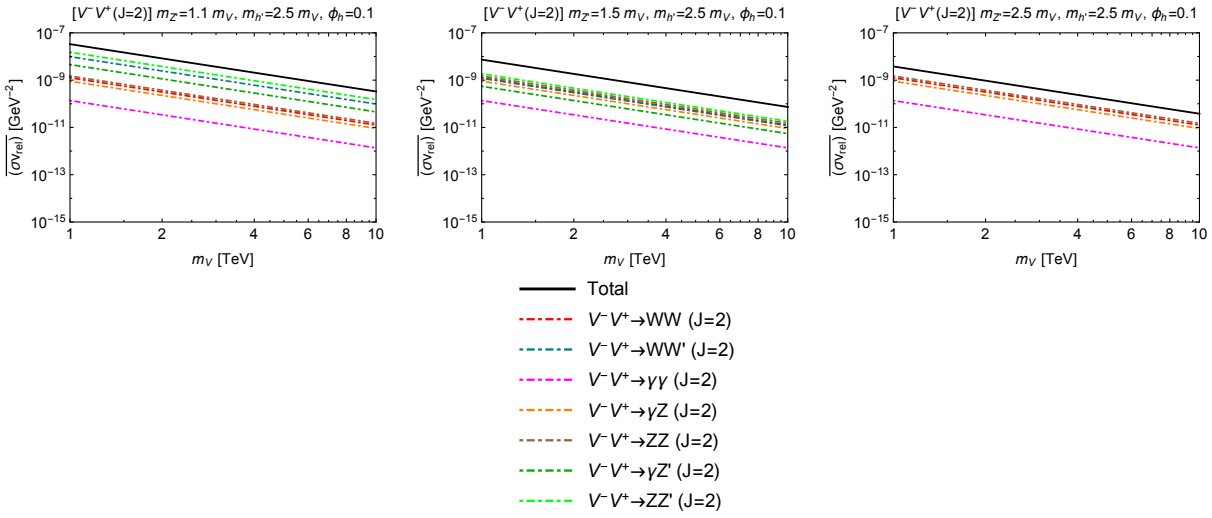

Figure 13: Spin-averaged annihilation cross section of $V^-V^+(J=2)$. All the annihilation modes are independent of $m_{h'}$, and thus we fix $m_{h'} = 2.5m_V$ as a benchmark value.

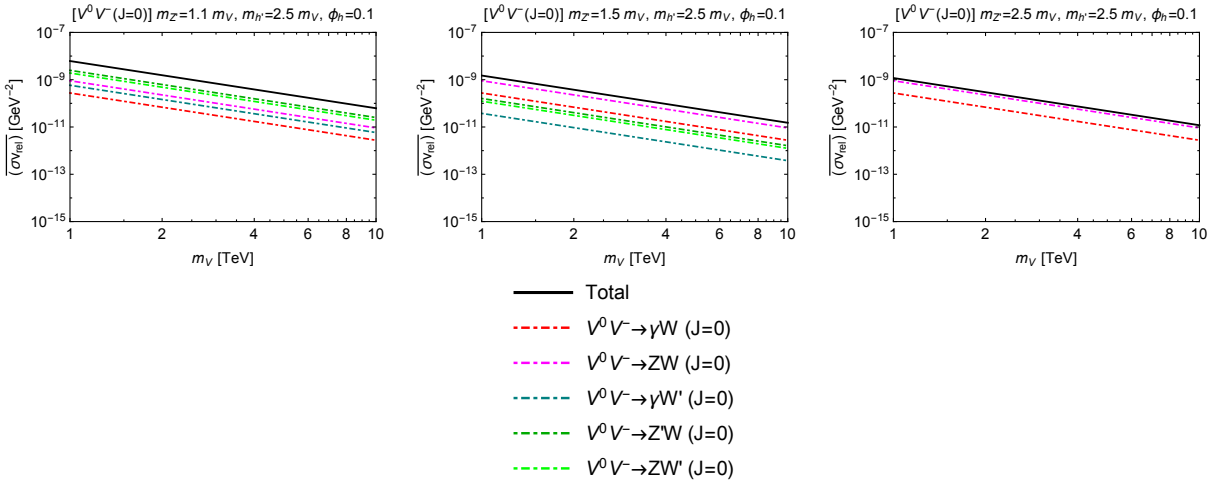

Figure 14: Spin-averaged annihilation cross section of $V^0V^-(J=0)$. All the annihilation modes are independent of $m_{h'}$, and thus we fix $m_{h'} = 2.5m_V$ as a benchmark value.

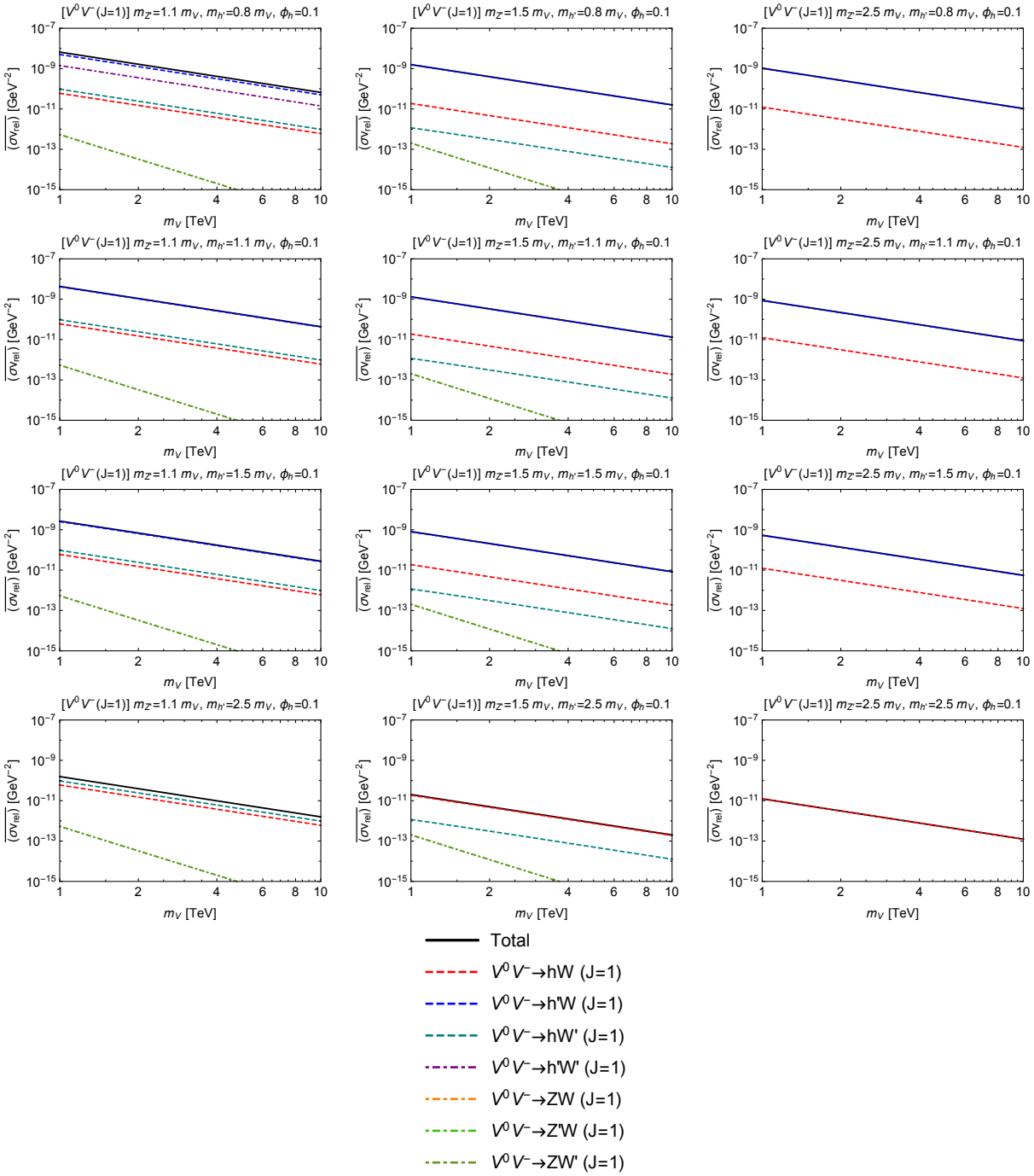

Figure 15: Spin-averaged annihilation cross section of $V^0V^-(J=1)$. The ZW mode is totally irrelevant and does not appear in all the panels.

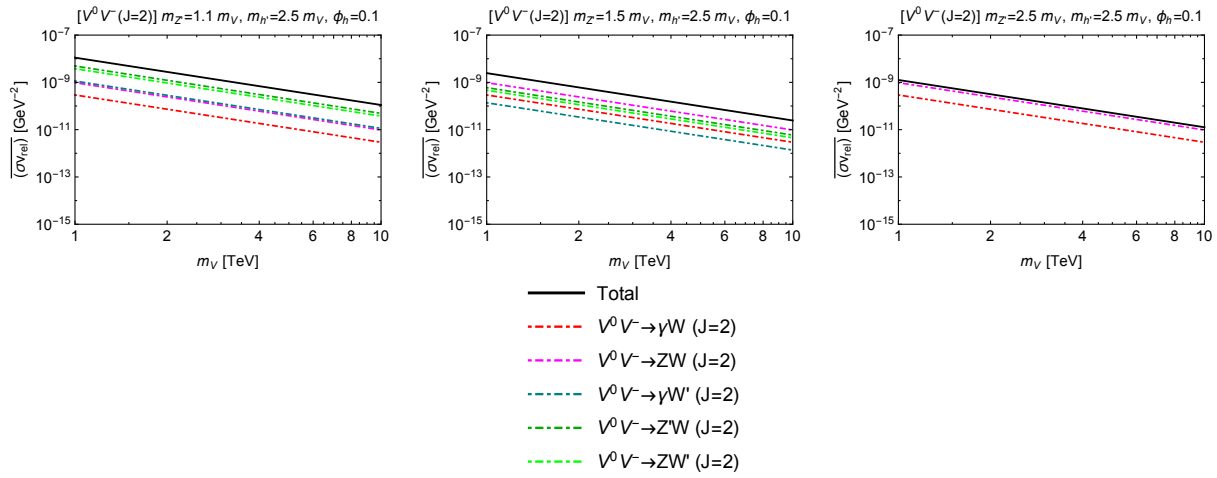

Figure 16: Spin-averaged annihilation cross section of $V^0V^-(J=2)$. All the annihilation modes are independent of $m_{h'}$, and thus we fix $m_{h'} = 2.5m_V$ as a benchmark value.

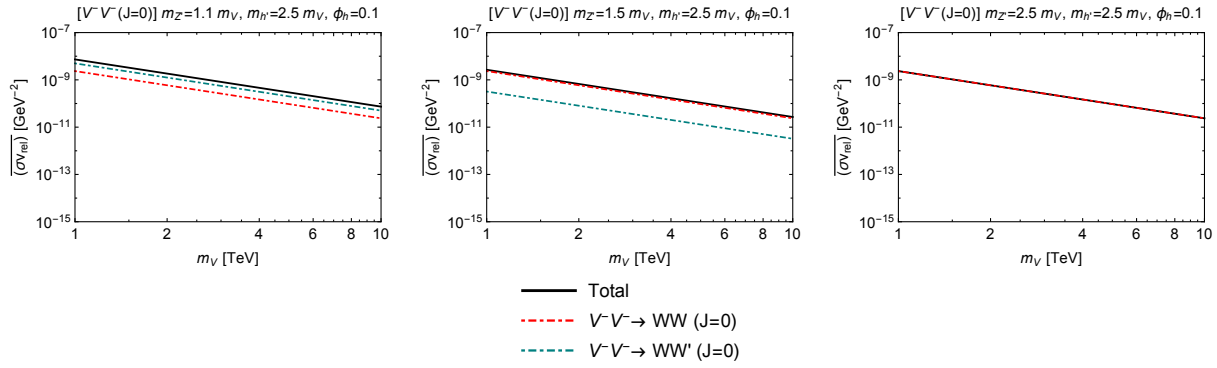

Figure 17: Spin-averaged annihilation cross section of $V^-V^-(J=0)$. All the annihilation modes are independent of $m_{h'}$, and thus we fix $m_{h'} = 2.5m_V$ as a benchmark value.

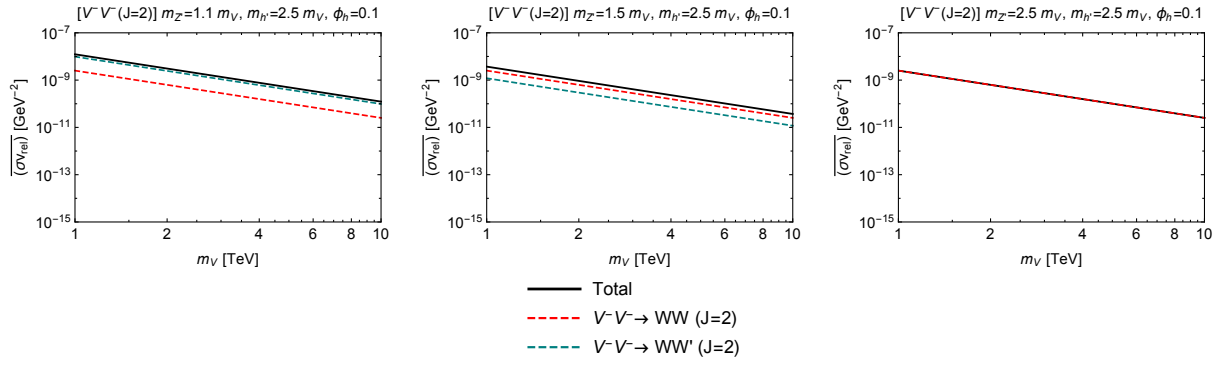

Figure 18: Spin-averaged annihilation cross section of $V^-V^-(J=2)$. All the annihilation modes are independent of $m_{h'}$, and thus we fix $m_{h'} = 2.5m_V$ as a benchmark value.

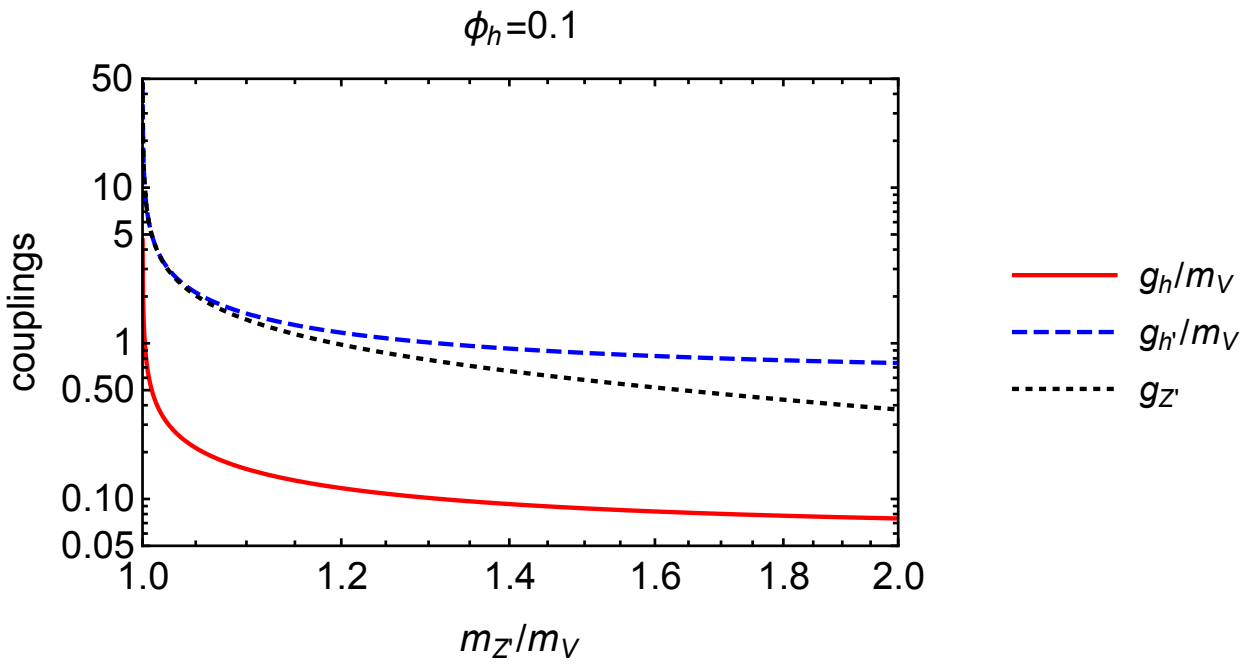

Figure 19: Plots of g_h/m_V, $g_{h'}/m_V$, and $g_{Z'}$ as functions of $m_{Z'}$ which are defined in Sec. 3.3.2. All the couplings are enhanced in the degenerated regions, $m_{Z'}/m_V \simeq 1$.

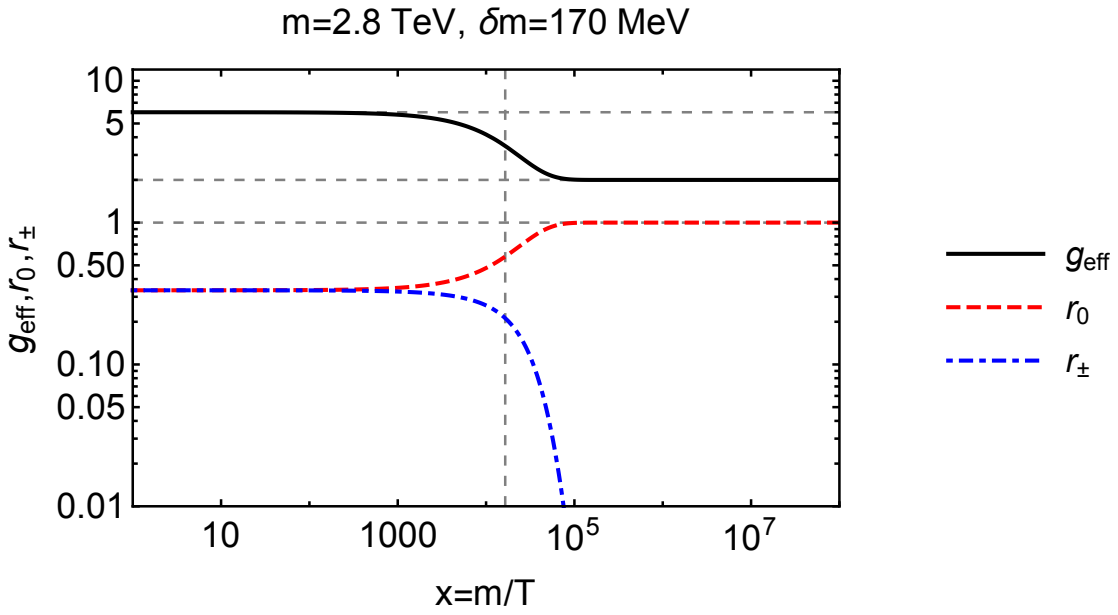

Figure 20: Coannihilation factors for $\mathrm{SU}(2)_L$ triplet spin-1/2 DM system. The black solid, red dashed, and blue dot-dashed curves show $g_{\rm eff}$, r_0, and $r_\pm$, respectively.

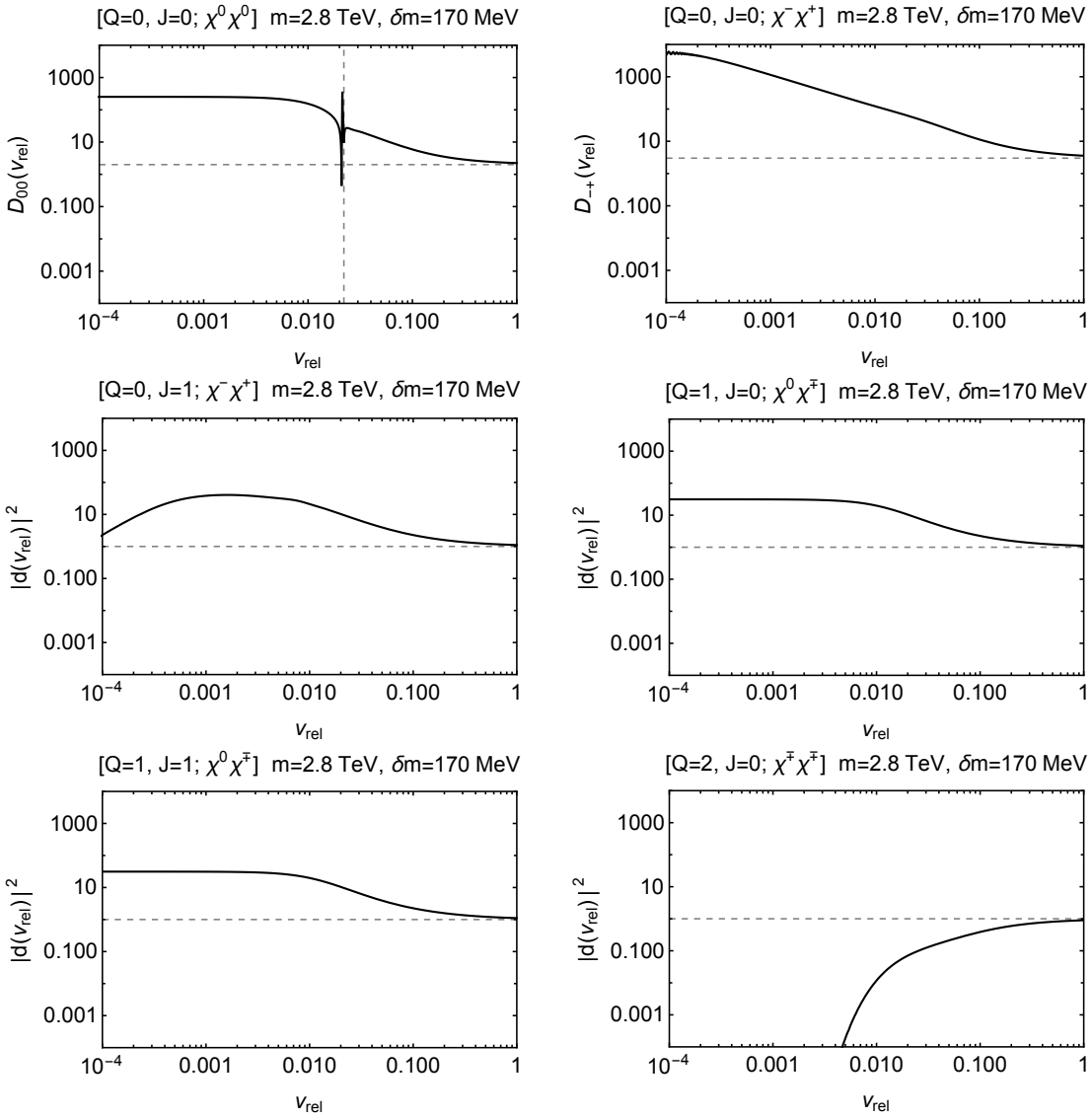

Figure 21: The relative velocity v dependence of the Sommerfeld factors in the Wino DM system. We take $m = 2.8$ TeV and $\delta m = 170$ MeV as benchmark values. These factors are evaluated by solving the Schwinger-Dyson equation for the Green function describing $\chi^i\chi^j \to \chi^k\chi^\ell$ process. Each panel shows the factor for annihilation processes decomposed into partial wave modes where we show $[Q,\, J,\, \chi^i\chi^j]$ on the top of each panel. The converged values are shown as the black horizontal dashed line. The black vertical dashed line in the plot of $[Q = 0,\, J = 0,\, \chi^0\chi^0]$ shows the velocity, $v \simeq \sqrt{8\delta m/m}$, at which the final state with charged components is closed.

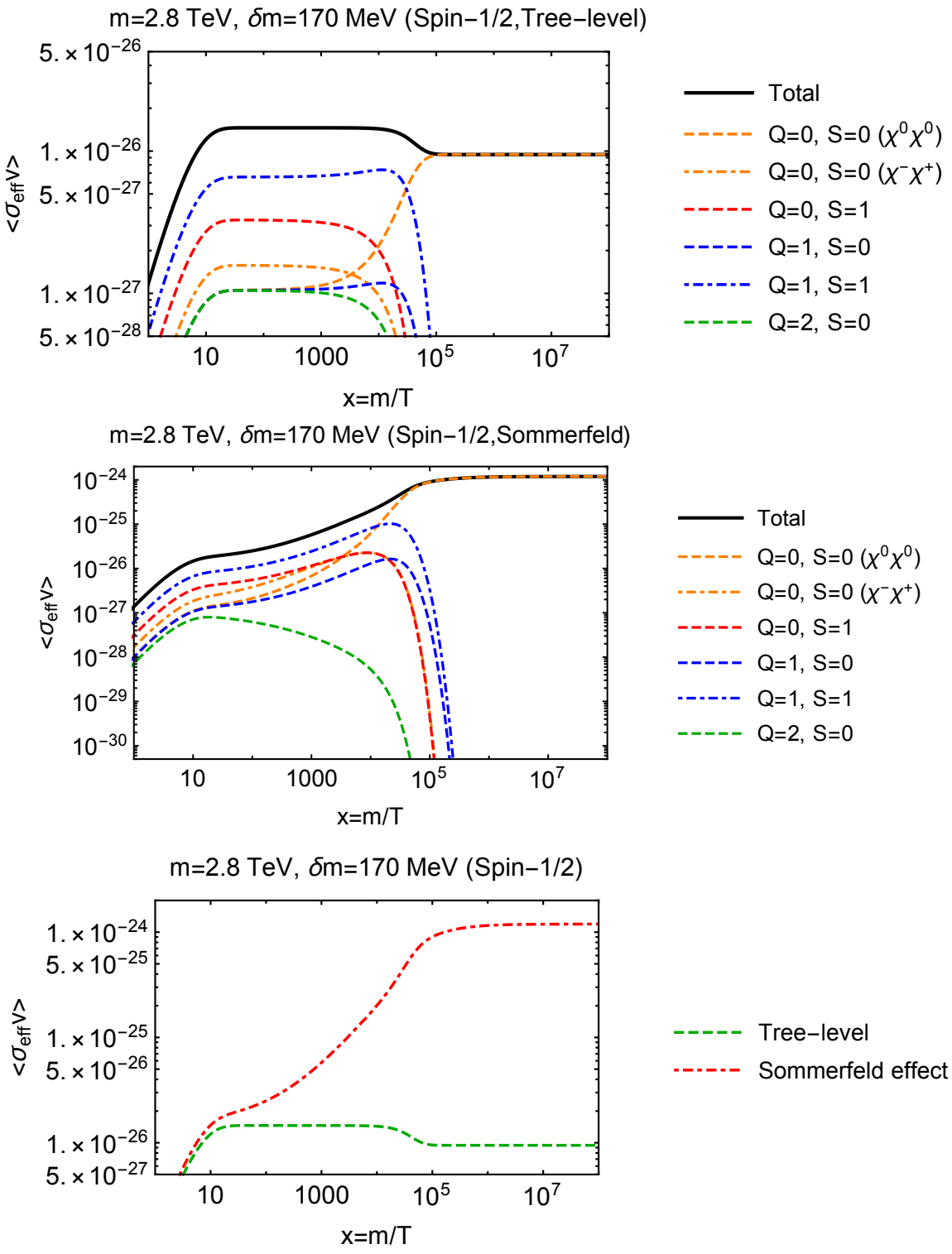

Figure 22: The x dependence of the effective cross section in the Wino system. We show the perturbative result in the top panel and show the result with the Sommerfeld effect in the center panel. We take $m = 2.8$ TeV and $\delta m = 170$ MeV as benchmark values. In the bottom panel, we show the comparison of the results without and with the Sommerfeld effect.

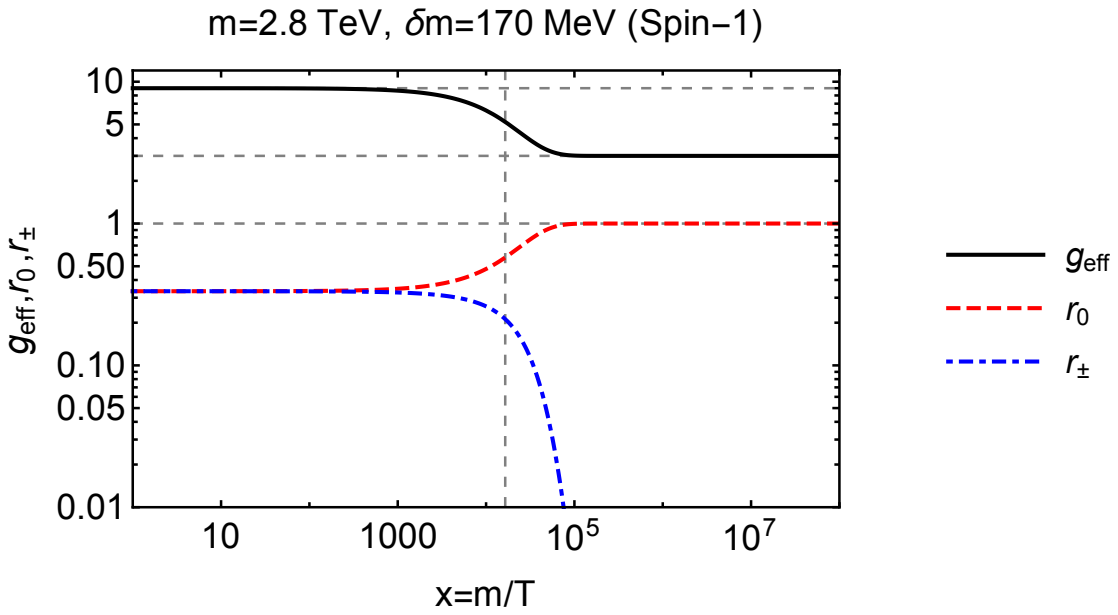

Figure 23: Coannihilation factors for $\mathrm{SU}(2)_L$ triplet spin-1 DM candidate. The black solid, red dashed, and blue dot-dashed curves show $g_{\rm eff}$, r_0, and $r_\pm$, respectively.

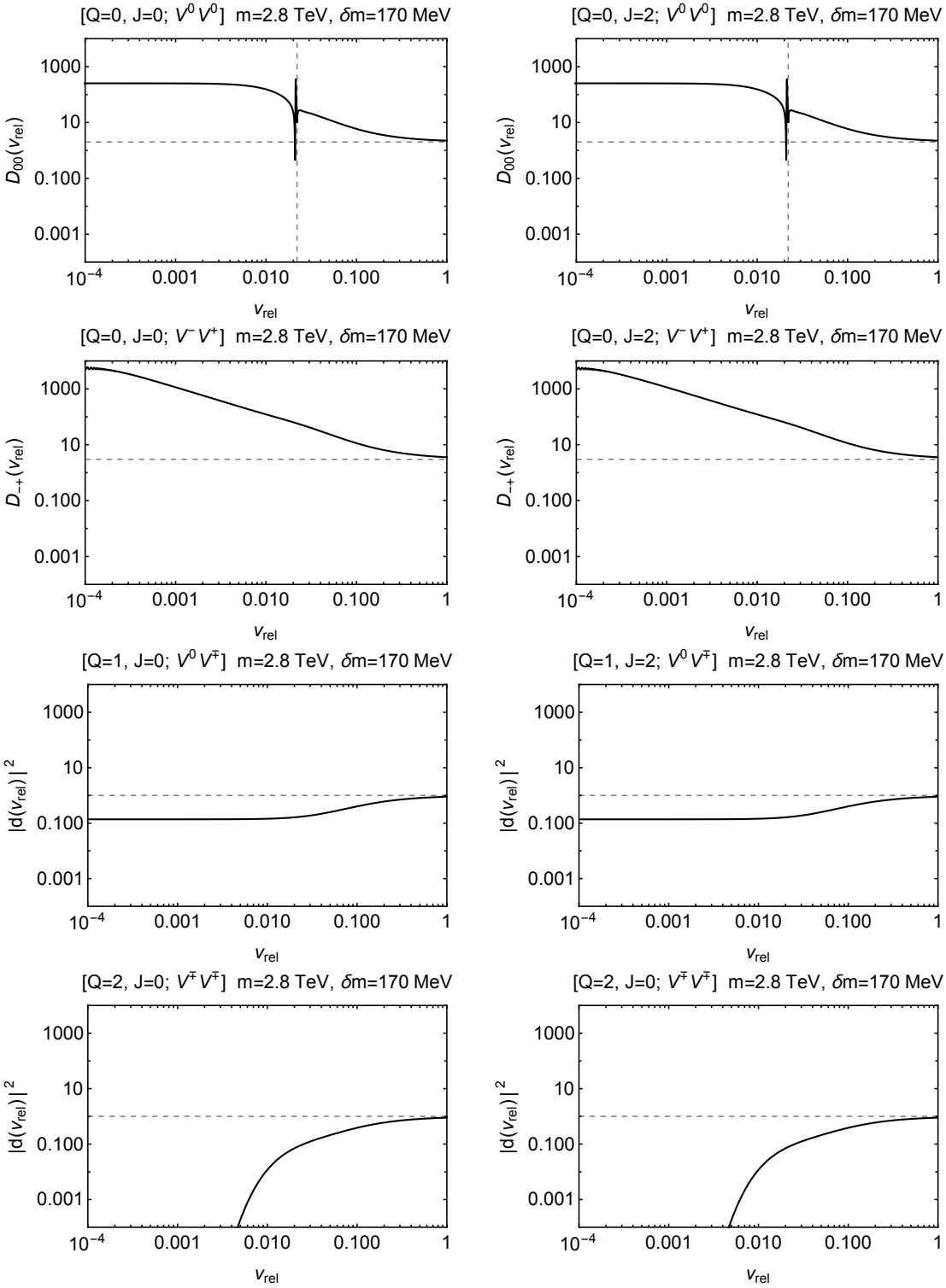

Figure 24: The relative velocity v dependence of the Sommerfeld enhancement factors in the non-abelian vector DM system. We take $m_V = 2.8$ TeV, $\delta m_V = 170$ MeV, and $m_{Z'} = 1.5\, m_V$ as a benchmark value. See the caption of Fig. 21 for details.

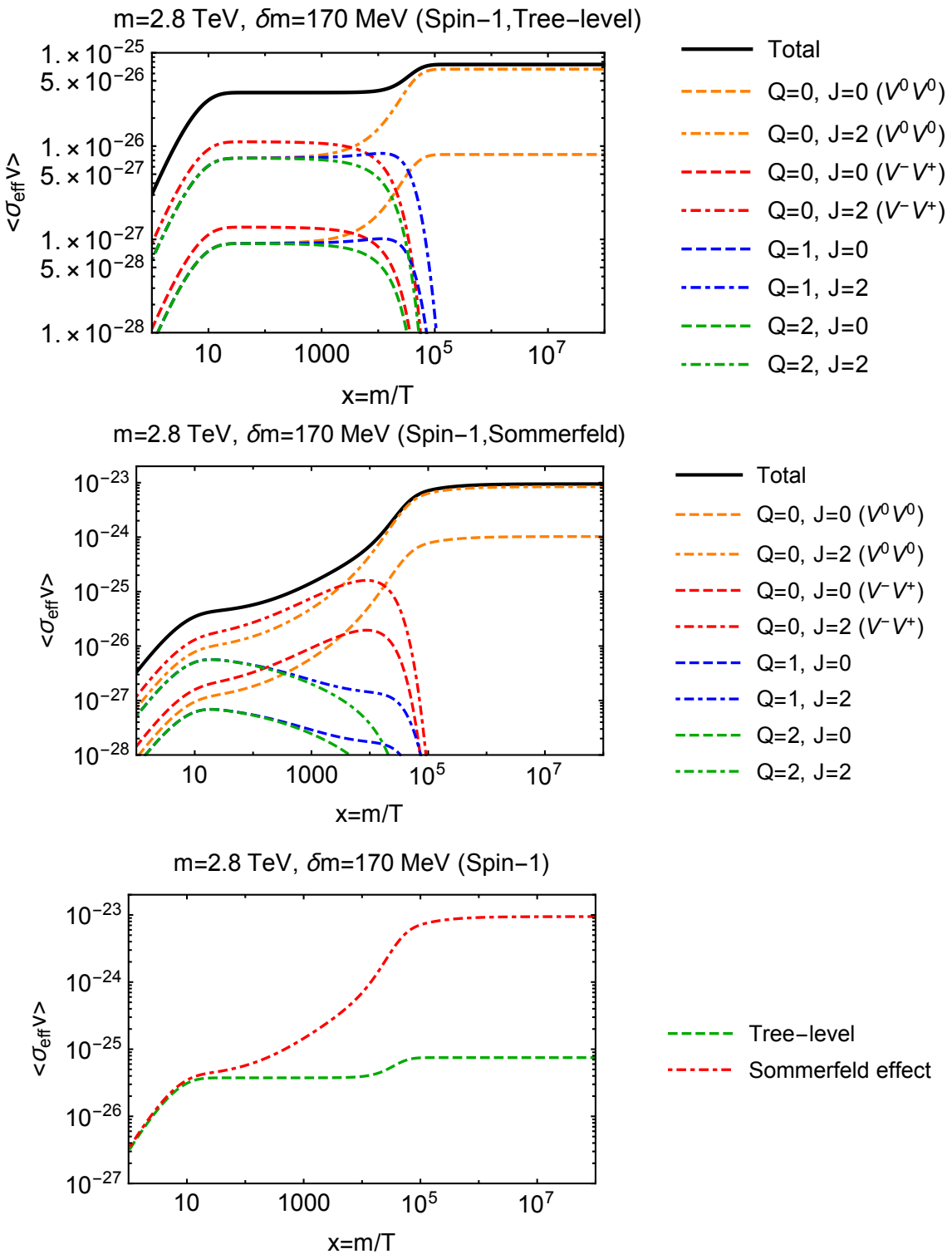

Figure 25: The x dependence of the effective cross section in the vector DM system. We take $m_V = 2.8$ TeV, $\delta m_V = 170$ MeV, and $m_{Z'} = 1.5\ m_V$ as benchmark values to compare with spin-1/2 system. We show the tree-level result in the top panel and show the result with the Sommerfeld effect in the center panel. In the bottom panel, we show the comparison of the results with and without Sommerfeld effect. 91

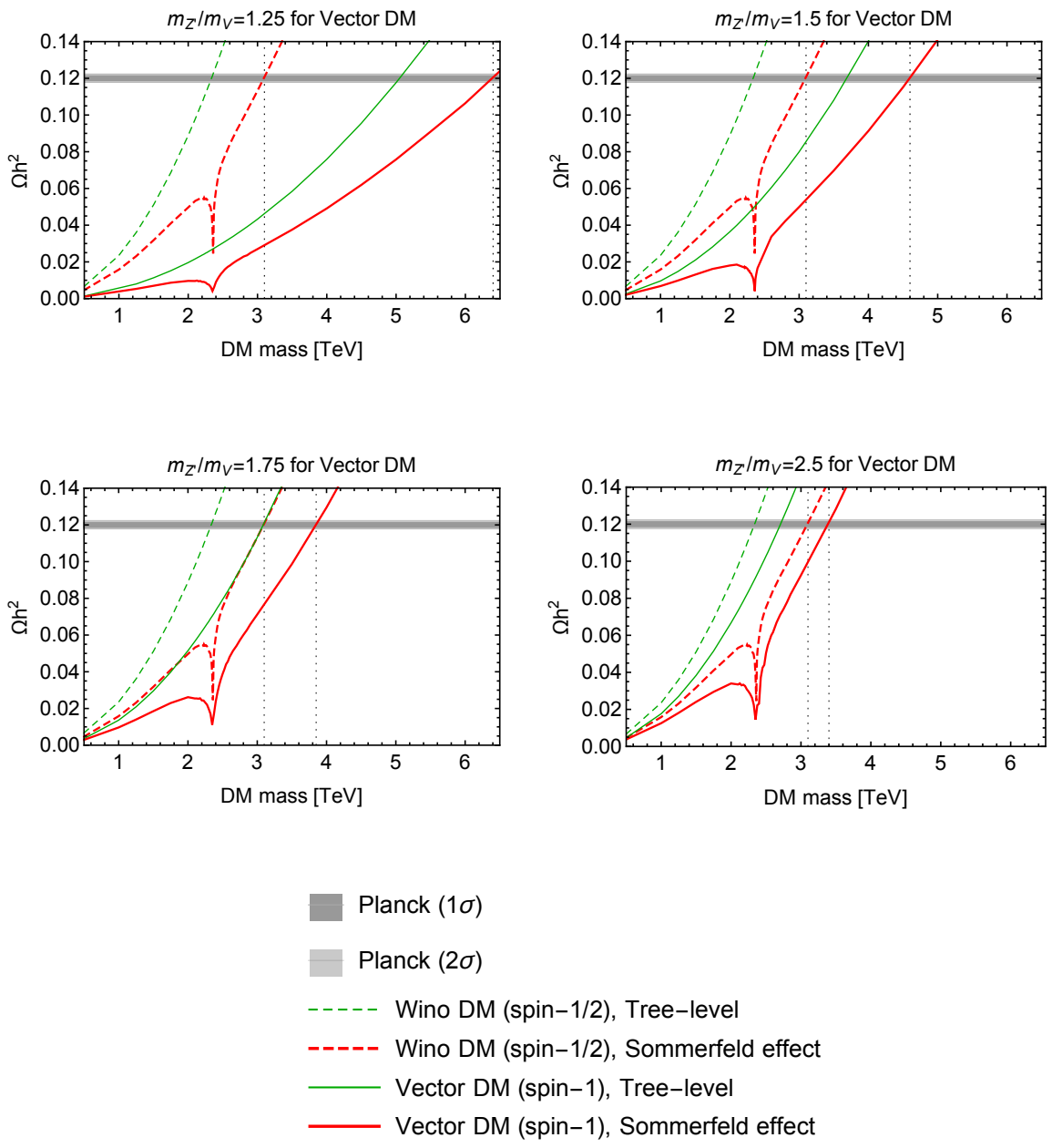

Figure 26: The comparison of DM thermal relic abundance in unit of Ωh^2. The dashed lines show the result for the Wino DM (spin-1/2) and the solid lines for Vector DM (spin-1). The green and red lines show the result without and with the Sommerfeld effects. We take $m_{Z'}/m_V = 1.25, 1.5$, 1.75, and 2.5 in the upper left, upper right, lower left, and lower right panels, respectively.

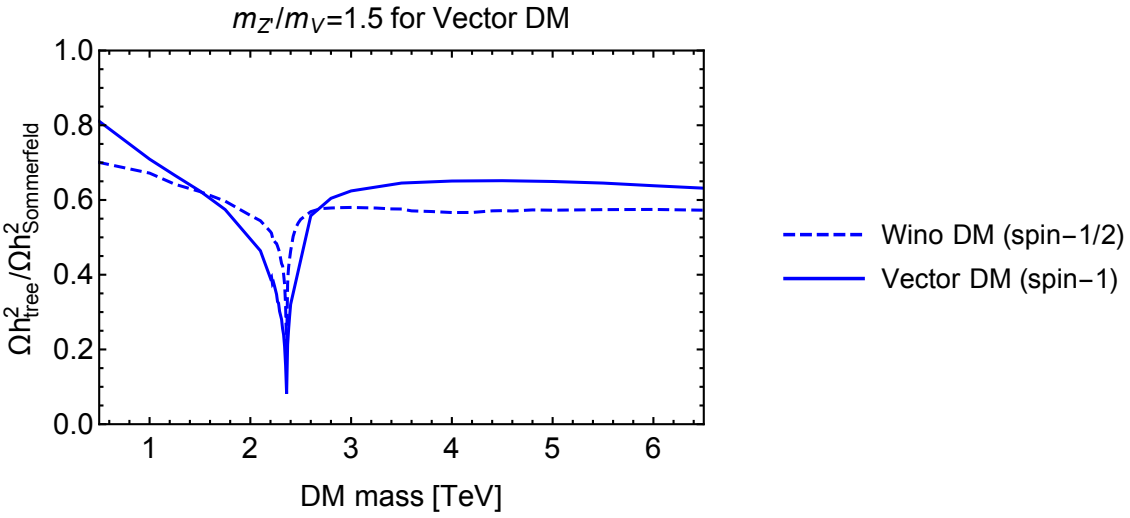

Figure 27: The ratio of Ωh^2 without and with the Sommerfeld effects. The dashed blue and solid blue lines show the results for the Wino DM (spin-1/2) and the Vector DM (spin-1), respectively. The ratio for the spin-1 DM system is almost independent of a value of $m_{Z'}/m_V$, and we take $m_{Z'}/m_V = 1.5$ as a benchmark value.

6 Gamma-ray signatures and DM spin discrimination

We will discuss how to discriminate spin-1/2 and spin-1 DM candidates with $\mathrm{SU}(2)_L$ triplet and $Y = 0$ interactions. In Sec. 6.1, we briefly review the DM indirect detection approach. The monochromatic gamma-ray search is one of the most promising channels to search DM annihilation signatures. We also show the way to derive the experimental constraints on the theoretical prediction of DM annihilation cross section and review current and future observations. In Sec. 6.2, we derive the constraint on the DM annihilation line cross section in light of the current experimental data. We also reveal the parameter region that will be tested in future gamma-ray observation.

6.1 Gamma-ray from DM annihilation

6.1.1 Indirect detection approach

The experimental target in the DM indirect detection is the annihilation or decay signals from DM pair annihilation processes. As reviewed in Sec. 2.1, we assume the interaction between DM and the SM particles in the WIMP hypothesis, and the DM annihilation cross section should be $\langle \sigma v \rangle \sim 10^{-26}$ cm^3/s to reach the correct DM abundance through the freeze-out mechanism. DM annihilation processes may happen in the current universe even after the freeze-out epoch, which may be probed in the astrophysical observation. This is a fundamental idea of the indirect detection experiment. In this approach, DM signals correspond to the excess from the expected background of the astrophysical source. If we observe data that is consistent with the standard prediction, the upper bound on $\langle \sigma v \rangle$ is derived. Therefore, controlling the astrophysical background is crucial. Although this is a challenging task, the canonical cross section in the WIMP scenario can be directly tested.

In Fig. 28, we show the schematic picture for the indirect detection of DM annihilation processes. DM may have a variety of annihilation channels such as electroweak bosons and a pair of quarks. The dominant DM annihilation or decaying channels differ in each DM theory. What we may observe in the observation are fragments of particles in DM annihilation.

As pointed out in Ref. [41], including electroweak corrections in the final states is crucial especially to predict the low energy spectrum. The point is that the electroweak radiative corrections do not cancel and have the Sudakov double log corrections, $\sim \alpha_2 \log^2(s/m_W^2)$. This double log structure cancels in the QED processes if we sum over the soft final states inclusively, which are almost degenerated with the hard indices. In the QCD processes, initial states are color singlet states, and thus the soft singularities also cancel out due to the inclusive summation of the color indices. These facts are known as the Bloch-Nordsieck theorem [42, 43, 44]. In the electroweak processes, on the other hand, initial states have fixed electroweak charges. Therefore, the soft corrections do not compensate with each other known as the violation of the Bloch-Nordsieck theorem, as pointed out in Ref. [45]. The situation is the same in DM annihilation processes, especially for electroweakly charged DM. Since the initial DM pair is non-relativistic, the center mass energy $\sqrt{s} \sim 2m_{\mathrm{DM}}$ is much larger than m_W assuming $m_{\mathrm{DM}} \gtrsim \mathcal{O}(1)$ TeV. The soft electroweak corrections to the final state legs are enhanced by the Sudakov double log corrections. After the primary processes, the

energy is distributed into a large number of stable particles produced through electroweak corrections. Consequently, the low energy spectrum ($\lesssim$ 100 GeV) is enhanced. All the particles charged under $\mathrm{SU}(2)_L \times \mathrm{U}(1)_Y$ may appear, in principle, in the final spectrum. Note that these final leg corrections are calculated independently from the primary annihilation processes, which are included in numerical code released in [46], while the primary channels in DM pair annihilation depend on each DM theory. The following representative primary states are considered.

$$\begin{aligned}
\text{charged lepton pair:} &\quad e_L^+ e_L^-, e_R^+ e_R^-, \mu_L^+ \mu_L^-, \mu_R^+ \mu_R^-, \tau_L^+ \tau_L^-, \tau_R^+ \tau_R^-, \\
\text{neutral lepton pair:} &\quad \nu_e \bar{\nu}_e, \nu_\mu \bar{\nu}_\mu, \nu_\tau \bar{\nu}_\tau, \\
\text{quark pair:} &\quad q\bar{q}, c\bar{c}, b\bar{b}, t\bar{t}, \\
\text{massless vectors:} &\quad \gamma\gamma, gg, \\
\text{massive vectors:} &\quad W_L^+ W_L^-, W_L^+ W_L^-, Z_L Z_L, Z_T Z_T, \\
\text{scalar pair:} &\quad hh,
\end{aligned}$$

where $q = u, d, s$ denotes light quarks and V_T (V_L) denotes the transverse (longitudinal) polarization for massive vector V. These primary states experience parton showers and hadronization. These processes are calculated by the Monte Carlo simulation programs such as `PYTHIA` [47] and `HERWIG` [48].

Comparing the theoretical predictions and the observed astrophysical data, we may perform the DM signatures as the unexpected excess from the background. Various searching channels are proposed and studied.

- Antiprotons were suggested by [49, 50] for the sensitive channels to excess originated from DM annihilation. The more systematical study is given by [51, 52, 53]
- Positrons were studied in [49, 51, 52, 54]
- Antideuterons were studied in [55, 56, 57]
- Gamma-ray was first studied as DM searching channel in [58, 59, 60] and revisited by [51].

For the electrically charged channels, well-studied targets are the antimatter such as positron and antiproton as listed above. The greatest advantage of focusing on the antiparticles is to suppress the abundance of the background. For instance, the antiproton-proton flux ratio is $\lesssim 10^{-4}$ in the $1 - 100$ GeV region [61], and thus the antiproton channel is sensitive to the small exotic injection from DM annihilation or decay. The antimatter signals are searched by the magnetic spectrometer such as the PAMELA experiment [62, 63] and the AMS-02 experiments [64], which are sensitive to the GeV to TeV mass range of DM. The magnetic spectrometer identifies the electric charge, energy, and momentum of the cosmic-ray. The electrically charged final particles are affected by the magnetic fields in Milky Way galaxy, called *galactic transport*, and thus it is important to trace the propagation in the diffusion disc. The uncertainty in the galactic transport is one of the main sources of uncertainty in the standard prediction for the cosmic-ray [65].

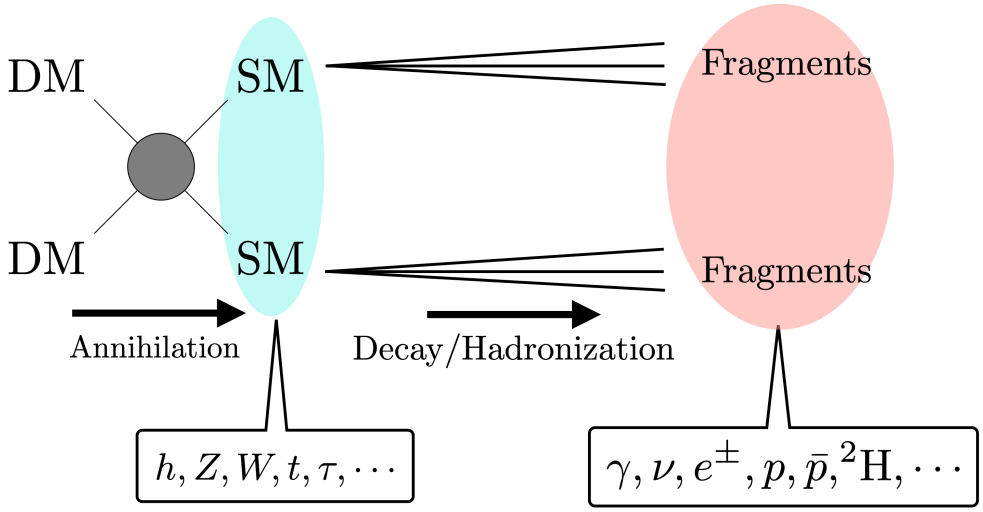

Figure 28: Indirect detection of DM annihilation processes. The fragments are stable particles such as a photon, neutrino, electron and their anti-particles.

The electrically neutral channels, such as neutrino and gamma-ray, propagate without suffering the uncertainty of the galactic transport. Therefore, we may choose the targets to search DM signals in each strategy. For the gamma-ray channel, one of the most efficient target region is the Galactic Center (GC) region. The most DM-dense circumstance is realized in the GC region because DM is gravitationally trapped and distributes with the high density. Since the gamma-ray flux from a DM pair annihilation is proportional to the squared DM density, the GC region is the suitable region to search the gamma-ray signals. The observed gamma-ray spectrum is composed of two parts: One is the continuum spectrum induced from the quarks, heavy charged leptons, and electroweak bosons. These particles emit the secondary photon through inverse Compton scatterings and bremsstrahlung of electrons. This continuum spectrum is predicted up to DM mass where all the annihilation channels kinematically vanish. The other one is the line spectrum associated with the primary photon emission. This narrow spectrum is predicted by the final state of γX where X denotes a neutral particle such as γ and Z. These line signatures are broadened by the additional photon emissions from the final state radiation in the charged modes and the virtual bremsstrahlung [66, 67]. In the succeeding section, we give theoretical formalism to derive constraints on DM theories from the observational gamma-ray search.

6.1.2 Monochromatic gamma-ray search

The photon flux from a DM pair annihilation is given by

$$\frac{d\Phi}{dE_\gamma}(E_\gamma, \Delta\Omega) = \frac{\langle \sigma v \rangle}{8\pi m^2} \frac{dN}{dE_\gamma}(E_\gamma) \cdot J(\Delta\Omega), \tag{6.1}$$

where $\langle \sigma v \rangle$ denotes the velocity weighted DM annihilation cross section and dN/dE_γ denotes the energy spectrum for the number of photons. For a DM annihilation channel into two

photons, the dN/dE_γ is constrained to be

$$\frac{dN}{dE_\gamma}(E_\gamma) = 2 \times \delta(m_{\rm DM} - E_\gamma), \tag{6.2}$$

and thus the narrow peak at $E_\gamma \simeq m_{DM}$ is predicted. The astrophysical properties are all included in $J(\Delta\Omega)$, which is called *J-factor* [68].

$$J(\Delta\Omega) = \int_{\Delta\Omega}\int_{\rm LOS} ds\ d\Omega\ \rho^2\left(r(s,\theta)\right). \tag{6.3}$$

The squared DM density is integrated along with the line of sight (LOS) for fixed solid angle $\Delta\Omega$. The variable r for DM density is defined as

$$r \equiv (r_\odot^2 + s^2 - 2r_\odot s\cos\theta)^{\frac{1}{2}}, \tag{6.4}$$

where s denotes the distance along the LOS, θ denotes the angle between the direction of the GC and observation, and $r_\odot = 8.5$ kpc denotes the distance from the GC [69].

The High Energy Stereoscopic System (H.E.S.S.) is the imaging air Cherenkov array, which is released the latest gamma-ray search in the GC region [70]. In this analysis, the constraint on DM annihilation cross section is derived from ten years of observation taken by the initial four telescopes. The large photon statistics are realized, and thus the wide sensitivity of DM mass, 300 GeV-70 TeV, is covered.

In the H.E.S.S analysis, the event selection and reconstruction are performed by the advanced semi-analytical shower model technique developed in Ref. [71]. This technique is based on χ^2 comparison of the observed shower images, which are images of photons induced electromagnetic shower in the camera, with calculated shower images from a model of the Cherenkov light distribution in electromagnetic showers. The Cherenkov light distribution of a shower is characterized by the longitudinal, lateral, and angular distributions of charged particles in the shower, which are derived from Monte Carlo simulations and parametrized to realize analytical description. The contribution of the night sky background noise is also treated by modeling its camera images in every pixel and performing a detailed statistical analysis. To observe the GC region, it is important to mitigate this background because the night sky noise may affect the normalization of the signal and background region exposure through the systematic effects in the event acceptance [72, 73]. This technique enables us to reconstruct the energy value and the direction of each event, and the energy resolution, $\Delta E_\gamma/E_\gamma$, has a root mean square of 10 % above 300 GeV DM mass.

The signal and background events are separated by comparing the two separated regions. The DM annihilation signals are searched in the region of interest (ROIs), the annuli with inner radii of 0.3°-0.9° in radial distance from the GC. These regions are named the `ON region`. Some regions are excluded from the ON regions to avoid the astrophysical very-high-energy (VHE, $E_\gamma \gtrsim 100$ GeV) gamma-ray source. In the analysis of Ref. [70], a region with $\pm 0.3°$ for the Galactic latitude and $\pm 1°$ for the Galactic longitude is eliminated to avoid the contamination of the VHE gamma-ray source observed by the previous H.E.S.S observations such as the super massive black hole Sagittarius A*[74, 75], the supernova and

pulsar wind nebula G0.9 + 0.1 [76], and a diffuse emission extending along the Galactic plane [77, 78, 79]. A disk region with 0.4° is also excluded to avoid the supernova remnant named HESS J1745-303 [80]. An *OFF region* is defined symmetrically to the ON regions with respect to each observational pointing position and is observed with the same acceptance and observational conditions. See Fig. 1 in Ref. [70] for the schematic picture showing how to choose ON and OFF regions. The values of the J-factor differ between ON and OFF regions due to the location relative to the GC. If we assume the cusped Einasto profiles, the value for the ON region is larger by 3.5 than the OFF region.

The two dimensional (2D) binned Poisson maximum likelihood analysis is performed for the signal search. The spectral and spatial features of DM annihilation signals are exploited in this method. Each event is divided by the value of observed gamma-ray energy and spatial information. The whole energy region, 300 GeV-70 TeV, is divided into 60 bins on a logarithmic scale. The ON region is divided into seven regions of annuli of 0.1° and each annulus has different value of the J-factor. The numerical values, assuming cusped profiles, are listed in TABLE I of Ref. [81]. There is no statistically significant excess in the ON region compared with the OFF region, and thus we obtain the upper bound on the monochromatic flux, Φ, from DM annihilation for each energy bin. This upper bound on $\langle\sigma v\rangle$ is also obtained since the differential flux is proportional to $\langle\sigma v\rangle$. If we assume the final state particles have negligible masses compared to DM mass, we obtain $E_\gamma \simeq m_{\rm DM}$. This relation enables us to draw the excluded region on the $m_{\rm DM}$ vs Φ ($\langle\sigma v\rangle$) plane as shown in Ref. [70], see the left (right) panel of Fig. 2.

The CTA is next-generation imaging Air Cherenkov Array, which is sensitive to higher energy regions. The Observatory is distributed to two places, La Palma in the northern hemisphere and Chile in the southern hemisphere. The greatest feature of the CTA is that different sizes of telescopes will be constructed to maximize the sensitivity. We have three types of telescopes in the CTA.

- The 4 m Small-Sized Telescope (SST) covering 2 TeV - 200 TeV
- The 12 m Medium-Sized Telescope (MST) covering 100 GeV - 10 TeV
- The 23 m Large-Sized Telescope (LST) covering 20 GeV - 2 TeV

The SSTs are only sensitive to the high energy region due to the limitation of area. and thus the low- and mid- energy region will be covered by LST and MST. The northern hemisphere array will be composed of the four LST, fifteen MST, and MAGIC. Since there is no SST, which is important to observe the high energy region, this array will focus on the energy range of 20 GeV to 10 TeV. The southern hemisphere array will be composed of the four LST, twenty-five MST, and seventy SST. To increase sensitivity in the high energy region, it is important to increase the number of SST to enlarge their effective area as much as possible. The full range of energy sensitivity 20 GeV to 200 TeV is realized in this southern array. The GC region is observed by this southern array. Compared to the H.E.S.S. experiment, the differential flux sensitivity of the CTA will be improved by an order of magnitude. Besides, the energy sensitivity will be pushed up by an order of magnitude. The CTA experiments

may observe sufficient numbers of events since its effective area (after gamma-ray/hadron separation cuts) will reach $\sim \mathcal{O}(1)$ km^2 for a large gamma-ray energy region. Therefore, the sensitivity tend to be saturated for the long time observation.

6.2 Monochromatic gamma-ray search of electroweakly interacting DM

We study the gamma-ray line signatures from electroweakly interacting DM and compare the predictions of spin-1/2 and spin-1 DM. We study signatures of monochromatic gamma-ray lines in the GC region. Since predicted flux is proportional to the squared DM density, the derived constraints highly depend on the density profiles. We take some benchmark profiles to show this uncertainty in our result.

6.2.1 Line cross section

The latest analysis for the gamma-ray line signals from DM annihilation is performed by the H.E.S.S. collaboration using the ten years of data for the gamma-ray observation in the GC region [70]. In our model, we have three annihilation modes involving the gamma-ray line signals, $\{\gamma\gamma, Z\gamma, Z'\gamma\}$. The annihilation cross section formulas are derived in Sec. 4.2.2 and Sec. 4.2.3. For the $\gamma\gamma/Z\gamma$ modes, the photon energy is approximately equivalent to the DM mass, $E_\gamma \simeq m_V$, where we take the NR limit for the initial DM pair and neglect m_Z. For the $Z'\gamma$ mode, we can not neglect $m_{Z'}$ because $m_{Z'}$ must be heavier than m_V, see Eq. (3.117). The photon energy in the $Z'\gamma$ annihilation mode depends on both m_V and $m_{Z'}$.

$$E_\gamma \simeq m_V \left(1 - \frac{m_{Z'}^2}{4m_V^2}\right) \equiv m_V - \Delta E_\gamma, \tag{6.5}$$

where $\Delta E_\gamma \equiv m_{Z'}^2/(4m_V)$. If the $Z'\gamma$ mode is kinematically allowed, $m_{Z'} \lesssim 2m_V$, we may observe the double-peak gamma-ray spectrum at $E_\gamma \simeq m_V - \Delta E_\gamma$ and $E_\gamma \simeq m_V$. To distinguish between these two peaks, $\Delta E_\gamma/m_V$ should be larger than the instrumental energy resolution. In the H.E.S.S. experiment, the energy resolution is about 10 % for $m_{\rm DM} \gtrsim 300$ GeV in gamma-ray observation. Our interesting region, to search double peak signatures, is specified below.

$$1.02 \lesssim \frac{m_{Z'}}{m_V} < 2, \tag{6.6}$$

where the lower and upper values come from the g_0 perturbative unitarity and the kinematical suppression of the $Z'\gamma$ annihilation mode, respectively. The condition to discriminate between two peaks, $\frac{\Delta E_\gamma}{m_V} \gtrsim 0.1$, is always satisfied if we focus on this region. Therefore, we can discriminate the gamma-ray peak originated from the $\gamma\gamma/Z\gamma$ modes and the peak from the $Z'\gamma$ mode. This double-peak gamma-ray spectrum is an outstanding signal of our DM model, and we can read out the values of m_V and $m_{Z'}$ from this double-peak spectrum.[23]

[23]Similar signals are predicted in the context of the extra-dimensional models. See Ref. [82] for the discussion in a model with six-dimensions.

We define the *line cross section*, which contributes to the monochromatic gamma-ray line signal. We introduce two types of line cross sections that predict final photon energies.

$$\langle \sigma v_{\rm rel} \rangle^{\rm line}_{\gamma\gamma, Z\gamma} = \langle \sigma v_{\rm rel} \rangle_{\gamma\gamma} + \frac{1}{2} \langle \sigma v_{\rm rel} \rangle_{Z\gamma} \qquad \text{Energy peak: } E_\gamma \simeq m_V, \tag{6.7}$$

$$\langle \sigma v_{\rm rel} \rangle^{\rm line}_{Z'\gamma} = \frac{1}{2} \langle \sigma v_{\rm rel} \rangle_{Z'\gamma} \qquad \text{Energy peak: } E_\gamma \simeq m_V \left(1 - \frac{m^2_{Z'}}{4 m^2_V} \right). \tag{6.8}$$

We derive the excluded region by using the experimental bound shown in Fig. 6 of Ref. [70]. In their analysis, all the masses for final state particles are assumed to be negligible, and thus we can directly compare these constraints with $\langle \sigma v_{\rm rel} \rangle^{\rm line}_{\gamma\gamma, Z\gamma}$. We can also derive a constraint on $\langle \sigma v_{\rm rel} \rangle^{\rm line}_{Z'\gamma}$ by noting that the horizontal axis of Fig. 6 in Ref. [70] corresponds to E_γ. These constraints are derived by assuming these three cuspy DM density profiles as defined below.

- Einasto profile [82]/Einasto2 profile [46]

$$\rho_{\rm Einasto}(r) \equiv \rho_s \exp\left[-\frac{2}{\alpha_s} \left(\left(\frac{r}{r_s} \right)^{\alpha_s} - 1 \right) \right]. \tag{6.9}$$

- Navarro-Frenk-White (NFW) profile [83]

$$\rho_{\rm NFW}(r) \equiv \rho_s \left(\frac{r}{r_s} \left(1 + \frac{r}{r_s} \right)^2 \right)^{-1}. \tag{6.10}$$

In Table. 11, we summarize the parameters for the cuspy DM density profiles used in Ref. [70]. Another choice is the cored DM density profile. The core radius, r_c, depends on the model of baryonic physics, and cores extending to $r_c \sim 5$ kpc can potentially be obtained [84]. The cored Einasto profile is defined as shown below.

$$\rho(r) = \begin{cases} \rho_{\rm Einasto}(r) & \text{for } r > r_c, \\ \rho_{\rm Einasto}(r_c) & \text{for } r < r_c, \end{cases} \tag{6.11}$$

where $\rho_{\rm Einasto}(r)$ is defined in Eq. (6.9). For the cored profile, ρ_s is chosen to realize the value of the local DM density. We show the current excluded region with the cusped DM density profiles assumed in the analysis of the H.E.S.S. collaboration [70]. The sensitivity of the H.E.S.S. experiment is studied for the cored profiles in Ref. [85], which is focusing on the pure Wino DM search.[24] From this study, the upper bound on the line cross section will be weakened by a factor of $\mathcal{O}(10 - 100)$ if we use the cored DM density profile.

6.2.2 Constraint from gamma-ray line signatures

We compare the predicted line cross section between our spin-1 DM and the Wino DM system. In Fig. 29, we show the predicted value of $\langle \sigma v_{\rm rel} \rangle^{\rm line}_{\gamma\gamma, Z\gamma}$ and experimental upper bounds. The

[24] See the left panel of Fig. 7 in Ref. [85].

Table 11: The cuspy DM density profiles used in Ref. [70].

Profiles	Einasto [82]	NFW [83]	Einasto2 [46]
$\rho_{\rm s}$ [GeV cm^{-3}]	0.079	0.307	0.033
$r_{\rm s}$ [kpc]	20.0	21.0	28.4
$\alpha_{\rm s}$	0.17	–	0.17

solid (dashed) black curve shows the line cross section including the Sommerfeld effects for our spin-1 DM (the pure Wino DM). The green region with a solid boundary is the excluded region by the H.E.S.S. observation [70] for the Einasto profile [82]. We also show green dashed and green dotted curves as the upper limits on the cross section for the cusped NFW profile [83] and the Einasto2 profile [46], respectively. Since our spin-1 DM and the Wino DM have the SU(2)$_L$ triplet features, the Sommerfeld resonance structures are almost the same. The line cross section for the spin-1 DM is larger than that for the Wino DM by 38/9, and thus we obtain more severe constraints on the spin-1 DM. We find the following excluded regions for our spin-1 DM depending on the DM density profiles.[25]

- Einasto profile

$$300\ \text{GeV} \lesssim m_V \lesssim 14.4\ \text{TeV} \quad \text{(Excluded region 1)}, \tag{6.12}$$
$$16.5\ \text{TeV} \lesssim m_V \lesssim 22.9\ \text{TeV} \quad \text{(Excluded region 2)}, \tag{6.13}$$
$$33.8\ \text{TeV} \lesssim m_V \lesssim 37.5\ \text{TeV} \quad \text{(Excluded region 3)}. \tag{6.14}$$

- Cusped NFW profile

$$300\ \text{GeV} \lesssim m_V \lesssim 12.5\ \text{TeV} \quad \text{(Excluded region 1)}, \tag{6.15}$$
$$17.9\ \text{TeV} \lesssim m_V \lesssim 22.2\ \text{TeV} \quad \text{(Excluded region 2)}, \tag{6.16}$$
$$34.8\ \text{TeV} \lesssim m_V \lesssim 36.7\ \text{TeV} \quad \text{(Excluded region 3)}. \tag{6.17}$$

- Einasto2 profile

$$300\ \text{GeV} \lesssim m_V \lesssim 11.7\ \text{TeV} \quad \text{(Excluded region 1)}, \tag{6.18}$$
$$18.6\ \text{TeV} \lesssim m_V \lesssim 21.6\ \text{TeV} \quad \text{(Excluded region 2)}, \tag{6.19}$$
$$35.0\ \text{TeV} \lesssim m_V \lesssim 36.1\ \text{TeV} \quad \text{(Excluded region 3)}. \tag{6.20}$$

The lower value of 300 GeV comes from the limitation for the energy resolution in the H.E.S.S experiment. Let us again note that these bounds are weakened by $\mathcal{O}(10-100)$ if we choose cored DM density profiles.

[25] If we take $m_{h'} \simeq m_V$, the parameter region in Fig. 30 may be constrained by the perturbative unitarity bounds on the scalar couplings, which is studied in our previous collaboration [25]. We can evade these unitarity bounds by taking sufficiently small values of ϕ_h and $m_{h'}$.

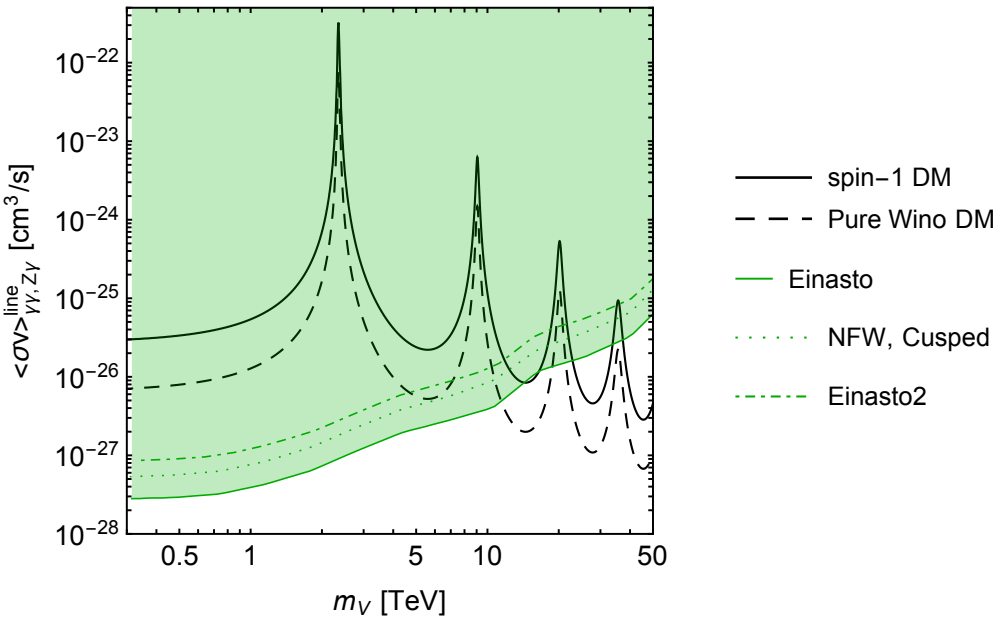

Figure 29: The comparison of the line cross sections between our spin-1 DM and the Wino DM. The solid (dashed) black curve shows $\langle\sigma v_{\rm rel}\rangle^{\rm line}_{\gamma\gamma,Z\gamma}$ for our model (pure Wino). The green shaded region shows the constraint from the H.E.S.S. observation in the GC region [70] for the Einasto profile [82]. The green dotted and green dashed curves show the upper limit for the NFW profile [83] and Einasto2 profile [46], respectively. The upper bound is expected to be weakened by a factor of $\mathcal{O}(10-100)$ for the cored DM density profile. Reprinted from [**?**], Copyright 2021, The Authors licensed under CC-BY 4.0.

In Fig. 30, we show the current bound on the line cross section by the H.E.S.S. observation for the Einasto DM density profiles [82] focusing on the region in Eq. (6.6). The green regions are excluded by $\langle\sigma v_{\rm rel}\rangle^{\rm line}_{\gamma\gamma,Z\gamma}$ shown in Eqs. (6.12)-(6.14). These green regions are extended for $m_{Z'}/m_V \geq 2$ where the annihilation into $Z'\gamma$ is forbidden kinematically. The blue region is excluded by $\langle\sigma v_{\rm rel}\rangle^{\rm line}_{Z'\gamma}$. The black solid, dashed, dot-dashed, and dotted contours show the predicted value of $\langle\sigma v_{\rm rel}\rangle^{\rm line}_{Z'\gamma}$ for 10^{-24}, 10^{-25}, 10^{-26}, and 10^{-27} in the unit of cm^3/s, respectively. The red solid lines show the g_0 contours. In Fig. 31, we show the constraints for the NFW [83], and Einasto2 DM density profiles [46]. The derived constraints depend on the DM density profiles. The blue excluded regions from $\langle\sigma v_{\rm rel}\rangle^{\rm line}_{Z'\gamma}$ give stronger constraints for $m_{Z'} \simeq m_V$. This is due to we have the enhancement factor in the coupling of Z', $g_{Z'}$, defined in Eq. (3.92). Note that g_0 gets larger in the same region, and thus we expect relatively large higher-order correction for our perturbative calculations.

We have a further chance to explore the parameter region in the upcoming CTA experiment [86, 87]. The prospect sensitivity for the line gamma-ray signals is studied by Ref. [88] for the Wino and Higgsino DM. In Fig. 32, we show the current bound and sensitivity expected in the CTA. The green region is excluded by the H.E.S.S. observation for the

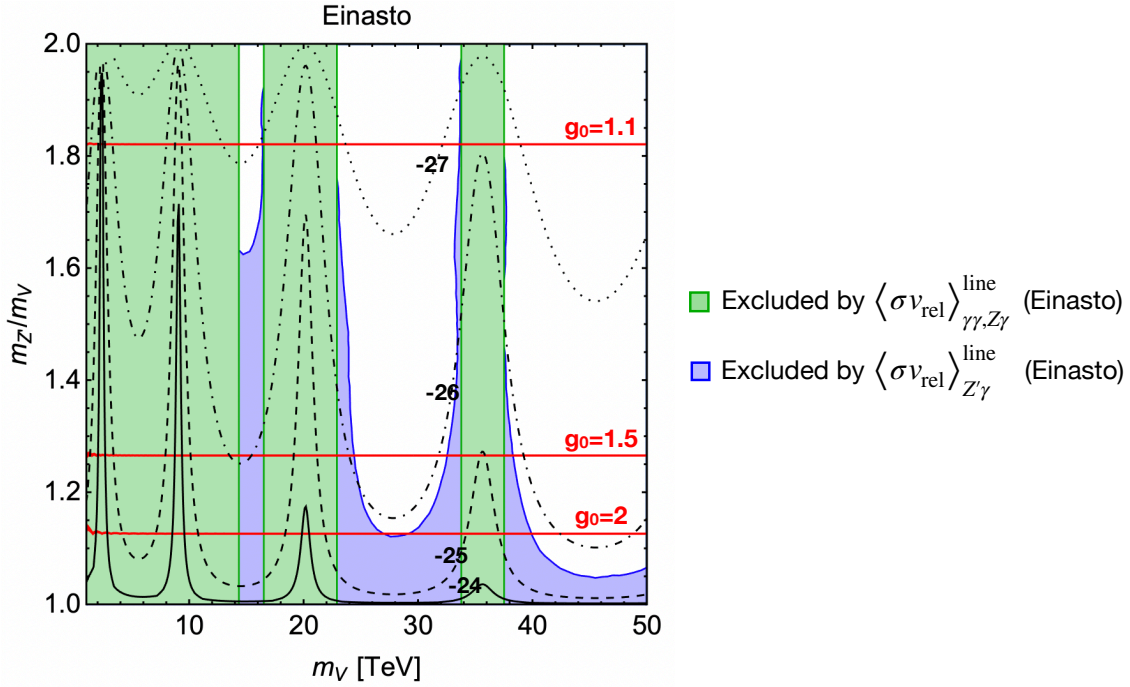

Figure 30: The current bound on the line cross section by the H.E.S.S. observation assuming the Einasto profile [82]. The green regions are excluded by $\langle \sigma v_{\rm rel} \rangle^{\rm line}_{\gamma\gamma, Z\gamma}$ while the blue regions are excluded by $\langle \sigma v_{\rm rel} \rangle^{\rm line}_{Z'\gamma}$. The black solid, dashed, dot-dashed, and dotted contours show the predicted value of $\langle \sigma v_{\rm rel} \rangle^{\rm line}_{Z'\gamma}$ for 10^{-24}, 10^{-25}, 10^{-26}, and 10^{-27} in the unit of cm^3/s, respectively. The red solid lines show the g_0 contours. Reprinted from [**?**], Copyright 2021, The Authors licensed under CC-BY 4.0.

cusped Einasto2 profile shown in the lower panel of Fig. 31. We use the prospect derived in Ref. [88] to show the CTA sensitivity. The orange region with the dashed boundary shows the most conservative sensitivity assuming the core radius, $r_c = 5$ kpc, and we will obtain $m_V \gtrsim 25.3$ TeV as the prospect bound. The whole parameter region in Fig. 32 will be covered if we take $r_c \lesssim 2$ kpc.

As found from this figure, we may probe gamma-ray signatures from spin-1 DM. If we choose cusped DM density profiles, DM mass region for $m_V \lesssim 10$ TeV is already excluded. If we choose cored DM profiles, on the other hand, we may find the viable parameter regions where we may achieve the correct value of Ωh^2. Compared with the Wino DM, we only expect one peak at $E_\gamma \sim m_{\rm DM}$. In this discrimination between these two DM models, therefore, a double peak spectrum will be a distinctive signature for spin-1 DM. Besides, we may reconstruct not only DM mass but also Z' mass from the peak locations. If we may detect Z' mass through this double peak search, we may perform the consistency check such as Z' search in High Luminosity LHC [89] as studied in our previous work [25].

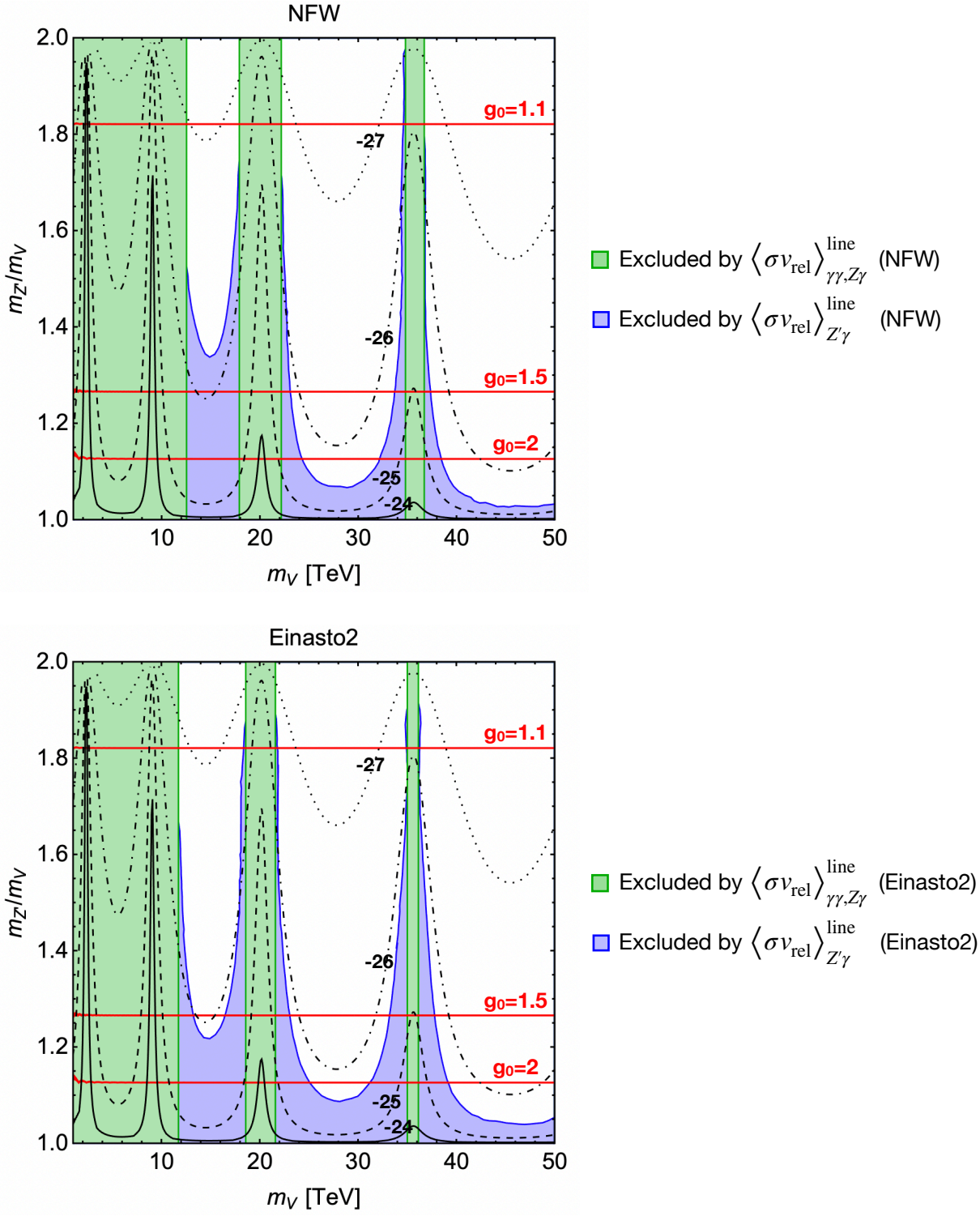

Figure 31: The constraints on the line cross section for the different DM density profiles. The upper and lower panels show the constraints for the NFW profile [83] and the Einasto2 profile [46], respectively. Descriptions for each plot are given in the caption of Fig. 30. Reprinted from [**?**], Copyright 2021, The Authors licensed under CC-BY 4.0.

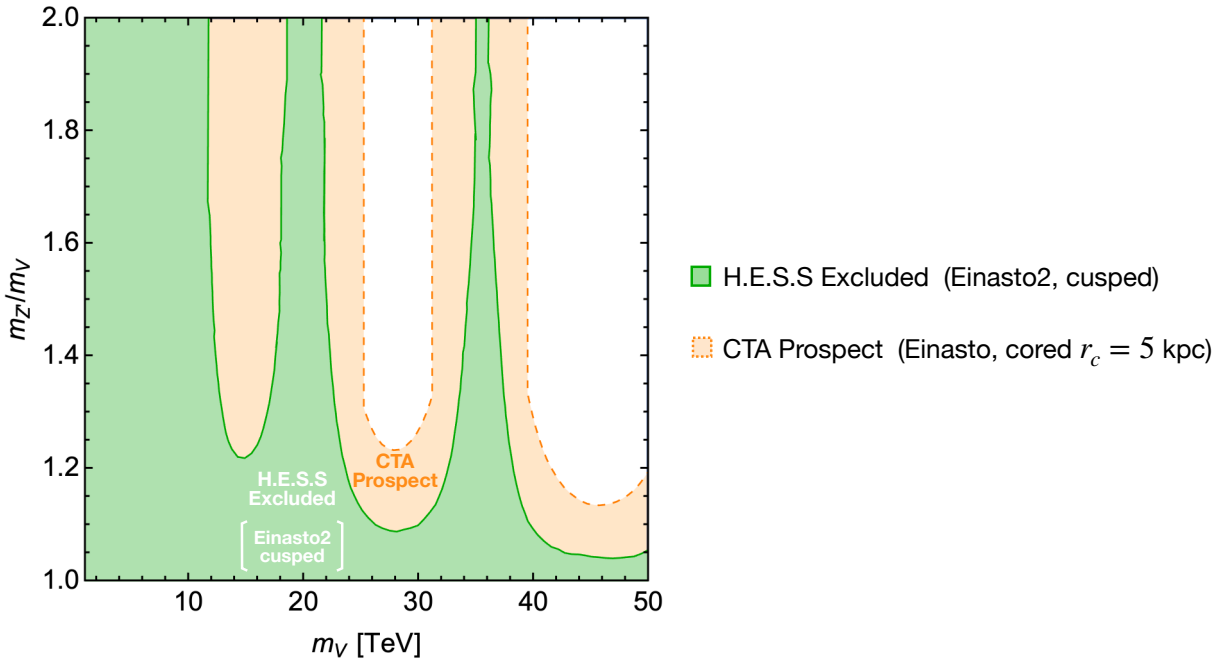

Figure 32: The current bound from the H.E.S.S. observation and the prospect in the CTA. The green region is excluded by the H.E.S.S. collaboration for the Einasto2 profile [46] shown in the lower panel of Fig. 31. The orange region with the dashed boundary is the prospect sensitivity in the CTA for the cored Einasto profile with $r_c = 5$ kpc, which is the most conservative one studied in Ref. [88]. If we take $r_c \lesssim 2$ kpc, the prospect sensitivity will cover the whole region of this figure. Reprinted from [**?**], Copyright 2021, The Authors licensed under CC-BY 4.0.

7 Conclusions

The electroweakly-charged DM is one of the most promising DM candidates and predicts possible signals in the next-generation DM searches such as XENONnT, LZ, and CTA experiments. These experiments will provide an unprecedented chance to obtain DM signatures from these candidates. Preparing for this exciting era, the possibility of the model construction for the electroweakly-charged DM is systematically studied mainly focused on the spin-0 and spin-1/2 scenarios.

Since our goal is not only to obtain the DM signatures but also to identify DM theory, signal discrimination between various DM candidates is an essential issue. Determination of the quantum numbers of DM, such as spin and electroweak charges, is important. In particular, DM spin is one of the most fundamental quantum numbers that determine DM physics. To discriminate DM spin from the experimental data, we need to study DM phenomenologies, determine the interesting parameter region, and specify spin-dependent features from the observables.

The most nontrivial discrimination is a comparison between DM candidates that have the same interactions but with different spins. One interesting separation is discrimination between electroweakly interacting DM candidates predicted from a supersymmetric theory and a theory with extra-dimension. In these two scenarios, discrete symmetry to stabilize DM, such as R-parity and KK-parity, are realized. The lightest parity-odd particle is stabilized and stable DM candidate. Several DM candidates appear depending on each model, and electroweakly interacting DM with the same $\mathrm{SU}(2)_L$ triplet and $Y = 0$ interaction appear in both of these scenarios, the Wino DM (spin-1/2 DM) and the KK electroweak boson DM (spin-1 DM). Since these DM candidates are directly related to BSM scenarios, we may obtain implications on the physics behind DM by discriminating signatures from spin-1/2 and spin-1 DM candidates. However, DM spin determination is highly nontrivial in this case. This is because spin-dependent features tend to decouple from the low energy signatures. We need to carefully study predictions in each model and extract non-decoupling spin-dependent features. Although spin-1/2 DM phenomenologies are studied in detail in contexts of the Wino DM study, spin-1 DM phenomenologies are only studied in some benchmark models. In particular, we have wide varieties of the spectrum of KK modes, which may crucially determine phenomenologies. If the second KK mode may appear in the final states of DM annihilation, we have new annihilation modes, which realize an effectively larger annihilation cross section for DM.

In this thesis, phenomenologies of electroweakly interacting spin-1 DM are studied. We use a simplified renormalizable model of spin-1 DM to reveal phenomenologies of electroweakly interacting DM candidates in an extra-dimensional setup with assuming as a general mass spectrum as possible. In this model, DM interacts with the SM electroweak vectors through $\mathrm{SU}(2)_L$ triplet and $Y = 0$ non-abelian vector couplings. Therefore, the electroweak interaction may dominate DM physics, and similar features are realized in the spin-1/2 DM system such as the nearly degenerated mass spectrum and the electroweak forces between DM multiplet. Comparing predictions between spin-1/2 and spin-1 DM system, DM spin discrimination is discussed by focusing on a benchmark scenario, which corresponds to dis-

crimination between the Wino DM and the KK electroweak boson DM.

In this system, the electroweak potential force plays an important role to evaluate predictions on DM annihilation, which is known as the Sommerfeld effects. To describe the DM annihilation processes, the NR effective field theory for electroweakly interacting spin-1 DM system is derived following the method systematically formulated in the spin-1/2 DM system. The matching procedure and formalism in this thesis are applicable for the spin-1 DM with arbitrary electroweak charges. We applied our general formalism for the $\mathrm{SU}(2)_L$ triplet DM system and compare our results with the prediction in the spin-1/2 DM system, with $\mathrm{SU}(2)_L$ triplet and $Y = 0$ interactions, derived in the previous studies at the leading order in the NR limit.

In order to specify the relevant annihilation processes, we systematically listed up spin-1 DM annihilation modes, which are classified by the initial states, final states, and the topology of the diagrams. We specify the leading order contributions. The general formulas for these leading order annihilation cross sections are also derived. Including the effects of the degenerated charged spectrum and the Sommerfeld effects, we numerically solved the Boltzmann equation and evaluated the DM thermal relic abundance for spin-1 DM. The spin-1 DM has an effectively larger annihilation cross section compared with that of spin-1/2 DM due to the larger number of DM spin. Consequently, DM thermal relic abundance is predicted in the heavier DM mass region compared with the spin-1/2 scenario. We also found that the Z_2-even heavier vectors such as Z' and W' in the spin-1 DM system realize the new DM annihilation channels if kinematically allowed. These modes affect the DM abundance depending on the mass ratio between Z' and spin-1 DM, $m_{Z'}/m_V$. In particular, if we take $m_{Z'}/m_V = 1.5$, then the correct abundance is predicted with 4.6 TeV in the spin-1 system. This value is larger than the spin-1/2 DM prediction by 15 %.

We compared the DM signals in the indirect detection experiments in order to conclude the possibility of DM spin discrimination in our benchmark comparison. In particular, we reveal the testable region of monochromatic gamma-ray line signatures from electroweakly interacting spin-1 DM in the CTA experiments. We found spin-1 DM predicts the larger cross section by roughly a factor of 38/9 at the leading order due to the larger number of spin states. Besides, an interesting possibility is seen: our spin-1 DM may predict the separable two peaks in the photon energy spectrum. The one peak originates from the $\gamma\gamma$ and $Z\gamma$ final states, while the other peak arises from the $Z'\gamma$ state where Z' is the heavier parity-even neutral vector in our spectrum. The double peak spectrum can be probed in the CTA, wherein both the DM and Z' mass can be reconstructed from the peak locations. Since the mass relation between spin-1 DM and Z' would be predictable in extra-dimensional DM models, we revealed the possibility to test these scenarios by studying the counterpart of this signal in the extra-dimensional theory. Our analysis in the simplified renormalizable model of spin-1 DM can be applied straightforwardly to the extra-dimensional setup, which corresponds to the more realistic scenario to realize DM stability and electroweak interaction for DM at the same time. We are going to extend our study in this direction in our future collaboration.

A Derivation of effective action

We give the derivation of the effective action shown in Sec. 4.

A.1 Real part of potential

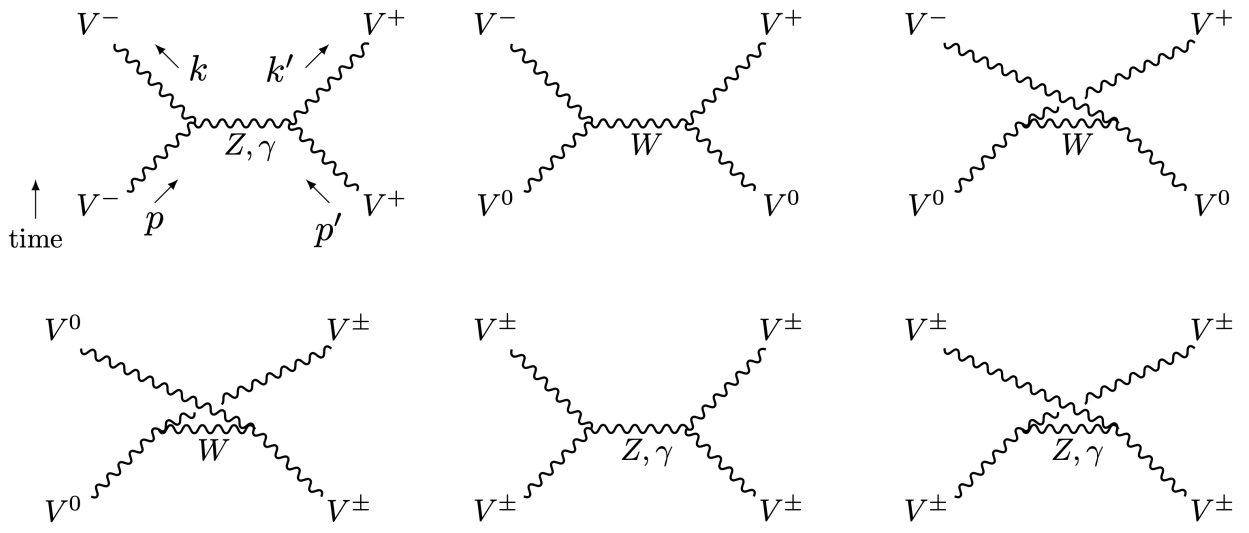

Figure 33: The relevant tree-level diagrams to derive the real part of the potential. The diagrams for $V^-V^+ \to V^0V^0$ mode are implicit.

The real part of the potential is obtained from the amplitudes of the V-particles evaluated in the NR limit. We focus on the electroweak scattering processes which give the leading-order corrections. The corresponding diagrams are shown in Fig. 33. We comment about other contributions which are sub-leading to the electroweak corrections. The exchanges of the Higgs bosons, h and h', and heavy Z_2-even vector bosons, W' and Z', also induce the real part of the potential. The h exchange contribution is suppressed by small ϕ_h. The h', W', and Z' exchange contributions are exponentially suppressed by masses. In our model, V-particles have the vector quadratic couplings, which are suppressed by $1/m_V^2$.

In the NR limit, we obtain the following amplitude at the leading-order.

$$i\mathcal{M}^{Q=0}_{Z,\gamma} \simeq i4m_V^2 \left(\frac{e^2}{|\boldsymbol{p}-\boldsymbol{p}'|^2} + \frac{g_W^2 c_W^2}{|\boldsymbol{p}-\boldsymbol{p}'|^2 + m_Z^2} \right) \epsilon_i(p)\epsilon_i^*(k)\epsilon_j(p')\epsilon_j^*(k'), \tag{A.1}$$

$$\begin{aligned} i\mathcal{M}^{Q=0}_{W} \simeq i4m_V^2 \Bigg(& \frac{g_W^2}{|\boldsymbol{p}-\boldsymbol{p}'|^2 + m_W^2} \epsilon_i(p)\epsilon_i^*(k)\epsilon_j(p')\epsilon_j^*(k') \\ & + \frac{g_W^2}{|\boldsymbol{p}-\boldsymbol{k}'|^2 + m_W^2} \epsilon_i(p)\epsilon_i^*(k')\epsilon_j(p')\epsilon_j^*(k) \Bigg), \end{aligned} \tag{A.2}$$

$$i\mathcal{M}^{Q=\pm1}_{W} \simeq -i4m_V^2 \frac{g_W^2}{|\boldsymbol{p}-\boldsymbol{p}'|^2 + m_W^2} \epsilon_i(p)\epsilon_i^*(k)\epsilon_j(p')\epsilon_j^*(k'), \tag{A.3}$$

$$\begin{aligned} i\mathcal{M}^{Q=\pm2}_{Z,\gamma} \simeq -i4m_V^2 \Bigg[& \Big(\frac{e^2}{|\boldsymbol{p}-\boldsymbol{p}'|^2} + \frac{g_W^2 c_W^2}{|\boldsymbol{p}-\boldsymbol{p}'|^2 + m_Z^2} \Big) \epsilon_i(p)\epsilon_i^*(k)\epsilon_j(p')\epsilon_j^*(k') \\ & + \Big(\frac{e^2}{|\boldsymbol{p}-\boldsymbol{k}'|^2} + \frac{g_W^2 c_W^2}{|\boldsymbol{p}-\boldsymbol{k}'|^2 + m_Z^2} \Big) \epsilon_i(p)\epsilon_i^*(k')\epsilon_j(p')\epsilon_j^*(k) \Bigg], \end{aligned} \tag{A.4}$$

where $\mathcal{M}^Q_{Z,\gamma}$ and $\mathcal{M}^Q_W$ are induced from the neutral and charged boson exchange processes, respectively, and contribute to the two-body state with a total charge $Q = 0, \pm1, \pm2$. The labels of the polarization are implicit. From these amplitudes, we read out the effective action

composed of the NR V-particle operators, which are defined in Eqs. (4.35)-(4.37).

$$
\begin{aligned}
S_{\rm eff}^{Q=0} = & \int d^4R d^3r \frac{\alpha_2 s_W^2 + \alpha_2 c_W^2 e^{-m_Z r}}{r} \\
& \times \left[\mathcal{B}_i^\dagger(R^0, \boldsymbol{R}+\boldsymbol{r}/2)\ \mathcal{B}_i(R^0, \boldsymbol{R}+\boldsymbol{r}/2) \right] \left[\mathcal{D}_j^\dagger(R^0, \boldsymbol{R}-\boldsymbol{r}/2)\ \mathcal{D}_j(R^0, \boldsymbol{R}-\boldsymbol{r}/2) \right] \\
& + \Bigg\{ \int d^4R d^3r \frac{\alpha_2 e^{-m_W r}}{r} \\
& \times \left[\mathcal{A}_i^\dagger(R^0, \boldsymbol{R}+\boldsymbol{r}/2)\ \mathcal{B}_i(R^0, \boldsymbol{R}+\boldsymbol{r}/2) \right] \left[\mathcal{A}_j^\dagger(R^0, \boldsymbol{R}-\boldsymbol{r}/2)\ \mathcal{D}_j(R^0, \boldsymbol{R}-\boldsymbol{r}/2) \right] \\
& + h.c. \Bigg\},
\end{aligned}
\tag{A.5}
$$

$$
\begin{aligned}
S_{\rm eff}^{Q=\pm 1} = & \int d^4R d^3r \frac{-\alpha_2 e^{-m_W r}}{r} \\
& \times \Bigg\{ \left[\mathcal{B}_i^\dagger(R^0, \boldsymbol{R}+\boldsymbol{r}/2)\ \mathcal{A}_i(R^0, \boldsymbol{R}+\boldsymbol{r}/2) \right] \left[\mathcal{A}_j^\dagger(R^0, \boldsymbol{R}-\boldsymbol{r}/2)\ \mathcal{B}_j(R^0, \boldsymbol{R}-\boldsymbol{r}/2) \right] \\
& + \left[\mathcal{D}_i^\dagger(R^0, \boldsymbol{R}+\boldsymbol{r}/2)\ \mathcal{A}_i(R^0, \boldsymbol{R}+\boldsymbol{r}/2) \right] \left[\mathcal{A}_j^\dagger(R^0, \boldsymbol{R}-\boldsymbol{r}/2)\ \mathcal{D}_j(R^0, \boldsymbol{R}-\boldsymbol{r}/2) \right] \Bigg\},
\end{aligned}
\tag{A.6}
$$

$$
\begin{aligned}
S_{\rm eff}^{Q=\pm 2} = & \int d^4R d^3r \frac{-1}{2} \frac{\alpha_2 s_W^2 + \alpha_2 c_W^2 e^{-m_Z r}}{r} \\
& \times \Bigg\{ \left[\mathcal{B}_i^\dagger(R^0, \boldsymbol{R}+\boldsymbol{r}/2)\ \mathcal{B}_i(R^0, \boldsymbol{R}+\boldsymbol{r}/2) \right] \left[\mathcal{B}_j^\dagger(R^0, \boldsymbol{R}-\boldsymbol{r}/2)\ \mathcal{B}_j(R^0, \boldsymbol{R}-\boldsymbol{r}/2) \right] \\
& + \left[\mathcal{D}_i^\dagger(R^0, \boldsymbol{R}+\boldsymbol{r}/2)\ \mathcal{D}_i(R^0, \boldsymbol{R}+\boldsymbol{r}/2) \right] \left[\mathcal{D}_j^\dagger(R^0, \boldsymbol{R}-\boldsymbol{r}/2)\ \mathcal{D}_j(R^0, \boldsymbol{R}-\boldsymbol{r}/2) \right] \Bigg\}.
\end{aligned}
\tag{A.7}
$$

We want to express the two-body effective action in the decomposed form into each partial wave mode. We reform the SO(3) vector indices, i and j, by using the Fierz identity for Grassmann-even operators.

$$
\delta_{ij}\delta_{k\ell} = \sum_{J,J_z} (-1)^J S_{i\ell}^{J,J_z} S_{kj}^{J,J_z *} \qquad (i,j,k,\ell = 1,2,3),
\tag{A.8}
$$

where S_{ij}^{J,J_z} is defined in Eqs. (4.51)-(4.53). After the decomposition, we can express the effective action in terms of the two-body states in Eqs. (4.44)-(4.45). We obtain $\hat{V}$ as given in Eq. (4.65).

A.2 Imaginary part of potential

A.2.1 Matching procedure

To derive the imaginary part of the potential, $\hat{\Gamma}^J$, we perform the operator matching between the two-body field operators and the calculations of the one-loop amplitudes of the V-particles. Since we focus on the annihilation modes into the neutral vectors, the $(1,1)$-component of $\hat{\Gamma}^J$ only has the nonzero value. Therefore, we can use the optical theorem to calculate the imaginary part of the one-loop amplitude.

$$\mathrm{Im}\mathcal{M}|^J_{V^-V^+\to XX'\to V^-V^+} = 2m_V^2 \langle\sigma v_{\rm rel}\rangle^J_{V^-V^+\to XX'} \qquad (XX' = \gamma\gamma, Z\gamma, Z'\gamma), \tag{A.9}$$

where the LHS denotes the imaginary part of the forward scattering amplitude for $V^-V^+ \to XX' \to V^-V^+$ with J which is expressed by $(\hat{\Gamma}^J_{XX'})_{11}$. On the RHS, $\langle\sigma v_{\rm rel}\rangle^J_{V^-V^+\to XX'}$ denotes the partial wave annihilation cross section of $V^-V^+ \to XX'$ for the initial state with J. In the evaluation of the annihilation cross section, we only leave the leading-order terms in the NR limit and take the massless limit for all the SM particles in the final states while we leave the masses of Z'. We derive $\hat{\Gamma}^J$ through the above procedure as summarized in Eqs. (4.59)-(4.64). In the succeeding section, we show how to determine $\hat{\Gamma}^J_{\gamma\gamma}$ as a demonstration.

A.2.2 Derivation of $\hat{\Gamma}^J_{\gamma\gamma}$

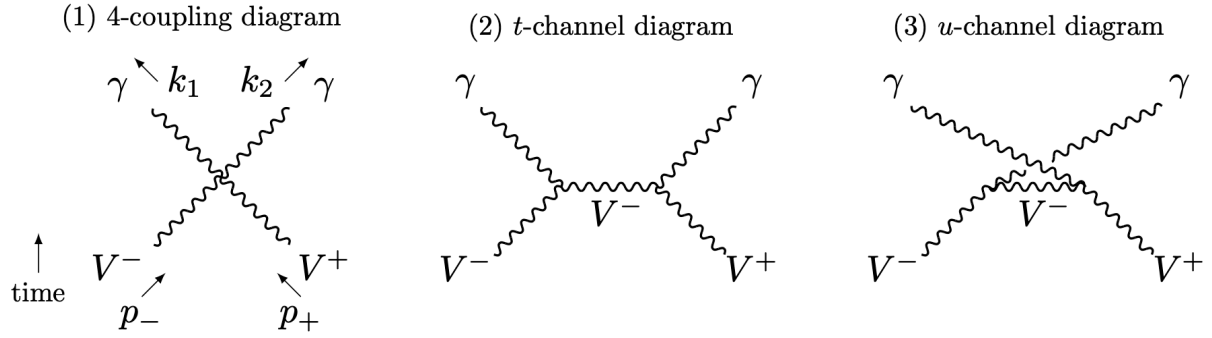

Figure 34: The tree-level diagrams which contribute to $V^-V^+ \to \gamma\gamma$ annihilation.

We show the derivation of $\hat{\Gamma}^J_{\gamma\gamma}$ as a concrete example. We can focus on the nonzero component, $(\hat{\Gamma}^J_{\gamma\gamma})_{11}$. First, we calculate the velocity-weighted annihilation cross section for $V^-V^+ \to \gamma\gamma$. The tree-level diagrams in the unitarity gauge are shown in Fig. 34. The

amplitudes that correspond to each diagram are obtained as follows.

$$i\mathcal{M}_4 = ie^2(g^{\mu\rho}g^{\nu\sigma} + g^{\nu\rho}g^{\mu\sigma} - 2g^{\mu\nu}g^{\rho\sigma})\epsilon_\sigma(p_-)\epsilon_\rho(p_+)\epsilon^*_\mu(k_1)\epsilon^*_\nu(k_2), \tag{A.10}$$

$$\begin{aligned} i\mathcal{M}_t =& ie[(p_- + q)^\mu g^{\alpha\sigma} + (-p_- - k_1)^\alpha g^{\mu\sigma} + (k_1 - q)^\sigma g^{\mu\alpha}]\frac{-i}{q^2 - m_V^2}\left(g_{\alpha\beta} - \frac{q_\alpha q_\beta}{m_V^2}\right) \\ & \times ie[(q - p_+)^\nu g^{\beta\rho} + (-q - k_2)^\rho g^{\beta\nu} + (k_2 + p_+)^\beta g^{\rho\nu}]\epsilon_\sigma(p_-)\epsilon_\rho(p_+)\epsilon^*_\mu(k_1)\epsilon^*_\nu(k_2), \end{aligned} \tag{A.11}$$

$$\begin{aligned} i\mathcal{M}_u =& ie[(p_- + q')^\nu g^{\alpha\sigma} + (-p_- - k_2)^\alpha g^{\nu\sigma} + (k_2 - q')^\sigma g^{\nu\alpha}]\frac{-i}{q'^2 - m_V^2}\left(g_{\alpha\beta} - \frac{q'_\alpha q'_\beta}{m_V^2}\right) \\ & \times ie[(q' - p_+)^\mu g^{\beta\rho} + (-q' - k_1)^\rho g^{\beta\mu} + (k_1 + p_+)^\beta g^{\rho\mu}]\epsilon_\sigma(p_-)\epsilon_\rho(p_+)\epsilon^*_\mu(k_1)\epsilon^*_\nu(k_2), \end{aligned} \tag{A.12}$$

where $q \equiv p_- - k_1$ and $q' \equiv p_- - k_2$.

In the NR limit for the initial V-particles, the zeroth components of the polarization vectors are sub-leading, and we focus on the spatial component, $\epsilon_i(p_-)\epsilon_j(p_+)$. We decompose the amplitude into each partial wave contribution by replacing the initial state polarization vectors with S_{ij}^{J,J_z} defined in Eqs. (4.51)-(4.53).

$$\epsilon_i(p_-)\epsilon_j(p_+) \to S_{ij}^{J,J_z}. \tag{A.13}$$

Note that S_{ij}^{J,J_z} is symmetric matrices for $J = 0, 2$ and anti-symmetric for $J = 1$. Thanks to these properties, the amplitudes in the center-of-mass frame are obtained in the decomposed form, $\mathcal{M}^{J,J_z}$.

$$\mathcal{M}^{0,0} = 2e^2\left[4\epsilon^*_i(k_1)S^{0,0}_{ij}\epsilon^*_j(k_2) - \epsilon^*_i(k_1)\epsilon^*_i(k_2)\left(S^{0,0}_{ii} - \frac{2}{m_V^2}k_j S^{0,0}_{jk}k_k\right)\right], \tag{A.14}$$

$$\mathcal{M}^{1,J_z} = 0, \tag{A.15}$$

$$\mathcal{M}^{2,J_z} = 2e^2\left[4\epsilon^*_i(k_1)S^{2,J_z}_{ij}\epsilon^*_j(k_2) + \epsilon^*_i(k_1)\epsilon^*_i(k_2)\frac{2}{m_V^2}k_j S^{2,J_z}_{jk}k_k\right], \tag{A.16}$$

where $|J_z| \leq J$, and k_i denotes the spatial components of $k_{1\mu}$. We use $S^{2,J_z}_{ii} = 0$ to obtain the above result. The polarization vectors for the photons are given by

$$\epsilon^\pm_i(k_1) = \frac{1}{\sqrt{2}}\begin{pmatrix} \mp\cos\theta \\ -i \\ \pm\sin\theta \end{pmatrix}, \qquad \epsilon^\pm_i(k_2) = \frac{1}{\sqrt{2}}\begin{pmatrix} \pm\cos\theta \\ -i \\ \mp\sin\theta \end{pmatrix}, \tag{A.17}$$

where θ is the scattering angle for the photon with its momentum k_1.

After taking the sum over the final state spins, the squared amplitudes can be expressed

as follow.

$$\sum_{\text{final}} |\mathcal{M}^{0,0}|^2 = 24e^4, \tag{A.18}$$

$$\sum_{\text{final}} |\mathcal{M}^{1,J_z}|^2 = 0, \qquad (J_z = 0, \pm 1), \tag{A.19}$$

$$\sum_{\text{final}} |\mathcal{M}^{2,J_z}|^2 = \begin{cases} 48e^4 \sin^4\theta, & (J_z = 0) \\ 16e^4 \sin^2\theta(3 + \cos 2\theta), & (J_z = \pm 1) \\ 8e^4(1 + 6\cos^2\theta + \cos^4\theta). & (J_z = \pm 2) \end{cases} \tag{A.20}$$

We obtain the cross section for each partial wave mode.

$$\langle \sigma v_{\text{rel}} \rangle^{J=0}_{V^-V^+ \to \gamma\gamma} = 6\frac{\pi\alpha_2^2}{m_V^2} s_W^4, \tag{A.21}$$

$$\langle \sigma v_{\text{rel}} \rangle^{J=1}_{V^-V^+ \to \gamma\gamma} = 0, \tag{A.22}$$

$$\langle \sigma v_{\text{rel}} \rangle^{J=2}_{V^-V^+ \to \gamma\gamma} = \frac{32}{5}\frac{\pi\alpha_2^2}{m_V^2} s_W^4. \tag{A.23}$$

The spin-averaged total cross section is obtained by adding up all the partial wave cross sections.

$$\overline{\langle \sigma v_{\text{rel}} \rangle}^{\text{tot}}_{V^-V^+ \to \gamma\gamma} = \frac{38}{9}\frac{\pi\alpha_2^2}{m_V^2} s_W^4. \tag{A.24}$$

This cross section is larger than that of the Wino DM by a factor of $\frac{38}{9}$. For the $Z\gamma$ mode, we take the massless limit of the Z boson, and the calculation procedure is the same. For the $Z'\gamma$ mode, we do not neglect $m_{Z'}$, and the longitudinal mode also contributes to the final result.

Next, we calculate the imaginary part of the forward scattering amplitude using the two-body effective action shown in Eq. (4.42). Namely, we use the following coupling to calculate the $\gamma\gamma$ contribution to $\text{Im}\mathcal{M}$.

$$S_{\text{eff}} \supset \sum_{J,J_z} i\frac{9}{2}(\hat{\Gamma}^J_{\gamma\gamma})_{11} \int d^4R \; \phi_C^{J,J_z\dagger}(R, \mathbf{0}) \; \phi_C^{J,J_z}(R, \mathbf{0}). \tag{A.25}$$

Using this coupling, we obtain

$$\text{Im}\mathcal{M}|^J_{V^-V^+ \to \gamma\gamma \to V^-V^+} = 2m_V^2 \cdot 9(\hat{\Gamma}^J_{\gamma\gamma})_{11}. \tag{A.26}$$

Comparing with (A.9), we can determine $(\hat{\Gamma}^J_{\gamma\gamma})_{11}$ as shown below.

$$(\hat{\Gamma}^J_{\gamma\gamma})_{11} = \frac{1}{9}\langle \sigma v_{\text{rel}} \rangle^J_{V^-V^+ \to \gamma\gamma} = \begin{cases} \frac{2}{3}\frac{\pi\alpha_2^2}{m_V^2} s_W^4, \\ 0, \\ \frac{32}{45}\frac{\pi\alpha_2^2}{m_V^2} s_W^4. \end{cases} \tag{A.27}$$

This result is summarized in Eqs. (4.59)-(4.60). We can also determine $\hat{\Gamma}^J_{Z\gamma}$ and $\hat{\Gamma}^J_{Z'\gamma}$ in the same procedure.

B Amplitude decomposed into partial waves

We obtain the amplitudes for each type (type-A, -B, -C, and -D) where overall factors of couplings, shown in the fourth column of Table 9, are factorized.

$$\mathcal{M}^{J=0,J_z}\big|_{\text{Type-A}} = \sqrt{3}\left(\frac{1}{2m_V^2} - \frac{4}{4m_V^2 - m_3^2 - m_4^2}\right) + \frac{\boldsymbol{k}\cdot S^{J,J_z}\cdot\boldsymbol{k}}{m_V^2}\frac{4}{4m_V^2 - m_3^2 - m_4^2}, \tag{B.1}$$

$$\mathcal{M}^{J=1,J_z}\big|_{\text{Type-A}} = 0, \tag{B.2}$$

$$\mathcal{M}^{J=2,J_z}\big|_{\text{Type-A}} = \frac{\boldsymbol{k}\cdot S^{J,J_z}\cdot\boldsymbol{k}}{m_V^2}\frac{4}{4m_V^2 - m_3^2 - m_4^2}, \tag{B.3}$$

$$\mathcal{M}_b^{J,J_z}\Big|_{\text{Type-B}} = 0, \quad (\text{for } J = 0, 2) \tag{B.4}$$

$$\mathcal{M}_b^{J=1,J_z}\Big|_{\text{Type-B}} = \frac{4}{4m_V^2 - m_3^2 - m_4^2}[\boldsymbol{k}\cdot S^{J,J_z}\cdot\epsilon^b(k_4)]\left(\frac{m_4^2}{m_V^2} - 4\right), \tag{B.5}$$

$$\mathcal{M}_{ab}^{J,J_z}\Big|_{\text{Type-C}} = 2\times\tilde{\mathcal{M}}_{ab}^{J,J_z}, \quad (\text{for } J = 0, 2) \tag{B.6}$$

$$\mathcal{M}_{ab}^{J=1,J_z}\Big|_{\text{Type-C}} = 0, \tag{B.7}$$

$$\mathcal{M}_{ab}^{J,J_z}\Big|_{\text{Type-D}} = \tilde{\mathcal{M}}_{ab}^{J,J_z}, \quad (\text{for } J = 0, 1, 2) \tag{B.8}$$

where

$$\begin{aligned}
\tilde{\mathcal{M}}_{ab}^{J,J_z} = \Bigg\{\Bigg[&-4|\boldsymbol{k}|^2\frac{m_V^2}{m_3 m_4}\mathrm{Tr}S^{J,J_z}\delta_L^a\delta_L^b \\
&+ 8|\boldsymbol{k}|m_V\left[\frac{\boldsymbol{k}\cdot S^{J,J_z}\cdot\epsilon^a(k_3)}{m_4}\delta_{bL} - \frac{\boldsymbol{k}\cdot S^{J,J_z}\cdot\epsilon^b(k_4)}{m_3}\delta_{aL}\right] \\
&+ [\epsilon^a(k_3)\cdot S^{J,J_z}\cdot\epsilon^b(k_4)] \\
&\quad\times\frac{m_V^2\left[(m_V+E_3)(m_V+E_4)+|\boldsymbol{k}|^2\right]+(m_V^2-m_3^2)(m_V^2-m_4^2)}{m_V^2} \\
&- 4[\boldsymbol{k}\cdot S^{J,J_z}\cdot\boldsymbol{k}]\ \epsilon_\mu^a(k_3)\epsilon^{b\mu}(k_4)\Bigg]\times\frac{2}{4m_V^2 - m_3^2 - m_4^2} \\
&+ \mathrm{Tr}S^{J,J_z}\ \epsilon_\mu^a(k_3)\epsilon^{b\mu}(k_4) \\
&+ [\epsilon^a(k_3)\cdot S^{J,J_z}\cdot\epsilon^b(k_4)]\Bigg\}, \quad (\text{for } J = 0, 2)
\end{aligned} \tag{B.9}$$

$$\tilde{\mathcal{M}}_{ab}^{J=1,J_z} = [\epsilon^a(k_3)\cdot S^{J,J_z}\cdot\epsilon^b(k_4)] \times\left[\frac{2\left\{m_V^2\left[(m_V+E_3)(m_V+E_4)+|\boldsymbol{k}|^2\right]+(m_V^2-m_3^2)(m_V^2-m_4^2)\right\}}{m_V^2(4m_V^2-m_3^2-m_4^2)}-3\right]. \tag{B.10}$$

In the above expressions, we introduce the momentum, $\boldsymbol{k}$, and the energy of the final state particles in the center mass frame, $E_i(i=3,4)$, respectively.

$$|\boldsymbol{k}| = \frac{\sqrt{16m_V^4-8m_V^2(m_3^2+m_4^2)+(m_3^2-m_4^2)^2}}{4m_V}, \tag{B.11}$$

$$E_3 = \frac{\sqrt{16m_V^4-8m_V^2(-m_3^2+m_4^2)+(m_3^2-m_4^2)^2}}{4m_V}, \tag{B.12}$$

$$E_4 = \frac{\sqrt{16m_V^4-8m_V^2(m_3^2-m_4^2)+(m_3^2-m_4^2)^2}}{4m_V}. \tag{B.13}$$

We take the average for the scattering angle θ to obtain the cross section We also add up all the polarization for the final state particles.

For Type-A, we obtain the following squared amplitude.

$$\overline{\left|\mathcal{M}^{J}_{\text{Type-A}}\right|^2} \equiv \frac{1}{2}\int_{-1}^{1} d\cos\theta \left|\mathcal{M}^{J,J_z}_{\text{Type-A}}\right|^2, \tag{B.14}$$

where

$$\overline{\left|\mathcal{M}^{J=0}_{\text{Type-A}}\right|^2} = \frac{\left[40m_V^4-2m_V^2(m_3^2+m_4^2)+(m_3^2-m_4^2)^2\right]^2}{48m_V^8(4m_V^2-m_3^2-m_4^2)^2}, \tag{B.15}$$

$$\overline{\left|\mathcal{M}^{J=1}_{\text{Type-A}}\right|^2} = 0, \tag{B.16}$$

$$\overline{\left|\mathcal{M}^{J=2}_{\text{Type-A}}\right|^2} = \frac{\left[16m_V^4-8m_V^2(m_3^2+m_4^2)+(m_3^2-m_4^2)^2\right]^2}{120m_V^8(4m_V^2-m_3^2-m_4^2)^2}. \tag{B.17}$$

We obtain the same result for $J_z=0,\pm1$.

For Type-B, we need to add up all the polarization label ($b=\pm,L$). and obtain the following squared amplitude.

$$\begin{aligned}\overline{\left|\mathcal{M}^{J=1}_{\text{Type-B}}\right|^2} &\equiv \frac{1}{2}\int_{-1}^{1} d\cos\theta \sum_{b=\pm,L}\left|\mathcal{M}^{J=1,J_z}_{b,\text{Type-B}}\right|^2 \\ &= \frac{1}{3}\left(\frac{1}{4m_V^2-m_3^2-m_4^2}\right)^2\left(4-\frac{m_4^2}{m_V^2}\right)^2\frac{16m_V^4-8m_V^2(m_3^2+m_4^2)+(m_3^2-m_4^2)^2}{m_V^2},\end{aligned} \tag{B.18}$$

where we obtain the same result for $J_z=0,\pm1$.

For Type-C and Type-D, the amplitude is expressed in $\tilde{\mathcal{M}}^{J,J_z}_{ab}$ defined in Eqs. (B.9)-(B.10). After adding up all the polarization label $(a, b = \pm, L)$[26] and performing the $\cos\theta$ integral, we obtain the following results.

$$\overline{\left|\tilde{\mathcal{M}}^{J}\right|^2} \equiv \frac{1}{2}\int_{-1}^{1} d\cos\theta \sum_{a,b=\pm,L} \left|\tilde{\mathcal{M}}^{J,J_z}_{ab}\right|^2. \quad (|J_z| \le J) \tag{B.19}$$

The explicit forms are shown below for each J.

$$\overline{\left|\tilde{\mathcal{M}}^{J=0}\right|^2} = \underbrace{\frac{(6m_V^2 - m_3^2 - m_4^2)^2}{6m_V^4}}_{(a,b)=(\pm,\pm),(\pm,\mp)} + \underbrace{\frac{m_3^2 m_4^2 \left(32m_V^4 - (m_3^2 - m_4^2)^2\right)^2}{192m_V^8 \left(4m_V^2 - m_3^2 - m_4^2\right)^2}}_{(a,b)=(L,L)} \tag{B.20}$$

$$= \frac{1}{192m_V^8(4m_V^2 - m_3^2 - m_4^2)^2} \times \Big[18432m_V^{12} - 15360m_V^{10}\left(m_3^2 + m_4^2\right) + 128m_V^8\left(37m_3^4 + 37m_4^4 + 82m_3^2m_4^2\right) - 640m_V^6\left(m_3^2 + m_4^2\right)^3 + 32m_V^4\left(m_3^8 + m_4^8 + 2m_3^6m_4^2 + 2m_3^2m_4^6 + 10m_3^4m_4^4\right) + m_3^2m_4^2\left(m_3^2 - m_4^2\right)^4\Big] \tag{B.21}$$

$$\xrightarrow{m_3, m_4 \ll m_V} 6 + \mathcal{O}(1/m_V^2), \tag{B.22}$$

$$\overline{\left|\tilde{\mathcal{M}}^{J=1}\right|^2} = \underbrace{\frac{4m_3^4m_4^4}{3m_V^4\left(4m_V^2 - m_3^2 - m_4^2\right)^2}}_{(a,b)=(\pm,\pm),(\pm,\mp)} + \underbrace{\frac{m_3^2m_4^4\left(4m_V^2 + m_3^2 - m_4^2\right)^2}{12m_V^6\left(4m_V^2 - m_3^2 - m_4^2\right)^2}}_{(a,b)=(L,\pm)} + \underbrace{\frac{m_3^4m_4^2\left(4m_V^2 - m_3^2 + m_4^2\right)^2}{12m_V^6\left(4m_V^2 - m_3^2 - m_4^2\right)^2}}_{(a,b)=(\pm,L)} \tag{B.23}$$

$$= \frac{m_3^2m_4^2\left[16m_V^4\left(m_3^2 + m_4^2\right) - 8m_V^2\left(m_3^4 + m_4^4 - 4m_3^2m_4^2\right) + \left(m_3^2 - m_4^2\right)^2\left(m_2^2 + m_4^2\right)\right]}{12m_V^6\left(4m_V^2 - m_3^2 - m_4^2\right)^2} \tag{B.24}$$

$$\xrightarrow{m_3, m_4 \ll m_V} \frac{1}{12}\frac{m_3^2m_4^2(m_3^2 + m_4^2)}{m_V^6} + \mathcal{O}(1/m_V^8), \tag{B.25}$$

[26]The applicability of Type-B, -C, and -D formulas for photon channels are discussed after Eq. (B.28).

$$
\begin{aligned}
\overline{\left|\tilde{\mathcal{M}}^{J=2}\right|^2} &= \frac{1}{15m_V^4\left(4m_V^2-m_3^2-m_4^2\right)^2} \\
&\quad\times\Big[1536m_V^8-768m_V^6\left(m_3^2+m_4^2\right)+16m_V^4\left(7m_3^4+7m_4^4+38m_3^2m_4^2\right) \\
&\quad\underbrace{-8m_V^2\left(m_3^6+m_4^6+9m_3^4m_4^2+9m_3^2m_4^4\right)+42m_3^4m_4^4-8m_3^2m_4^6-8m_3^6m_4^2+m_3^8+m_4^8\Big]}_{(a,b)=(\pm,\pm),(\pm,\mp)} \\
&\quad+\underbrace{\frac{m_3^2\left[16m_V^4-4m_V^2\left(m_3^2-2m_4^2\right)+m_3^2m_4^2-m_4^4\right]^2}{20m_V^6\left(4m_V^2-m_3^2-m_4^2\right)^2}}_{(a,b)=(L,\pm)} \\
&\quad+\underbrace{\frac{m_4^2\left[16m_V^4-m_V^2\left(4m_4^2-8m_3^2\right)+m_3^2m_4^2-m_3^4\right]^2}{20m_V^6\left(4m_V^2-m_3^2-m_4^2\right)^2}}_{(a,b)=(\pm,L)} \\
&\quad+\underbrace{\frac{m_3^2m_4^2\left[\left(m_3^2-m_4^2\right)^2-80m_V^4\right]^2}{480m_V^8\left(4m_V^2-m_3^2-m_4^2\right)^2}}_{(a,b)=(L,L)} \qquad \text{(B.26)} \\
&= \frac{1}{480m_V^8\left(4m_V^2-m_3^2-m_4^2\right)^2} \\
&\quad\times\Big[49152m_V^{12}-18432m_V^{10}\left(m_3^2+m_4^2\right)+256m_V^8\left(2m_3^4+2m_4^4+149m_3^2m_4^2\right) \\
&\quad+128m_V^6\left(m_3^6+m_4^6-18m_3^4m_4^2-18m_3^2m_4^4\right) \\
&\quad+32m_V^4\left(m_3^8+m_4^8-31m_3^6m_4^2-31m_3^2m_4^6+88m_3^4m_4^4\right) \\
&\quad+24m_V^2m_3^2m4^2\left(m_3^2-m_4^2\right)^2\left(m_3^2+m_4^2\right)+m_3^2m_4^2\left(m_3^2-m_4^2\right)^4\Big] \qquad \text{(B.27)} \\
&\xrightarrow{m_3,m_4\ll m_V} \frac{32}{5}+\mathcal{O}(1/m_V^2), \qquad \text{(B.28)}
\end{aligned}
$$

where we show the polarizations of the final vectors in the first line. We also show the leading order behaviors for $m_3, m_4 \ll m_V$ in the last lines.

Note that we only add up the transverse modes for final states including photons. This manipulation is automatically incorporated in the above formulas as explained below. For the Type-B formula, shown in Eq. (B.18), the longitudinal contributions are canceled. For the Type-C and Type-D formulas, shown in Eqs. (B.20)-(B.26), the longitudinal contributions in $\overline{|\tilde{\mathcal{M}}^J|^2}$ vanish if we take the massless limit of final vectors. Therefore, all these formulas for annihilation cross sections can be applied even for the photon channels by taking the massless limit of m_3 or/and m_4. This point is also mentioned in Sec. 5.2.2. The cross section formulas are expressed using the above expressions and the final results are summarized in Eqs. (5.9)-(5.16).

The relevance of each partial mode is determined by $\overline{|\tilde{\mathcal{M}}^J|^2}$ for Type-D annihilation modes where we have nonzero contributions from all the $J = 0, 1, 2$ partial modes. In Fig. 35, we

show $\overline{|\tilde{\mathcal{M}}^J|^2}$ as functions of the final vector mass, m_4. The red solid, blue dashed, and black dotted curves show $J = 0$, $J = 1$, and $J = 2$, respectively. We take $m_V = 4$ TeV in all panels. In the upper left panel, we take $m_3 = 80.4$ GeV ($\ll m_V$), and thus we obtain the converged values shown in Eqs. (B.22)-(B.28) for $m_4 \ll m_V$. In the upper right and lower panels, we take $m_3 = 4$ TeV and 6 TeV, respectively. In these cases, m_3 is comparable to m_V, and we obtain the following asymptotic values for $m_4 \ll m_V$.

$$\overline{\left|\tilde{\mathcal{M}}^J\right|^2} \simeq \begin{cases} \frac{1}{6}\left(6 - \frac{m_3^2}{m_V^2}\right), & (J=0) \\ \frac{1}{12}\frac{m_3^4 m_4^2}{m_V^6}, & (J=1) \\ \frac{1}{15}\left(\frac{m_3^4}{m_V^4} + 12\frac{m_3^2}{m_V^2} + 96\right). & (J=2) \end{cases} \tag{B.29}$$

For our interesting region, $1 \leq m_3/m_V \leq 2$, the $J = 0$ ($J = 2$) contributions decrease (increase) for larger m_3/m_V. The $J = 1$ contributions are proportional to m_4^2 and negligible for $m_4 \ll m_V$.

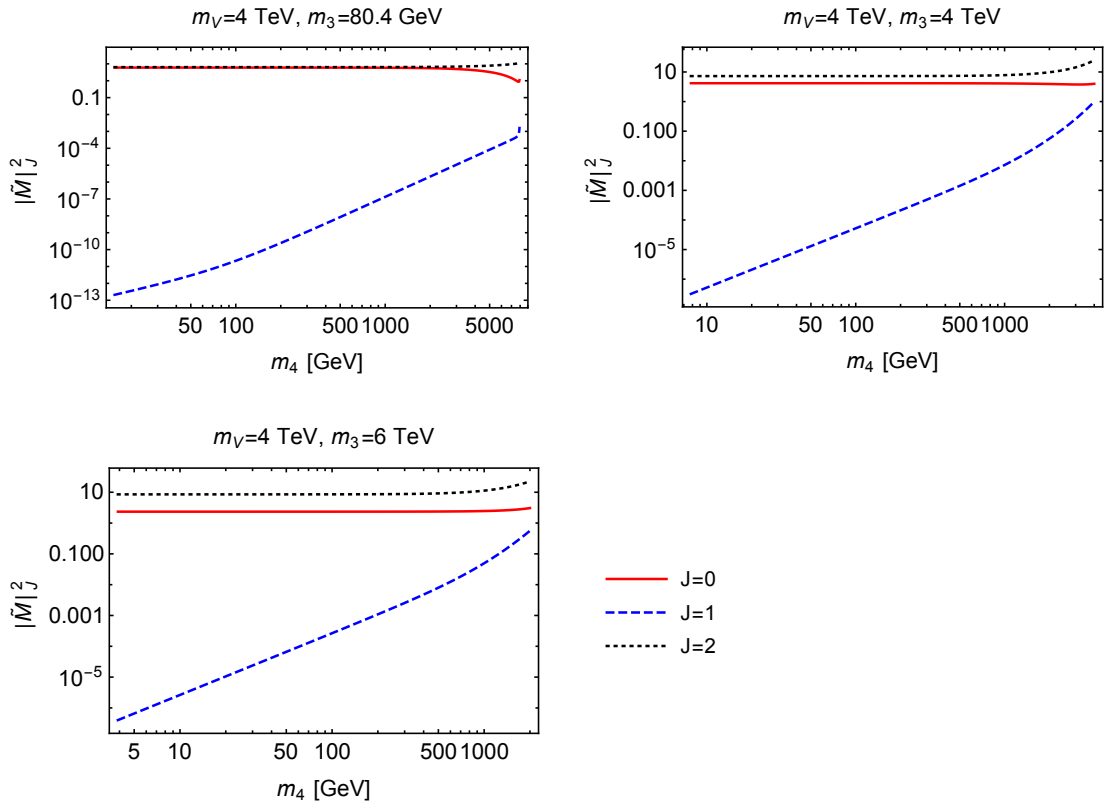

Figure 35: Plots for $\overline{|\tilde{\mathcal{M}}^J|^2}$ as functions of the final vector mass. The red solid, blue dashed, and black dotted curves show $J = 0$, $J = 1$, and $J = 2$, respectively.

References

[1] J. H. Oort, "The force exerted by the stellar system in the direction perpendicular to the galactic plane and some related problems," Bulletin of the Astronomical Institutes of the Netherlands, vol. 4, p. 249, 1932.

[2] F. Zwicky, Helv. Phys. Acta **6**, 110-127 (1933) doi:10.1007/s10714-008-0707-4

[3] V. C. Rubin and W. K. Ford, Jr., Astrophys. J. **159**, 379-403 (1970) doi:10.1086/150317

[4] K. C. Freeman, Astrophys. J. **160**, 811 (1970) doi:10.1086/150474

[5] N. Aghanim *et al.* [Planck], Astron. Astrophys. **641**, A6 (2020) [erratum: Astron. Astrophys. **652**, C4 (2021)] doi:10.1051/0004-6361/201833910 [arXiv:1807.06209 [astro-ph.CO]].

[6] M. Cirelli, N. Fornengo and A. Strumia, Nucl. Phys. B **753**, 178-194 (2006) doi:10.1016/j.nuclphysb.2006.07.012 [arXiv:hep-ph/0512090 [hep-ph]].

[7] M. Cirelli, A. Strumia and M. Tamburini, Nucl. Phys. B **787**, 152-175 (2007) doi:10.1016/j.nuclphysb.2007.07.023 [arXiv:0706.4071 [hep-ph]].

[8] M. Cirelli and A. Strumia, New J. Phys. **11**, 105005 (2009) doi:10.1088/1367-2630/11/10/105005 [arXiv:0903.3381 [hep-ph]].

[9] G. R. Farrar and P. Fayet, Phys. Lett. B **76**, 575-579 (1978) doi:10.1016/0370-2693(78)90858-4

[10] T. Flacke, A. Menon and D. J. Phalen, Phys. Rev. D **79**, 056009 (2009) doi:10.1103/PhysRevD.79.056009 [arXiv:0811.1598 [hep-ph]].

[11] N. Maru, N. Okada and S. Okada, Phys. Rev. D **98**, no.7, 075021 (2018) doi:10.1103/PhysRevD.98.075021 [arXiv:1803.01274 [hep-ph]].

[12] T. Flacke, D. W. Kang, K. Kong, G. Mohlabeng and S. C. Park, JHEP **04**, 041 (2017) doi:10.1007/JHEP04(2017)041 [arXiv:1702.02949 [hep-ph]].

[13] A. Belyaev, G. Cacciapaglia, J. Mckay, D. Marin and A. R. Zerwekh, Phys. Rev. D **99**, no.11, 115003 (2019) doi:10.1103/PhysRevD.99.115003 [arXiv:1808.10464 [hep-ph]].

[14] J. Hisano, S. Matsumoto, M. M. Nojiri and O. Saito, Phys. Rev. D **71**, 063528 (2005) doi:10.1103/PhysRevD.71.063528 [arXiv:hep-ph/0412403 [hep-ph]].

[15] K. Griest and D. Seckel, Phys. Rev. D **43**, 3191-3203 (1991) doi:10.1103/PhysRevD.43.3191

[16] Y. Yamada, Phys. Lett. B **682**, 435-440 (2010) doi:10.1016/j.physletb.2009.11.044 [arXiv:0906.5207 [hep-ph]].

[17] M. Ibe, S. Matsumoto and R. Sato, Phys. Lett. B **721**, 252-260 (2013) doi:10.1016/j.physletb.2013.03.015 [arXiv:1212.5989 [hep-ph]].

[18] J. McKay and P. Scott, Phys. Rev. D **97**, no.5, 055049 (2018) doi:10.1103/PhysRevD.97.055049 [arXiv:1712.00968 [hep-ph]].

[19] K. Agashe, A. Falkowski, I. Low and G. Servant, JHEP **04**, 027 (2008) doi:10.1088/1126-6708/2008/04/027 [arXiv:0712.2455 [hep-ph]].

[20] T. Appelquist, H. C. Cheng and B. A. Dobrescu, Phys. Rev. D **64**, 035002 (2001) doi:10.1103/PhysRevD.64.035002 [arXiv:hep-ph/0012100 [hep-ph]].

[21] H. Georgi, A. K. Grant and G. Hailu, Phys. Lett. B **506**, 207-214 (2001) doi:10.1016/S0370-2693(01)00408-7 [arXiv:hep-ph/0012379 [hep-ph]].

[22] H. C. Cheng, K. T. Matchev and M. Schmaltz, Phys. Rev. D **66**, 036005 (2002) doi:10.1103/PhysRevD.66.036005 [arXiv:hep-ph/0204342 [hep-ph]].

[23] C. T. Hill and R. J. Hill, Phys. Rev. D **76**, 115014 (2007) doi:10.1103/PhysRevD.76.115014 [arXiv:0705.0697 [hep-ph]].

[24] N. Arkani-Hamed, A. G. Cohen and H. Georgi, Phys. Lett. B **516**, 395-402 (2001) doi:10.1016/S0370-2693(01)00946-7 [arXiv:hep-th/0103135 [hep-th]].

[25] T. Abe, M. Fujiwara, J. Hisano and K. Matsushita, JHEP **07**, 136 (2020) doi:10.1007/JHEP07(2020)136 [arXiv:2004.00884 [hep-ph]].

[26] N. Arkani-Hamed, A. G. Cohen and H. Georgi, Phys. Rev. Lett. **86**, 4757-4761 (2001) doi:10.1103/PhysRevLett.86.4757 [arXiv:hep-th/0104005 [hep-th]].

[27] R. Coquereaux, AIP Conf. Proc. **589**, no.1, 181-203 (2001) doi:10.1063/1.1419325 [arXiv:hep-th/0105239 [hep-th]].

[28] K. Hally, H. E. Logan and T. Pilkington, Phys. Rev. D **85**, 095017 (2012) doi:10.1103/PhysRevD.85.095017 [arXiv:1202.5073 [hep-ph]].

[29] G. P. Lepage, L. Magnea, C. Nakhleh, U. Magnea and K. Hornbostel, Phys. Rev. D **46**, 4052-4067 (1992) doi:10.1103/PhysRevD.46.4052 [arXiv:hep-lat/9205007 [hep-lat]].

[30] M. Beneke, C. Hellmann and P. Ruiz-Femenia, JHEP **03**, 148 (2013) [erratum: JHEP **10**, 224 (2013)] doi:10.1007/JHEP03(2013)148 [arXiv:1210.7928 [hep-ph]].

[31] C. Hellmann and P. Ruiz-Femenía, JHEP **08**, 084 (2013) doi:10.1007/JHEP08(2013)084 [arXiv:1303.0200 [hep-ph]].

[32] J. Hisano, S. Matsumoto, M. Nagai, O. Saito and M. Senami, Phys. Lett. B **646**, 34-38 (2007) doi:10.1016/j.physletb.2007.01.012 [arXiv:hep-ph/0610249 [hep-ph]].

[33] T. Cohen, M. Lisanti, A. Pierce and T. R. Slatyer, JCAP **10**, 061 (2013) doi:10.1088/1475-7516/2013/10/061 [arXiv:1307.4082 [hep-ph]].

[34] G. Ovanesyan, T. R. Slatyer and I. W. Stewart, Phys. Rev. Lett. **114**, no.21, 211302 (2015) doi:10.1103/PhysRevLett.114.211302 [arXiv:1409.8294 [hep-ph]].

[35] G. Ovanesyan, N. L. Rodd, T. R. Slatyer and I. W. Stewart, Phys. Rev. D **95**, no.5, 055001 (2017) [erratum: Phys. Rev. D **100**, no.11, 119901 (2019)] doi:10.1103/PhysRevD.95.055001 [arXiv:1612.04814 [hep-ph]].

[36] M. Beneke, A. Broggio, C. Hasner and M. Vollmann, Phys. Lett. B **786**, 347-354 (2018) [erratum: Phys. Lett. B **810**, 135831 (2020)] doi:10.1016/j.physletb.2018.10.008 [arXiv:1805.07367 [hep-ph]].

[37] M. Beneke, A. Broggio, C. Hasner, K. Urban and M. Vollmann, JHEP **08**, 103 (2019) [erratum: JHEP **07**, 145 (2020)] doi:10.1007/JHEP08(2019)103 [arXiv:1903.08702 [hep-ph]].

[38] M. Beneke, R. Szafron and K. Urban, Phys. Lett. B **800**, 135112 (2020) doi:10.1016/j.physletb.2019.135112 [arXiv:1909.04584 [hep-ph]].

[39] P. A. Zyla *et al.* [Particle Data Group], PTEP **2020**, no.8, 083C01 (2020) doi:10.1093/ptep/ptaa104

[40] D. J. Fixsen, Astrophys. J. **707**, 916-920 (2009) doi:10.1088/0004-637X/707/2/916 [arXiv:0911.1955 [astro-ph.CO]].

[41] P. Ciafaloni, D. Comelli, A. Riotto, F. Sala, A. Strumia and A. Urbano, JCAP **03**, 019 (2011) doi:10.1088/1475-7516/2011/03/019 [arXiv:1009.0224 [hep-ph]].

[42] F. Bloch and A. Nordsieck, Phys. Rev. **52**, 54-59 (1937) doi:10.1103/PhysRev.52.54

[43] V. V. Sudakov, Sov. Phys. JETP **3**, 65-71 (1956)

[44] D. R. Yennie, S. C. Frautschi and H. Suura, Annals Phys. **13**, 379-452 (1961) doi:10.1016/0003-4916(61)90151-8

[45] M. Ciafaloni, P. Ciafaloni and D. Comelli, Phys. Rev. Lett. **84**, 4810-4813 (2000) doi:10.1103/PhysRevLett.84.4810 [arXiv:hep-ph/0001142 [hep-ph]].

[46] M. Cirelli, G. Corcella, A. Hektor, G. Hutsi, M. Kadastik, P. Panci, M. Raidal, F. Sala and A. Strumia, JCAP **03**, 051 (2011) [erratum: JCAP **10**, E01 (2012)] doi:10.1088/1475-7516/2012/10/E01 [arXiv:1012.4515 [hep-ph]].

[47] T. Sjostrand, S. Mrenna and P. Z. Skands, Comput. Phys. Commun. **178**, 852-867 (2008) doi:10.1016/j.cpc.2008.01.036 [arXiv:0710.3820 [hep-ph]].

[48] B. P. Kersevan and E. Richter-Was, Comput. Phys. Commun. **184**, 919-985 (2013) doi:10.1016/j.cpc.2012.10.032 [arXiv:hep-ph/0405247 [hep-ph]].

[49] J. Silk and M. Srednicki, Phys. Rev. Lett. **53**, 624 (1984) doi:10.1103/PhysRevLett.53.624

[50] F. W. Stecker, S. Rudaz and T. F. Walsh, Phys. Rev. Lett. **55**, 2622-2625 (1985) doi:10.1103/PhysRevLett.55.2622

[51] J. R. Ellis, R. A. Flores, K. Freese, S. Ritz, D. Seckel and J. Silk, Phys. Lett. B **214**, 403-412 (1988) doi:10.1016/0370-2693(88)91385-8

[52] S. Rudaz and F. W. Stecker, Astrophys. J. **325**, 16 (1988) doi:10.1086/165980

[53] F. W. Stecker and A. J. Tylka, Astrophys. J. Lett. **336**, L51-L54 (1989) doi:10.1086/185359

[54] M. S. Turner and F. Wilczek, Phys. Rev. D **42**, 1001-1007 (1990) doi:10.1103/PhysRevD.42.1001

[55] F. Donato, N. Fornengo and P. Salati, Phys. Rev. D **62**, 043003 (2000) doi:10.1103/PhysRevD.62.043003 [arXiv:hep-ph/9904481 [hep-ph]].

[56] H. Baer and S. Profumo, JCAP **12**, 008 (2005) doi:10.1088/1475-7516/2005/12/008 [arXiv:astro-ph/0510722 [astro-ph]].

[57] F. Donato, N. Fornengo and D. Maurin, Phys. Rev. D **78**, 043506 (2008) doi:10.1103/PhysRevD.78.043506 [arXiv:0803.2640 [hep-ph]].

[58] J. E. Gunn, B. W. Lee, I. Lerche, D. N. Schramm and G. Steigman, Astrophys. J. **223**, 1015-1031 (1978) doi:10.1086/156335

[59] F. W. Stecker, Astrophys. J. **223**, 1032-1036 (1978) doi:10.1086/156336

[60] Y. B. Zeldovich, A. A. Klypin, M. Y. Khlopov and V. M. Chechetkin, Sov. J. Nucl. Phys. **31**, 664-669 (1980)

[61] G. Giesen, M. Boudaud, Y. Génolini, V. Poulin, M. Cirelli, P. Salati and P. D. Serpico, JCAP **09**, 023 (2015) doi:10.1088/1475-7516/2015/9/023 [arXiv:1504.04276 [astro-ph.HE]].

[62] O. Adriani, G. C. Barbarino, G. A. Bazilevskaya, R. Bellotti, M. Boezio, E. A. Bogomolov, L. Bonechi, M. Bongi, V. Bonvicini and S. Bottai, *et al.* Phys. Rev. Lett. **102**, 051101 (2009) doi:10.1103/PhysRevLett.102.051101 [arXiv:0810.4994 [astro-ph]].

[63] O. Adriani *et al.* [PAMELA], Phys. Rev. Lett. **105**, 121101 (2010) doi:10.1103/PhysRevLett.105.121101 [arXiv:1007.0821 [astro-ph.HE]].

[64] M. Aguilar *et al.* [AMS], Phys. Rev. Lett. **117**, no.9, 091103 (2016) doi:10.1103/PhysRevLett.117.091103

[65] M. Boudaud, Y. Génolini, L. Derome, J. Lavalle, D. Maurin, P. Salati and P. D. Serpico, Phys. Rev. Res. **2**, no.2, 023022 (2020) doi:10.1103/PhysRevResearch.2.023022 [arXiv:1906.07119 [astro-ph.HE]].

[66] L. Bergstrom, Phys. Lett. B **225**, 372-380 (1989) doi:10.1016/0370-2693(89)90585-6

[67] T. Bringmann, L. Bergstrom and J. Edsjo, JHEP **01**, 049 (2008) doi:10.1088/1126-6708/2008/01/049 [arXiv:0710.3169 [hep-ph]].

[68] L. Bergstrom, P. Ullio and J. H. Buckley, Astropart. Phys. **9**, 137-162 (1998) doi:10.1016/S0927-6505(98)00015-2 [arXiv:astro-ph/9712318 [astro-ph]].

[69] A. M. Ghez, S. Salim, N. N. Weinberg, J. R. Lu, T. Do, J. K. Dunn, K. Matthews, M. Morris, S. Yelda and E. E. Becklin, *et al.* Astrophys. J. **689**, 1044-1062 (2008) doi:10.1086/592738 [arXiv:0808.2870 [astro-ph]].

[70] H. Abdallah *et al.* [HESS], Phys. Rev. Lett. **120**, no.20, 201101 (2018) doi:10.1103/PhysRevLett.120.201101 [arXiv:1805.05741 [astro-ph.HE]].

[71] M. de Naurois and L. Rolland, Astropart. Phys. **32**, 231 (2009) doi:10.1016/j.astropartphys.2009.09.001 [arXiv:0907.2610 [astro-ph.IM]].

[72] A. Abramowski *et al.* [H.E.S.S.], Phys. Rev. Lett. **114**, no.8, 081301 (2015) doi:10.1103/PhysRevLett.114.081301 [arXiv:1502.03244 [astro-ph.HE]].

[73] H. Dickinson and J. Conrad, Astropart. Phys. **41**, 17-30 (2013) doi:10.1016/j.astropartphys.2012.10.004 [arXiv:1203.5643 [astro-ph.IM]].

[74] F. Aharonian *et al.* [H.E.S.S.], Astron. Astrophys. **425**, L13-L17 (2004) doi:10.1051/0004-6361:200400055 [arXiv:astro-ph/0408145 [astro-ph]].

[75] F. Aharonian [H.E.S.S.], Astron. Astrophys. **503**, 817 (2009) doi:10.1051/0004-6361/200811569 [arXiv:0906.1247 [astro-ph.GA]].

[76] F. Aharonian *et al.* [H.E.S.S.], Astron. Astrophys. **432**, L25-L29 (2005) doi:10.1051/0004-6361:200500022 [arXiv:astro-ph/0501265 [astro-ph]].

[77] F. Aharonian *et al.* [H.E.S.S.], Nature **439**, 695-698 (2006) doi:10.1038/nature04467 [arXiv:astro-ph/0603021 [astro-ph]].

[78] A. Abramowski *et al.* [H.E.S.S.], Phys. Rev. D **90**, no.12, 122007 (2014) doi:10.1103/PhysRevD.90.122007 [arXiv:1411.7568 [astro-ph.HE]].

[79] A. Abramowski *et al.* [H.E.S.S.], Nature **531**, 476 (2016) doi:10.1038/nature17147 [arXiv:1603.07730 [astro-ph.HE]].

[80] F. Aharonian [H.E.S.S.], Astron. Astrophys. **483**, 509-517 (2008) doi:10.1051/0004-6361:20079230 [arXiv:0803.2844 [astro-ph]].

[81] H. Abdallah *et al.* [H.E.S.S.], Phys. Rev. Lett. **117**, no.11, 111301 (2016) doi:10.1103/PhysRevLett.117.111301 [arXiv:1607.08142 [astro-ph.HE]].

[82] G. Bertone, C. B. Jackson, G. Shaughnessy, T. M. P. Tait and A. Vallinotto, Phys. Rev. D **80**, 023512 (2009) doi:10.1103/PhysRevD.80.023512 [arXiv:0904.1442 [astro-ph.HE]].

[83] J. F. Navarro, C. S. Frenk and S. D. M. White, Astrophys. J. **490**, 493-508 (1997) doi:10.1086/304888 [arXiv:astro-ph/9611107 [astro-ph]].

[84] P. Mollitor, E. Nezri and R. Teyssier, Mon. Not. Roy. Astron. Soc. **447**, no.2, 1353-1369 (2015) doi:10.1093/mnras/stu2466 [arXiv:1405.4318 [astro-ph.GA]].

[85] L. Rinchiuso, N. L. Rodd, I. Moult, E. Moulin, M. Baumgart, T. Cohen, T. R. Slatyer, I. W. Stewart and V. Vaidya, Phys. Rev. D **98**, no.12, 123014 (2018) doi:10.1103/PhysRevD.98.123014 [arXiv:1808.04388 [astro-ph.HE]].

[86] M. Doro *et al.* [CTA Consortium], Astropart. Phys. **43**, 189-214 (2013) doi:10.1016/j.astropartphys.2012.08.002 [arXiv:1208.5356 [astro-ph.IM]].

[87] A. Acharyya *et al.* [CTA], JCAP **01**, 057 (2021) doi:10.1088/1475-7516/2021/01/057 [arXiv:2007.16129 [astro-ph.HE]].

[88] L. Rinchiuso, O. Macias, E. Moulin, N. L. Rodd and T. R. Slatyer, Phys. Rev. D **103**, no.2, 023011 (2021) doi:10.1103/PhysRevD.103.023011 [arXiv:2008.00692 [astro-ph.HE]].

[89] [ATLAS], ATL-PHYS-PUB-2018-044.